UNIVERSITÀ DELLA CALABRIA

UNIVERSITA' DELLA CALABRIA

Dipartimento di Fisica

CNR- Institute of Nanotechnology (NANOTEC)

Dottorato di Ricerca in

SCIENZE E TECNOLOGIE FISICHE, CHIMICHE E DEI MATERIALI

CICLO

XXIX

TITOLO TESI

Combined use of X-ray Fluorescence Microscopy, X-ray Phase Contrast Imaging, Atomic Force Microscopy and X-ray Nanotomography for high resolution quantitative Fe mapping in inflamed cells.

Settore Scientifico Disciplinare FIS/03 (FISICA DELLA MATERIA)

Coordinatore: Ch.mo Prof. Vincenzo Carbone

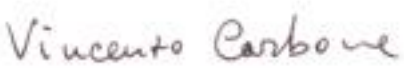

Firma

Supervisore/Tutor: Dr. Stefano Lagomarsino

Firma

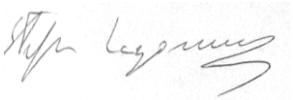

Ch.mo Prof. Roberto Bartolino

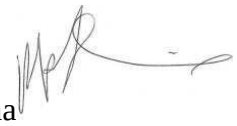

Firma

Dottoranda: Dott.ssa Chiara Gramaccioni

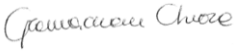

Firma _____

Acknowledgements

First of all thanks to my supervisor Dr. Stefano Lagomarsino to believe in me and in my own capacity, He was a real scientific guide.

I would like to thank my two tutors, Dr. Stefano Lagomarsino and Ch.mo Prof. Roberto Bartolino, for such an interesting and ambitious topic, as well as for opportunities given to me and for introducing me in such vast and interesting scientific areas.

I also thank, Dr. Emil Malucelli, for his patient teachings, the answers to all my doubts, and the aids in many instances. To him in particular way I am debtor, but I also thank the Department of Pharmacy and biotechnology of the University of Bologna (also for kindness and hospitality in my days in Bologna); particularly Ch.mo. Prof. Stefano Iotti for his support and for his forward-looking advice.

I must also thank Dr.ssa Giovanna Farruggia for supporting and help me for the preparation of the frozen hydrated cells used in this thesis.

Thanks to my colleague and friend Dr.ssa Alessandra Procopio whose company has undoubtedly made this experience more enjoyable over the last few months; thanks for her support and friendship.

I would like to thank Dr.ssa Michela Fratini and Dr. Andrea Notargiacomo for having advised me throughout the years of the PhD, for the articles and all the scientific suggestions they gave me, Thanks!

Thanks also to Dr.ssa Inna Bukreeva for her help in the data analysis, and in particular for the discussion of the tomographic results

I also thank the Department of Public Health and Infectious Diseases of the Univerity of Sapienza of Roma, particularly Ch.ma. Prof. Piera Valenti, Ch.ma. Prof. Francesca Berlutti for support, and precious and timely advices that allowed me to accomplish this work with completeness and precision; thanks also to Dr. Luigi di Rosa for his support.

I would like to thank the European Synchrotron Radiation Facility for providing the Beamtime, especially the whole staff of the beamline ID16A: in particular Peter Cloetens, responsible of the beamtime, but also Yang Yang, Alexandra Pacureanu, , Sylvain Bohic and Julio Cesar da Silva for their continuos support, and their help during the experimental work and data analysis.

I thank Dr.ssa Alessia Cedola of the CNR-Nanotec of Roma for the precious and always timely advice.

I am debtor also with all the people who in one way or another have come into contact with this work and have endured my questions: Florin Fus and Yin Cheng.

Thanks to Ch.ma Prof Silvia Gaudenzi and Fra Andrea who accompanied me, with theirs cordiality, during the most significant stages of the activity of the research and without which this adventure would not have begun.

Acknowledgements

Thanks to Cost 1207 for making it possible, at many moments, to realize this work hrough more than one STSM.

Special thanks go to my family for their unconditioned support during this long working period. Thanks to God who gave me courage, strength and help for my work.

Finally, I thank Mickaël, who was always close to me in this last year. He always managed to understand my sacrifices.

I hope I did not bother anyone, and I hope to continue in the future to work on areas of the thesis and collaborate with the same people that I had the pleasure and the honor to work with for this thesis.

To my Parents Enrico & Lucia.

Werner von Braun

"Research is what I'm doing when I don't know what I'm doing."

La pura ricerca è quando faccio quello che non so fare.

Blaise Pascal

"Par l'espace, l'univers me comprend et m'engloutit comme un point; par la pensée, je le comprends."

Attraverso lo spazio, l'universo mi comprende e mi inghiotte come un punto; attraverso il pensiero, io lo comprendo.

Abstract

The PhD project is based on the applications of several x-ray microscopy techniques for compositional and morphological studies at nanoscale spatial resolution to a biological problem, i.e. the quantitative determination of morphological and compositional properties of epithelial cells. Three x-ray microscopy techniques were exploited in this work: X-ray fluorescence microscopy, X-ray phase contrast imaging and nanotomography, which were made at the ID16NI beamline of the European Synchrotron Radiation Facility in Grenoble, France. In addition to synchrotron-based techniques, also Atomic Force Microscopy was performed. The latter was used for morphology characterization, and forcalibration and comparison purpose. The main aim of this study was to quantitatively determine the map of iron concentration at nanoscale spatial resolution of epithelial cells infected by bacterial pathogens in the presence or absence of lactoferrin (Lf), an iron-chelating glycoprotein of natural immunity. Two experiments have been carried out at ESRF, one on freeze dried cells, and one on frozen hydrated cells this last using the cryo stage foreseen in the Id16 NI beamline, in order to examine cells as close as possible to their native state, and to avoid radiation damage. The measurement and data analysis protocols have been carefully studied for optimal combination of all the techniques, to give quantitative results. Iron concentration and mass fraction maps have been obtained, which give an insight about the modification of iron spatial distribution under the influence of lactoferrin. Moreover, for the first time it has been demonstrated the possibility to obtain quantitative element concentration in cells through the combination of x-ray nanotomography in phase contrast and x-ray fluorescence microscopy.

Key words

Synchrotron, X-ray imaging, Fuorescence, Phase Contrast, sub-cellular level, Imaging, Nanotomography, Atomic Force Microscopy, Freeze-dried, Frozen hydrated cells, Culture Cells, Depth profile; Sample preparation.

Introduction

It was the 8th November of 1895, 120 years ago, when it was accidentally discovered the 'Existence of X-Ray, by the German physicist Wilhelm Roentgen. This fact in few months would revolutionize the field of medicine. In fact, next year, in the UK was built the First Department of radiology in a hospital and in a short time; the X-Rays began to be used in the world to obtain images of the fractures of bones. First radiology departments started to appear, like the one at the Glasgow Royal Infirmery. A number of remarkable X-ray images were made there: an X-ray of a kidney stone etc. New possibilities were discovered, not only to image the body parts but also to treat cancers or skin diseases. According to the most widespread history, Röntgen was doing the experiments with a fluorescent tube, an evacuated glass capsule through which was passed an electric current. For his experiment, Röntgen had covered the tube with the thick black cardboard sheets: whatever was illuminating the screen was at the same time practically invisible to the naked eye and able to penetrate the thick layer of paper, which covered the tube. Roentgen repeated the experiment many times to make sure to have not made a mistake. Then he tried to block the mysterious beam using a number of different objects, and found that only lead was good for this purpose. Finally, he replaced the screen with a photographic film and asked his wife to put his hand between the tube and the film. Röntgen in this way obtained the first X-Ray of the story: an image of the bones of the hand of his wife and his wedding ring (Figure1.1). He decided to provisionally call the mysterious rays "X" as the mathematical sign indicating an unknown quantity.

Figure 1.1: *Hand with Rings: print of Wilhelm Roentgen's first "medical" X-Ray of his wife's hand.*

However, X-rays are not only medical radiography. Immediately after their discovery, other extraordinary properties of X-rays have been studied. Among them, the possibility to obtain different X-ray fluorescence spectra for different elements, giving therefore the opportunity to accurate elemental analysis. Soon has been realized that X-rays are part of the electromagnetic spectrum, with wavelength close to the interatomic distances of crystals. Thus, the X-ray diffraction offered the opportunity to disclose the crystal structure, with countless fields of applications.

X-ray phase contrast imaging is a recent technique. Compared with absorption X-ray imaging, it requires specific properties of the X-ray beams used. These properties include strong spatial coherence, monochromaticity and high flux. As a result, most X-ray phase contrast imaging techniques have been developed using synchrotron sources. This currently limits the availability of these techniques, but there are ongoing developments to adapt it to conventional X-ray sources, such as interferometry based on diffraction networks (Pfeiffer et al., 2006).

For more than half a century X-rays have been generated by tubes similar in conception to that used by Roentgen. Only in the second half of XXth century new kind of sources, with unprecented

properties, have been developed, i.e. the synchrotron radiation sources, based on the radiating properties of charged particles circulating in a ring. ESRF is one of the most powerful synchrotron source in the world. It offers a brightness, energy range and resolution unachievable with laboratory radiation sources. This makes possible a large range of scientific applications otherwise impossible to exploit with traditional sources. A considerable part of research is dedicated to biomedical studies. Within this particular field, X-ray microscopy is a very important subject, in continuous development. One of the new beamline, build in the frame of the ESRF upgrade project, is ID16A, where the two experiments and the data analysis of this Ph.D. project have been performed. The ID16A nano-imaging end-station is dedicated to hard X-ray microanalysis nanoimaging and consists of the combination of X-ray fluorescence and 2D/3D X-ray phase imaging techniques. While X-ray fluorescence (XRF) reveals the chemical composition of the sample, the phase imaging completes the view by adding relevant information about the structure of the sample. Both techniques are exploited in this Ph.D. project in order to deal with questions related to the role of iron in inflamed cells. One of them is to quantitatively determine the intracellular map of iron concentration at nanoscale in cells infected by bacterial pathogens in the presence or absence of lactoferrin (Lf), an iron-chelating glycoprotein of natural immunity. The importance of iron for all eukaryotes, and particularly for humans, is widely recognized. Iron is essential for transport, storage and activation of oxygen, for electron transfer and many other metabolic processes. Iron homeostasis is also tightly linked to inflammation, immunity, and to response to pathogens. Macrophages are specialized cells that play a key role in these processes. Indeed, macrophages scavenge senescent and damaged erythrocytes, recycling iron recovered from hemoglobin. Many studies have addressed the relationships between iron management by macrophages, the ability of these cells to cope with invading pathogens and inflammation, and the effect of different molecules that can modulate the expression of proteins involved in iron homeostasis in macrophages. On the other hand, if not properly controlled, this situation can be dangerous leading to the anemia of inflammation (Paesano et al., 2012). Indeed, the expression of many proteins involved in cellular

iron management by macrophages varies in response to inflammatory stimuli as lipopolysaccharide (LPS) or to bacterial pathogens. Ferroportin, the sole protein able to export iron from the cells is down regulated in macrophages treated with LPS thus inhibiting iron export, increasing intracellular iron and leading to the anemia of inflammation (Paesano et al., 2012). Lactoferrin has been shown to possess potent antibacterial and anti-inflammatory properties (Valenti&Antonini, 2005; Berlutti et al., 2011). In particular, it has been recently showed that Lf counteract the LPS-induced decrease of ferroportin protein levels in adherent THP-1 macrophages challenged with LPS, a condition that mimics exposure to pathogens or inflammation. Restoring ferroportin at the plasma membrane will affect the iron export ability of these cells with possible beneficial effects, contrasting the anemia or the inflammation (Cutone et al., 2014). Therefore, it is of interest to evaluate the relationship between intracellular iron and bacterial infection in adherent macrophages. These studies at nano scale resolution could have a significant impact in defining new therapeutic interventions based on targeting intracellular iron.

In a first experiment we used freeze dried cells and we succeeded in recording fluorescence maps at 100 nm spatial resolution, together with 2D phase contrast images at 50 nm spatial resolution. Nanotomography at 50 and 25 nm resolution was also carried out on selected cells. Before the experiment session at ESRF, AFM was carried out on the same cells, in order to obtain independent information about morphology and to allow normalization of fluorescence intensity with illuminated volume, and consequently quantitative determination of concentration map. In a second experiment, we instead studied frozen hydrated cells, using the cryo stage installed in the Id16NI beamline. The frozen hydrated cells allow to examine cells as close as possible to their native state, and to avoid radiation damage. In this case, the illuminated volume cannot be measured with AFM, and therefore we used nanotomography for the purpose. The final aim of the study is combining all the techniques in order to obtain a quantitative mapping of iron concentration, mass fraction, density and volume of the cells, and to contribute to a better comprehension of the role of iron in the

inflammation process. Information on radiation damage can also be obtained by the combination of the different techniques.

The Ph.D. work is built as follows:

Chapter 1 describes the main characteristics of synchrotron radiation.

Chapter 2 is dedicated to a short description of the different X-ray microscopy techniques.

Chapter 3 describes the Atomic Force Microscopy technique.

Chapter 4 gives a brief description of the beamline ID16-A where the experiments have been done.

Chapter 5 describes the procedure of sample preparation

Chapter 6 illustrates the data analysis procedure and the strategy to obtain quantitative information from the combination of all the techniques

Chapter 7 describes the results obtained on freeze-dried cells.

Chapter 8 illustrates the results on frozen hydrated cells.

Chapter 9 gives the main conclusions, pointing out the problems encountered in the work, and illustrates future perspectives.

The original results, presented in this dissertation thesis, have been already published in part, and in part will be published in other manuscripts, currently in preparation (see List of publications).

My main contributions in this thesis work are presented in Chapters 5-6-7-8.

In details:

i. I took part in the **sample preparation**.

Samples were cultured at the Department for of Public Health and Infectiuos Diseases, of the University Sapienza at Rome. I collaborated on the cell preparation to allow for measurements. In particular, I took part to the delicate process of fast freezing, and prepared both freeze-dried and frozen hydrated cells (see chapter V).

ii. I participated in all the **synchrotron experiments** described in the thesis: one on freeze dried (ls2362) and two on frozen hydrated cells (ls2433-ls2551), both carried out at the beamline ID16A of the european synchrotron radiation facility (ESRF) of Grenoble (see chapter IV). Moreover, I participated to some shifts in the frame of in-house beamline research.

iii. I carried out the **data analysis** on all the experiment results, in particular:

- the fluorescence analysis using the PyMCA program, obtaining the fluorescence intensity maps of Iron, Potassium and Phosphorus
- The analysis of the Phase Contrast images, using the programs developed by the beamline staff.
- The elaboration, using the MATLAB platform, of the concentration and of the mass fraction maps, combining the information obtained by the fluorescence, the Atomic Force microscopy and the Phase Contrast images.
- The analysis of the holotomography experiment, and the elaboration of the cell thickness map using segmentation, and of the concentration map combining fluorescence and holotomography.
- The elaboration of the average values of Iron, Potassium and Phosphorus in the cells, differentiating between the nucleus and the cytoplasm, presented in Annex II.

This thesis research led to one work already published:

Gramaccioni C., Procopio A., Farruggia G., Malucelli E., Iotti S., Notargiacomo A., Fratini M., Yang Y., Pacureanu A., Cloetens P., Bohic S., Massimi L., Cutone A., Valenti P., Rosa L., Berlutti F. and Lagomarsino S. "Combined use of X-ray fluorescence microscopy, phase contrast imaging for high resolution quantitative iron mapping in inflamed cells." Journal of Physics: Conference Series, Volume 849, conference 1.

Moreover, one work is to be submitted to Applied Phys. Letters:

Gramaccioni C., Yang Y., Pacureanu A., Cloetens P., Bohic S., Malucelli E., Iotti S., Procopio A., Bukreeva I., Notargiacomo A., Fratini M., Valenti P., Rosa L., Berlutti F. and Lagomarsino S. **"Nanoscale quantitative determination of intracellular element concentration combining X-ray fluorescence microscopy with holotomography."**

Several others are in preparation. Furthermore, the results have been presented in several symposium:

- Poster presentation at the conference: BIOPHYSICS CNR, Area della Ricerca di Tor Vergata: "Quantitative high-resolution mapping of Fe concentration in inflamed cells, combining X-ray
- Oral presentation at the conference: 23rd SILS Conference Trento: "Combined use of X-ray Fluorescence Microscopy, Phase Contrast Imaging and Atomic Force Microscopy for high resolution quantitative Fe mapping in inflamed cells".
- Oral presentation at the conference: Meeting WG3: X-ray coherent and incoherent imaging diagnostics on Advanced X-ray metrology for theranostic, Amsterdam.
- Flash talk and poster presentation at the international conference X-Ray Microscopy XRM2016 OXFORD: "Combined use of X-Ray Fluorescence Microscopy, Phase Contrast Imaging and Nanotomography for high resolution quantitative Fe mapping in inflamed cells".
- Oral presentation at the conference: XTOP 2016 – 13th Biennial Conference on High-Resolution X-Ray Diffraction and Imaging –Brno, Czech Republic.

- Oral presentation at the conference: COST Action: MP1203 MC meeting co-located with X-ray optic metrology meeting, Athens Greece.
- Oral presentation at the conference: SILS 2016 Conference Bari: “Combined use of X-Ray fluorescence microscopy, phase contrast imaging and nanotomography for high resolution quantitative Fe mapping in inflamed cells.”
- Oral presentation International Workshop on Process and Biomedical Tomography, Warsaw.
- Oral presentation Microsymposiyum 2 (UDM2) ESRF user meeting 2017 Quantitative coherent X-ray diffraction imaging.
- Oral presentation during the Seminar: Synchrotron radiation for Life Sciences and Biology Quantitative coherent X-ray diffraction imaging. Department of Public Health and Infectious Diseases at Sapienza University of Rome.
- Poster presentation at the conference: Biophysics@rome 2017 CNR: “Nanotomography and X-Ray fluorescence microscopy for quantitative Iron concentration map in inflamed cells”.

Introduzione in Italiano

L'8 novembre del 1895, 120 anni fa, il fisico tedesco Wilhelm Röntgen scoprì per caso l'esistenza dei raggi-X, novità che nel giro di pochi mesi avrebbe rivoluzionato la medicina: l'anno successivo nel Regno Unito era già in funzione il primo dipartimento di radiologia all'interno di un ospedale e nel giro di poco tempo i raggi-X cominciarono ad essere usati in tutto il mondo per ottenere immagini delle fratture di ossa. Secondo la storia più diffusa, quel giorno Röntgen stava facendo degli esperimenti con un tubo fluorescente, una capsula di vetro sottovuoto attraverso cui veniva fatta passare una corrente elettrica. Dopo aver iniziato il suo esperimento, Röntgen si rese conto che qualcosa di strano stava accadendo. Mentre si preparava a passare alla fase successiva, distolse lo sguardo dall'apparecchio e con la coda dell'occhio notò che uno schermo cosparso di una sostanza fluorescente, che aveva sistemato a poca distanza dal tubo, stava brillando fiocamente. La luce era visibile solo con la coda dell'occhio, dove è situata una parte particolarmente sensibile della retina. Guardando fisso lo schermo, invece, Röntgen non riusciva a vedere nulla. Per il suo esperimento, Röntgen aveva coperto il tubo con degli spessi fogli di cartoncino nero: qualunque cosa stesse illuminando lo schermo era allo stesso tempo praticamente invisibile a occhio nudo e in grado di penetrare lo spesso strato di carta che copriva il tubo. Röntgen ripeté l'esperimento più volte per accertarsi di non aver commesso un errore. Poi cercò di bloccare il misterioso raggio utilizzando una serie di oggetti diversi e scoprì che soltanto il piombo riusciva nel compito. Infine sostituì lo schermo con una pellicola fotografica e chiese a sua moglie di mettere la mano tra il tubo e la pellicola. In questo modo Röntgen ottenne la prima radiografia della storia: un'immagine delle ossa della mano di sua moglie e del suo anello matrimoniale. Decise di chiamare provvisoriamente i misteriosi raggi "X", come il segno matematico che indica una quantità sconosciuta. Nei primi anni del 1900 i raggi X incominciarono ad essere utilizzati per trattare clinicamente malattie importanti come anche il cancro. Tuttavia, all'inizio non era ovvio che pur essendo ricoprendo un ruolo fondamentale nella cura delle malattie ci si sarebbe anche dovuti proteggere bene da essi in quanto le esposizioni sono nocive. Come ci troviamo oggi, dopo più di 100 anni da una scoperta straordinaria? Che conoscono le persone dei raggi X? Normalmente quando si pronuncia questa parola viene subito in mente l'idea di ospedale o malattia. Infatti, chi di noi almeno una volta nella vita non ha dovuto fare una radiografia o una tac per una visita medica? Ma non riduciamo raggi X solamente a questo, sarebbe troppo riduttivo! Se le persone hanno la possibilità di visitare una sorgente di sincrotrone, come ad esempio European Synchrotron Radiation Facility (ESRF) di

Grenoble, il loro parere in merito ai raggi X avrebbe la possibilità di arricchirsi. ESRF è la più potente sorgente di sincrotrone in Europa; capace di raggiungere un intervallo di energia ed una risoluzione irraggiungibile con le sorgenti di laboratorio. C'è una vasta gamma di possibili applicazioni scientifiche che utilizzano le proprietà dei raggi X della radiazione da sincrotrone. A ESRF, ad esempio ci sono diverse beamline a seconda del tipo di ricerca che si vuole effettuare. I fisici lavorano insieme con i chimici, ingegneri, biologi, medici, paleontologi ecc... Anche l'industria trova la sorgente di sincrotrone utile per le sue indagini, come ad esempio la "L'Oreal" che fa i propri esperimenti a ESRF. I raggi X ad esempio sono usati per studiare la struttura, i processi di crescita e la morfologia delle superfici. Essi sono utilizzati per studiare i comportamenti dei materiali ad altissime pressioni, per rivelarne la struttura cristallina. Infine essi sono utilizzati per applicazioni biomediche ad altissima risoluzione (50 nm). L' imaging a contrasto di fase a raggi X è un arte del tutto recente. Al contrario dell'imaging per assorbimento, richiede specifiche proprietà del fascio di raggi X. Ad esempio una forte coerenza spaziale, una monocromaticità del facsio ecc.. Pertanto, la maggior parte delle tecniche di imaging X a contrasto si sono sviluppate a seguito delle sorgenti di sincrotrone di sincrotrone. Gli esperimenti effettuati e la loro relativa dati, presentati in questa tesi di di dottorato sono stati svolti presso la beamlineID16NI a ESRF. In particolare questa beamline ID16NI è dedicato a raggi X duri e la microanalisi consiste nella combinazione di raggi X di fluorescenza con tecniche a raggi X di imaging di fase sia 2D che 3D. Mentre i raggi X di fluorescenza (XRF) ci rivelano la composizione chimica del campione, l'imaging a contrasto di fase completa la nostra analisi aggiungendo informazioni relative alla struttura del campione. Entrambe queste tecniche sono state sfruttate in questa ricerca di dottorato al fine di affrontare alcune questioni fondamentali. Uno di questi è di determinare quantitativamente la concentrazione di ferro con una spaziale nanometrica in cellule infettate da batteri i in presenza o assenza di lattoferrina, una glicoproteina naturale del sistema immunitario.

L'importanza del ferro per tutti gli organismi viventi e in modo particolare per gli esseri umani è universalmente riconosciuta. Il ferro è un elemento essenziale per il trasporto dell'ossigeno per il trasferimento degli elettroni ed è responsabile di molti altri pocessi del metabolismo.

L'omeostasi del Ferro è anche strettamente legata ai processi di infiammazione, immunità, e alla risposta agli agenti patogeni. I macrofagi sono cellule specializzate che svolgono un ruolo chiave in questi processi. In effetti, i macrofagi riciclano il ferro recuperato dall' emoglobina. Molti studi hanno affrontato proprio la relazione tra il ferro e i macrofagi, che sono cellule in grado di reagire agli agenti patogeni e ai processi infiammatori, e si sono anche fatti degli studi riguardanti l'effetto di diverse molecole in grado di modulare l'espressione delle proteine coinvolte nell'omeostasi del ferro nei macrofagi stessi. D'altra parte, se non adeguatamente controllata la concentrazione del

ferro, questa situazione può essere pericolosa portare a processi di infiammazione anemica (Paesano et al. 2012).

La lactoferrina (Lf) è stato dimostrato che ha forte proprietà antibatteriche e antinfiammatorie (Valenti&Antonini, 2005; Berlutti et al., 2011). In particolare recentemente si è dimostrato che Lf contrasta la riduzione di ferroportina causata da LPS. Restaurando la ferroportina nella membrana del plasma, influenza dunque la capacità di esportazione del ferro da parte di queste cellule con effetti benefici che contrastano dunque l'infiammazione anemica (Cutone et al., 2014). Ciononostante sarebbe molto interessante essere in grado di poter valutare la relazione tra la concentrazione del ferro intracellulare e le infiammazioni batteriche in particolar modo come diminuisce a livello quantitativo la concentrazione del ferro in queste condizioni. Questi studi ad una risoluzione spaziale nanometrica possono avere un ruolo significativo per definire nuovi interventi terapeutici mirati alla concentrazione del ferro intracellulare.

Nel primo esperimento, ls2362, abbiamo usato cellule liofilizzate "freeze-dried", e siamo riusciti a registrare mappe di fluorescenza con una risoluzione spaziale di 100 nm e delle immagini a contrasto di fase 2D con una risoluzione spaziale di 50 nm. È stata anche fatta tomografia a contrasto di fase con risoluzione spaziale di 50 e 25 nm sulle stesse cellule. Inoltre, prima dell'esperimento abbiamo misurato, sulle stesse cellule, la loro topografia con la tecnica dell'Atomic Force Microscopy (AFM), in modo da poter normalizzare le intensità di fluorescenza con il volume illuminato, ed essere quindi in grado di determinare quantitativamente le mappe di concentrazione. Tuttavia, dopo le misure di fluorescenza abbiamo notato un po' di danni da radiazioni. Nel secondo esperimento, ls2433, abbiamo utilizzato cellule idratate-congelate "frozen hydrated", utilizzando il criostato nella beamline ID16A, per esaminare le cellule il più vicino possibile al loro stato nativo. In questo caso il volume illuminato non può essere misurato con la tecnica dell'AFM, e pertanto si utilizzerà la tomografia per tale scopo. Inoltre, nel secondo esperimento si sono utilizzate invece di cellule murine delle cellule umane THP-1 macrofagi, al fine di acquisire informazioni utili per la salute umana. In questa tesi abbiamo analizzato anche i dati tomografici, delle cellule ad alta risoluzione per avere informazioni strutturali tridimensionali, cosa che non è mai stata fatta prima. Infine combinando queste tecniche (fluorescenza a raggi X, imaging a contrasto di fase 2D, tomografia a contrasto di fase e AFM), è stato possibile studiare la radiazione e gli effetti sui campioni cellulari; infatti non c'è alcun dubbio che durante l'esposizione del campione al fascio dei raggi X si sono verificati alcuni danni da radiazione.

La tesi di Dottorato è impostata nella seguente maniera:

Capitolo 1 descrizione delle caratteristiche della radiazione da sincrotrone.

Capitolo 2 descrizione delle tecniche di Imaging e di fluorescenza basate sulla radiazione da sincrotrone.

Capitolo 3 descrizione della teoria alla base della tecnica AFM.

Capitolo 4 descrizione della beamline ID16-A ESRF a Grenoble, dove sono stati svolti gli esperimenti oggetto di studio.

Capitolo 5 in questo capitolo sono descritti i campioni biologici. Murrin cells linea J774A.1 (ATCC® TIB-67™), trattate con lipopolisaccaride (LPS) e con lattoferrina (Lf).

Capitolo 6 trattazione dei dati analizzati e della metodologia adotatta per ottenere delle informazioni quantitative attraverso l'utilizzo di tutte le tecniche descritte nel precedente capitolo 2.

Capitolo 7 descrizione dei risultati ottenuti sulle cellule macrofaghe freezedried.

Capitolo 8 descrizione dei risultati ottenuti sulle cellule macrofaghe frozen hydrated.

Capitolo 9 riassunto della ricerca e prospettive.

Gli originali risultati, presentati in questa tesi di dottorato sono pubblicati parzialmente e in parte saranno oggetto di altre pubblicazioni attualmente in preparazione (vedi Elenco delle pubblicazioni).

I miei contributi principali in questo lavoro di tesi sono presentati nei Capitoli 5-6-7-8.

Nel dettaglio:

i. Ho partecipato alla **preparazione dei campioni**.
   Le cellule sono state coltivate presso il Dipartimento per la sanità pubblica e malattie infettive, dell'Università della Sapienza di Roma. Ho collaborato alla preparazione delle cellule per consentirne poi le misure. In particolare ho partecipato al veloce e delicato

processo di congelamento, e alla preparazione sia delle cellule freeze-dried che delle frozen hydrated (si veda il capitolo V).

ii. Ho partecipato a tutti gli **esperimenti di sincrotrone** descritti nella tesi: uno su cellule liofilizzate (ls2362) e due su cellule idratate congelate (ls2433-ls2551), tutti eseguiti nella beamline ID16A appartenente al sincrotrone europeo (ESRF) di Grenoble (si veda il capitolo IV). Inoltre, ho avuto a disposizione anche qualche shift aggiuntivo per la mia ricerca all'interno dell'in-house della beamline.

iii. Ho effettuato **l'analisi dei dati** su tutti i risultati acquisiti nel corso dei vari esperimenti, in particolare:

– Dall'analisi della fluorescenza con l'utilizzo del programma PyMCA, ho ottenuto le mappe di intensità di fluorescenza del Ferro, del Potassio e del Fosforo.

– Ho analizzato le immagini a Contrasto di Fase, utilizzando i programmi sviluppati dal personale della beamline.

– Ho elaborato, combinando le informazioni ottenute dalla fluorescenza, dalla microscopia a Forza Atomica e dalle immagini a contrasto di fase, utilizzando la piattaforma MATLAB, le mappe di concentrazione e di mass fraction.

– Ho analizzato i dati acquisiti di tomografia a contrasto di fase, ho elaborato utilizzando la segmentazione una mappa dello spessore della cellula e una mappa di concentrazione combinando fluorescenza e tomografia a contrasto di fase.

– Ho elaborato nelle cellule i valori medi di Ferro, Potassio e Fosforo, differenziando tra il nucleo e il citoplasma (si veda quanto riportato nell'allegato II).

Questa ricerca di tesi ha prodotto unalavoro già pubblicato:

Gramaccioni C., Procopio A., Farruggia G., Malucelli E., Iotti S., Notargiacomo A., Fratini M., Yang Y., Pacureanu A., Cloetens P., Bohic S., Massimi L., Cutone A., Valenti P., Rosa L., Berlutti F. and Lagomarsino S. "Combined use of X-ray fluorescence microscopy, phase contrast imaging for high resolution quantitative iron mapping in inflamed cells." Journal of Physics: Conference Series, Volume 849, conference 1.

Un lavoro è in via di sottomissione ad Appl. Phys. Lett.:

Gramaccioni C., Yang Y., Pacureanu A., Cloetens P., Bohic S., Malucelli E., Iotti S., Procopio A., Bukreeva I., Notargiacomo A., Fratini M., Valenti P., Rosa L., Berlutti F. and Lagomarsino S. **"Nanoscale quantitative determination of intracellular element concentration combining X-ray fluorescence microscopy with holotomography."**

Altri lavori sono in via di elaborazione. Oltre alle pubblicazioni, il lavoro è stato presentato nel corso di diversi convegni:

- Poster presentation at the conference: BIOPHYSICS CNR, Area della Ricerca di Tor Vergata: "Quantitative high-resolution mapping of Fe concentration in inflamed cells, combining X-ray
- Oral presentation at the conference: 23 th SILS Conference Trento: "Combined use of X-ray fluorescence microscopy, phase contrast Imaging and atomic force microscopy for high resolution quantitative Fe mapping in inflamed cells."
- Oral presentation at the conference: Meeting WG3: X-ray coherent and incoherent imaging diagnostics on Advanced X-ray metrology for theranostic, Amsterdam.
- Flash talk and poster presentation at the international conference X-Ray Microscopy XRM2016 OXFORD: "Combined use of X-Ray fluorescence microscopy, phase contrast imaging and nanotomography for high resolution quantitative Fe mapping in inflamed cells".
- Oral presentation at the conference: XTOP 2016 – 13th Biennial Conference on High-Resolution X-Ray Diffraction and Imaging –Brno, Czech Republic.
- Oral presentation at the conference: COST Action: MP1203 MC meeting co-located with X-ray optic metrology meeting, Athens Greece.

- Oral presentation at the conference: SILS 2016 Conference Bari: “Combined use of X-Ray fluorescence microscopy, phase contrast imaging and nanotomography for high resolution quantitative Fe mapping in inflamed cells.”
- Oral presentation International Workshop on Process and Biomedical Tomography, Warsaw.
- Oral presentation Microsymposiyum 2 (UDM2) ESRF user meeting 2017 Quantitative coherent X-ray diffraction imaging.
- Oral presentation during the Seminar: Synchrotron radiation for Life Sciences and Biology Quantitative coherent X-ray diffraction imaging. Department of Public Health and Infectious Diseases at Sapienza University of Rome.
- Poster presentation at the conference: Biophysics@rome 2017 CNR: “Nanotomography and X-Ray fluorescence microscopy for quantitative Iron concentration map in inflamed cells.”

Contents

Contents

CHAPTER 1

SYNCHROTRON RADIATION

1. Characteristics of synchrotron radiation

When electrons or positrons moving at relativistic speed, i.e., close to the velocity of light, if they are subjected to a magnetic field, their trajectory follows a circular orbit and synchrotron radiation (SR) is emitted in the tangential direction. The radiated energy is proportional to the fourth power of the particle speed and inversely proportional to the square of the radius of the path. The beam is concentrated into a forward narrow cone with half angle of typically 0.1 to 1 mrad. Synchrotron radiation facilities typically consist of an injection system, a storage ring and beamlines. In the injection system, electrons are generated, pre-accelerated, and sometimes a second accelerator further accelerates these electrons to few GeV before injection into the storage ring. At ESRF, the electrons are accelerated to a nominal energy of 6 GeV.

In the ring, bunches of electrons periodically circulate at relativistic speed for periods of up to many hours. The storage ring consists of radio frequency (RF) cavities, bending magnets, insertion devices and different control systems mainly to control the orbit of the electrons (Fig.1.1). The RF cavity system restores energy, which the electrons lose because of the emission of SR, and stabilizes the bunch of electrons. The high-energy electrons are maintained in a planar orbit by using bending magnet. Any accelerated charge radiates an e.m. field which, if the particle has a speed $v << c$ (c light speed), is isotropic around the acceleration. In a synchrotron (or storage ring), the electrons have velocity $v \approx c$, therefore relativistic effects dominate and the radiated e.m. field is sharply peaked in the direction of motion of the particles. The cone aperture is $1/\gamma$, where γ is the ratio between the particle energy and its rest mass. For electrons or positrons of energy E expressed in GeV $\gamma = 1957 * E$. Thus for 6 GeV electrons the aperture is about 80 μrad.

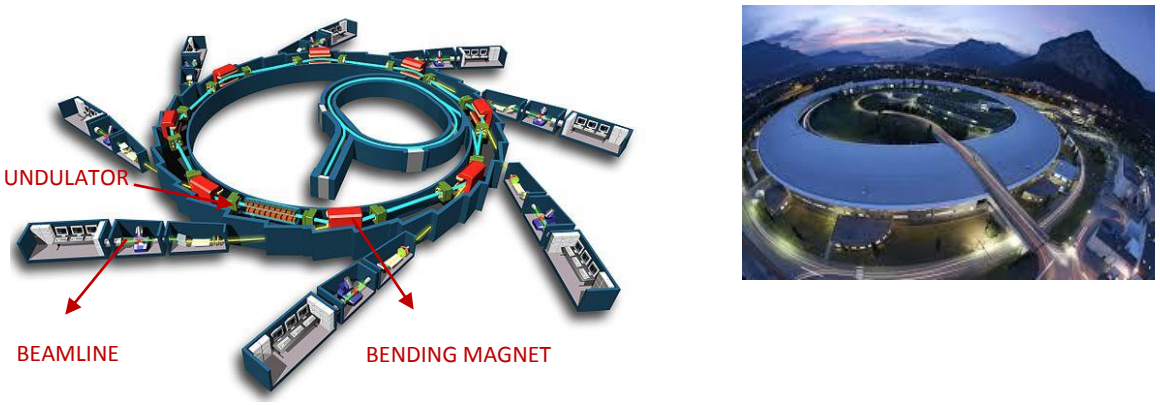

Figure 1.1:

Schematic picture of the synchrotron ring of the ESRF (right) and external view of the building (left)Electrons are first accelerated in the linear accelerator (linac) and in a booster synchrotron, and then they are injected into a storage ring.

The emission spectrum is continous from infrared radiation up to a critical wavelength λ_c which depends on ρ and γ. The critical wavelength is defined as the value for which half of the total power is emitted at wavelengths shorter than the critical one; λ_c is given by $\lambda_c = (4\pi/3)\ \rho/\gamma^3$. In order to improve the intensity of emission, insertion devices (I.D.) have been conceived where the charged particles pass through alternating magnetic (Figure 1.2) poles and are therefore compelled to have a zig-zag trajectory. At each wiggle (Figure 1.3), they emit radiation, which is therefore enhanced, of a 2N factor where N is the number of poles. These devices are called wigglers or undulators and the distinction is essentially due to the relation between the angular deviation α at each wiggle and the aperture $1/\gamma$. Values of $\alpha >> 1/\gamma$ identify wigglers, while $\alpha \approx 1/\gamma$ identify undulators. The radiation emitted by a wiggler is the incoherent sum of the radiation fields emitted by each individual magnet. The spectrum is continuous but shifted at higher energies with respect to that of a bending magnet. Instead, in the undulator regime, the amplitudes of the field radiated at each period of the particle trajectory may interfere resulting in a periodic radiation field. The spectrum is thus not continuous, but resonances occur at given frequencies (the fundamental and the harmonics).

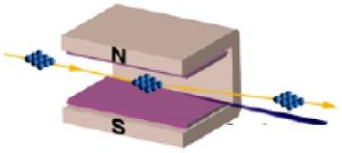

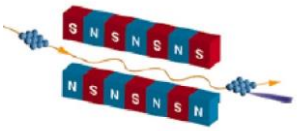

Figure 1.2: *Schematic picture of Bending Magnet.*

Figure 1.3: *Schematic picture of Wiggler.*

1.1. Brightness, brilliance and flux

What is important in S.R. is not only flux, which is defined as the number of photons per unit time in a given band-pass energy: F = ph/s/($\Delta\lambda/\lambda$). For $\Delta\lambda/\lambda$ is conventionally taken the value of 10^{-3}. Taking into account also the angular aperture (i.e. the collimation) we can speak of brightness which is the flux per solid angle: Brightness = ph/s/mrad^2/($\Delta\lambda/\lambda$) [1]. In fact also the size source is of importance and therefore the brilliance becomes the parameter of interest: Brilliance = Brightness/$\sigma_x\sigma_y$ = ph/s/mrad^2/$\sigma_x\sigma_y$/($\Delta\lambda/\lambda$) where σ_x and σ_y are the transverse source sizes (horizontal and vertical). The emittance of the source ε is defined as: $\varepsilon = \varepsilon_h * \varepsilon_v$ where the horizontal and vertical emittances ε_h and ε_v are defined as $\varepsilon_h = \sigma_x\sigma'_x$ and $\varepsilon_v = \sigma_y\sigma'_y$, where σ_x and σ_y are the horizontal and vertical source size respectively and σ'_x and σ'_y are the divergence of the beam in the horizontal and vertical directions respectively . The figure of merit of a synchrotron is brilliance and emittance. The first should be as high as possible and the last should be as low as possible. Just to give an idea about numbers, if an x-ray tube has a brilliance of the order of 10^7, brilliance at an undulator beamline of third generation S.R. can be as high as 10^{20} - 10^{21}. Horizontal and vertical emittances at ESRF reached values as low as 4 and 0.025 nm respectively.

Time structure is also important, at least for time resolved experiments. S.R. is not continuous, but is emitted in bunches corresponding to the electron bunches in the storage ring. Duration of a single bunch is, for ex. at the European Synchrotron Radiation Facility (ESRF) in Grenoble, of 20 picoseconds. Time between bunches depend on the filling mode of the storage ring. For single bunch mode (the one generally used for time resolved experiments) is about 3 μs at ESRF.

One of the important characteristics of the photon beam is the coherence. There are two kinds of coherence: transverse coherence and longitudinal coherence. The transverse coherence refers to the coherence of the electromagnetic disturbances at two points perpendicular to the propagation

direction. Consider two points P_1 and P_2 that lie on the same wave front of an e.m. wave at time t=0. Let $E_1(t)$ and $E_2(t)$ be the corresponding electric fields at these points. By definition, the difference between the phases of the two fields at t = 0 is zero. If this difference remains zero at any time t > 0, there is a perfect coherence between the two points. If this occurs for any two points of the e.m. wave front, the wave is *perfectly coherent* (the degree of spatial coherence is 1). Usually, for any point P_1, the point P_2 must lie within some finite area (*coherence area or length*) around P_1 to maintain the phase correlation.

From the Van Cittert-Zernike theorem [2] it comes out that, the radiation field from a primary incoherent source gains coherence during the propagation. Furthermore, the larger is the distance from the source and the smaller is the source size; the larger is the coherence length. The coherence length l can therefore be approximately defined as:

$l = \lambda L/s$ where λ is the wavelength, L the distance source-sample and s the transversal source size. Synchrotron radiation is inherently incoherent, but due the large distance from the source, the beam at the sample position has a large coherence.

The longitudinal coherence refers to the case of two points along the propagation direction and is related to the monochromaticity of the beam.

The longitudinal coherence is characterized by the longitudinal coherence length lc, which is related to the bandwidth $\delta\lambda/\lambda$ by:

$$l_c = \frac{\lambda^2}{\delta\lambda} \qquad \textbf{(1.1)}$$

CHAPTER 2

X-RAY MICROSCOPY TECHNIQUES

2.1 Interaction of X-rays with matter

X-rays are part of the electromagnetic (e.m) spectrum, extending in energy from about 250 eV to 50 KeV. Due to the simple relation $E = h\nu = hc/\lambda$, where E is the energy, ν the wave frequency, λ the wavelength, c the light speed and h the Planck constant, the same range can be expressed in wavelength between 50 nm and 0.025 nm. The part at lower energy (up to about 2 KeV) is called "soft", the more energetic "hard". X-rays interact with matter essentially via electrons. An isolated electron subjected to interaction with an X-ray plane wave is instantly accelerated and then radiates as a dipole antenna.

The strength of the interaction has been established by Thomson and the ratio between the incident amplitude and the scattered one is proportional to the Thomson scattering length (called also classical electron radius) $r_0 = e^2/mc^2 = 2.82 \times 10^{-13}$ cm. If the electron is bound to an atom a form factor, (atomic scattering factor) must be considered which takes into account the distribution of electrons in the atom. It can be useful to describe from a phenomenological point of view three phenomena that take place when X-rays interact with matter: absorption, refraction and diffraction.

2.1.1 Absorption

When an X-ray photon beam having an intensity I_0 impinges on a target of thickness t, the intensity I after the target is simply given by: $I = I_0 e^{-\mu t}$ where μ is called the linear absorption coefficient. The physical phenomenon at the basis of absorption is the photoelectric effect. When an X-ray photon has an energy larger than the binding energy of a given electron shell, the photon is absorbed and the electrons are ejected with a kinetic energy given in first approximation by the difference between the photon energy and the binding energy. This implies that the absorption coefficient as a function of photon energy is not continuous, but has sudden jumps in

correspondence of the electron binding energies of the target elements. The jumps are called absorption edges and the absorption coefficient before and after the absorption edge are significantly different (6 to 8 times). Absorption edge of the first shell of electrons is called K, the second L, the third M, etc. When an electron is ejected, a hole in the corresponding shell is created which electrons of the next shell immediately fill. This gives rise in turn to emission of a photon (x-ray fluorescence) or to other electrons (Auger electron). We will describe the X-ray fluorescence in detail in par. 2.3. In the energy region intermediate between two absorption edges, the absorption coefficient μ is approximately proportional to λ^3. This implies that μ is very different in the soft and hard regions. Just to give an example, photons of 25 KeV can pass 1 mm of Al with low losses, but are completely absorbed by an Al layer 1 micron thick if their energy is 410 eV.

2.1.2 Refraction and total reflection

The refraction index r of a material can be expressed by: $r = n - i\beta = 1 - \delta - i\beta$. We recall here that $n = (\varepsilon_r \mu_r)^{1/2}$ where ε_r and μ_r are respectively the relative (to the vacuum) dielectric constant and the relative magnetic permeability of the material under consideration.

If an X-ray beam traveling in a medium with refraction index n_1 impinges, at an angle α_1, on the flat surface of a material having refraction index n_2, it will be refracted following the simple Snell formula: $\cos\alpha_1 / \cos\alpha_2 = n_2/n_1$

Using quantum mechanical theory δ and β for a monatomic material in the X-ray region can be expressed respectively as:

$$\delta = \lambda^2 (N_0/A)\rho_m r_0(Z+f') \quad \text{and} \quad \beta = (\lambda/4\pi)\mu \quad \textbf{(2.1)}$$

where N_0 is the Avogadros' number, A the atomic mass, ρ_m the density, r_0 the classical electron radius, Z the atomic number of the element and f' a correction factor related to the rapid variation of the atomic scattering factor for X-rays in proximity of the absorption edges. μ is the linear absorption coefficient. δ is always positive and this implies that for X-rays all the materials have a refraction coefficient less than 1. Therefore if medium1 is vacuum (or air) $n_2 < n_1$ and the radiation will travel in the material with an angle $\alpha_2 < \alpha_1$ As a consequence, there will be an incident angle $\alpha_1 = \alpha_c$ for which $\alpha_2 = 0$. In this case, the incident beam is totally reflected and only an evanescent wave can enter into the material. α_c is called the critical angle for total reflection and is not difficult

to see that $\alpha_c \approx (2\delta)^{1/2}$. Therefore, α_c is proportional to λ and to the square root of Z and ρ_m. This property is the basis for optics based on total reflection and for refractive x-ray optics.

2.1.3 Diffraction

In refraction and reflection the atoms do not absorb the x-ray photons, but once excited by them, they are-irradiate X-ray beam of the same energy (in the elastic approximation). The same happens in diffraction. Diffraction is a common phenomenon of interaction between a wave and an object having dimensions of the same order of magnitude of the wavelength into consideration. Every point of the object, following the principle of Huygens, becomes source of spherical waves of the same wavelength of the incoming radiation. We can distinguish between Fresnel and Fraunhofer diffraction [3]. If we take a scale factor defined as $d^2/2\lambda$, where d is the object dimension and λ the wavelength, we can roughly speak of Fresnel diffraction when at least one of the relevant distances source–object (D1)or object-detector (D2) are smaller or of the same order of $d^2/2\lambda$. Fraunhofer diffraction will take place when both the relevant distances $D >> d^2/2\lambda$ and therefore plane wave approximation is valid. Bragg diffraction is a special case of Fraunhofer diffraction: if many objects interact with the incoming wave-front (that we suppose a plane wave) the resulting field is the superposition of the spherical wavelets emitted by all the objects. If they are disposed in an ordered array, like in a crystal, the superposition will give rise to constructive interference only for given directions where the wavelets are in phase, otherwise destructive interference will take place. This is the basis of Bragg diffraction. The simple formula which express the condition for constructive interference has been expressed by W.L. Bragg in 1913 [4] who considered the crystal as composed of sets of parallel planes of ions. The Bragg law is then:

$$\lambda = 2\, d \sin\vartheta \qquad \textbf{(2.2)}$$

Where λ is the wavelength, d the interplanar distance and ϑ the angle of incidence of the incoming (monochromatic) radiation onto the lattice plane.

2.2 Optics for X-Ray microscopy

Many types of X-ray optics have been developed to improve the flux density (flux per unit area) woth the purpose to make possible different kind of X-ray microscopy (X-ray imaging, X-ray fluorescence microscopy, X-ray diffraction microscopy, etc.). Here we will briefly describe just two types of X-ray optics: diffractive optics (zone plates) and reflection optics (mirrors), because they are the most commonly used for X-ray microscopy.

2.2.1 Diffractive optics: zone plates

The zone plate is so called because it is constructed following the Fresnel-zone law:
A plane opaque screen with a circular aperture of radius d illuminated by coherent radiation (i.e. a plane wave) produces, at a generic distance z from it (Figure 2.1), the usual diffraction pattern of lighter and darker rings on a screen normal to the z-axis.

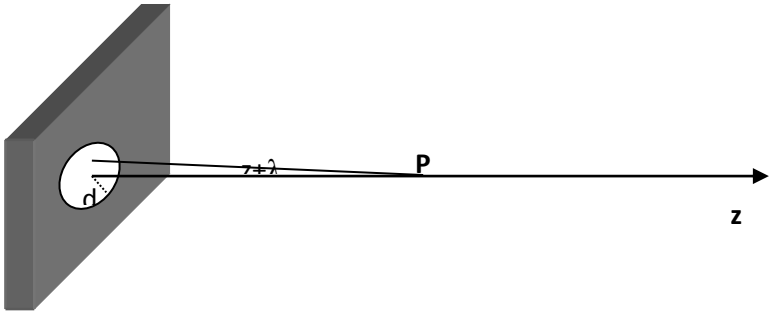

Figure 2.1: *Opaque screen with a circular aperture of radius d. The points on the aperture distant z+λ/2 from P define the radius of the first Fresnel zone for the point P.*

This diffraction pattern is not of interest here and the analysis will be focused on the diffraction along the z-axis alone. The field amplitude W(z) along the z-axis oscillates depending on the $d^2/\lambda z$ ratio according to the following relation [3]:

$$W(z) = Ae^{-ikz}\left(1 - e^{-i\pi N_F}\right) = -2iAe^{-i\left(kz+\frac{\pi}{2}N_F\right)}\sin\left(\frac{\pi N_F}{2}\right) \qquad \textbf{(2.3a)}$$

where:

$$N_F = \frac{d^2}{\lambda z} \qquad \textbf{(2. 3b)}$$

is the Fresnel number. Different regions of the aperture emit radiation, which interferes constructively or destructively depending on the distance z. For any given point P on the z axis, it is convenient to classify the regions on the z = 0 plane (where the aperture is located) depending on the constructive or destructive interference produced in P. These regions are named Fresnel zones.

The first Fresnel zone for the point P distant z from the screen is the circle of radius r_1

$$r_1^{\,2} = \left(z + \frac{\lambda}{2} \right)^2 - z^2 \approx \lambda z$$

It identifies the points on the z=0 plane at a distance smaller than z+λ/2 from P. The radiation emitted from these points interferes constructively in P since the optical path lengths differ by less than λ/2. The field generated by this circle in P is easily obtained from (2.3a) by taking d=r_1 and therefore N_F=1:

$$W_1 = Ae^{-ikz}\left(1 - e^{-i\pi}\right) = 2Ae^{-ikz} \qquad \textbf{(2. 4)}$$

So that its amplitude is twice larger than the field amplitude in the absence of the screen. In other words, if the aperture had a radius d=r_1, then the whole radiation passing through it would interfere constructively in P thus explaining the increased intensity.

The second Fresnel zone is a ring of internal radius r1 and external radius given by:

$$r_2^2 = \left(z + \lambda\right)^2 - z^2 \approx 2\lambda z$$

The field produced at P by the points in this second Fresnel zone is obtained by setting d= r_2 in (2.3b) and subtracting the field produced by the points in the first zone:

$$W_2 = Ae^{-ikz}\left[\left(1 - e^{-2i\pi}\right) - \left(1 - e^{-i\pi}\right)\right] = -2Ae^{-ikz} \qquad \textbf{(2.5)}$$

As it is apparent from the negative sign, if the aperture had a radius d=r_2, the radiation from the first Fresnel zone would interfere destructively with the radiation coming from the second one and the intensity in P would vanish.

The radius of the generic nth zone is:

$$r_n = \sqrt{n\lambda z} \qquad \text{n=1,2..} \qquad \textbf{(2.6)}$$

It is important to notice that the Fresnel zones are independent on the size of the aperture and they only depend on the position of P and on the wavelength.

For a point at distance z the number N_F in (2.3b) is the number of Fresnel zones contained in the aperture. In particular, if this number is an even integer the interference of the radiation from the

various zones is destructive and the intensity in P is zero. If NF is an odd integer, the radiation from one whole zone is unbalanced and the intensity is maximal.

The Fresnel zone plate (FZP) is a screen of alternately transparent and opaque zones equal in size to the Fresnel zones. The efficiency is quite poor, because a relevant part of the incoming radiation is simply lost. An advancement is constituted by the phase zone plate. In the phase zone plate the opaque zone is substituted with a material which introduces a chane of pahse of π. In this way both the odd and the even zones contribute to the total intensity, thus improving the ZP efficiency.

Illuminating the screen with a plane wave, for $m \neq 0$ the zone plate produces spherical waves with r_1 the radius of the innermost zone, n the zone number and m the number of diffracted order, the focal length fm of a zone plate being approximately:

$$\frac{k}{2f_m} = \frac{\pi m}{r_1^2} \quad \Rightarrow \quad f_m = \frac{r_1^2}{m\lambda} \tag{2.7}$$

It is important to notice that the position of the focal point depends on the wavelength.

The width of the outermost zone of a zone plate can approximately be written as:

$$dr_n = \frac{r_n}{2n} \tag{2.8}$$

One of important characteristic of the zone plate is the resolution Δ which can be expressed, according to the Rayleigh criterion [5,6], as:

$$\Delta = 1.22\frac{dr_n}{m} \tag{2.9}$$

where dr_n is the width of the outermost zone of the ZP. This represents the best possible resolution of the zone plate, but other factor can influence the effective spot size, such as a limited distance between source and ZP, and the non perfect monochromaticity of the beam.

The zone plates are mainly used for imaging. In this case, a condenser ZP lens concentrate the flux on a limited area of the sample, and an objective ZP lens gives a sample magnified view on the detector. The ZP lenses are mostly used in the soft X-ray region, where X-ray microscopy, especially in the water window, is able to reach resolution of the order of few tens of nanometers. In the hard X-ray region they are not very efficient, because the opaque zone should have a too large

aspect ration (ratio between thickness and width), to block, or even to introduce a π change of phase, if high spatial resolution is needed.

2.2.2 Total reflection optics: Kirkpatrick-Baez mirrors

An interesting optics to focus hard X-rays is given by grazing incidence total-reflection mirrors. A pair of elliptical mirrors arranged in a crossed mirror geometry (Kirkpatrick-Baez configuration) is able to focus X-ray to sub-micron size (Figure 2.2).

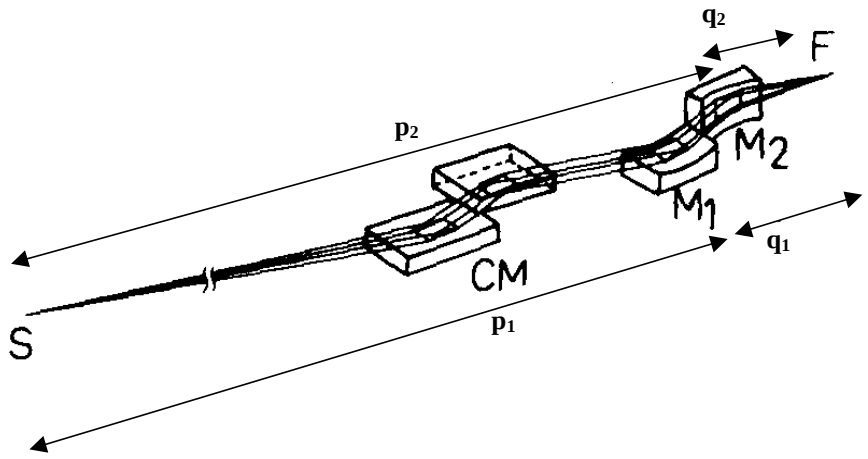

Figure 2.2: *Schematic diagram of the optical system of two crossed Kirkpatrick-Baez curved mirrors to form a demagnified image of an X-ray source.*

The X-ray beam passing through a Si (111) symmetric double crystal monochromator (CM) is focused by the elliptical mirrors. The radiation incident on the first mirror (M_1) is vertically focused. The reflected beam from M_1 is incident on the second mirror (M_2) which horizontally focuses the beam.

To achieve a focused image it is necessary to satisfy the focus equations at the centre of the first and second mirrors:

$$\frac{1}{p_1}+\frac{1}{q_1}=\frac{2}{R_1\sin\theta_1}; \qquad \frac{1}{p_2}+\frac{1}{q_2}=\frac{2}{R_2\sin\theta_2}$$

where p_1,q_1 , p_2,q_2 are clear from Figure 2.3, R_1 and R_2 are the mirror radius of curvature and θ_1 and θ_2 are the angles of glancing incidence for the first and second mirror respectively. For the simple case of cylindrical mirrors, the following conditions are fulfilled:

$$p_2 = p_1 + s \qquad q_2 = q_1 - s$$

where *s* is the distance between mirror centres.

When multilayer mirrors are used, it is additionally necessary to satisfy the Bragg equation for each mirror:

$$2d_1 \sin\theta_1 = 2d_2 \sin\theta_2 = m\lambda$$

where d_1 and d_2 are the periods of the multilayers and m is the reflection order.

Combining the equations given above one arrives to the following expression:

$$\frac{d_1 R_2}{d_2 R_1} = \left(1 + \frac{s}{p_1}\right) \frac{\left(K_1 - \frac{s}{p_1}\right)}{K_1}$$

where K_1 is the magnification of the first mirror ($K_1 = q_1/p_1$). It is important to note that for high de-magnification of the source (i.e. small beam size), p_1 and p_2 must be much larger than q_1 and q_2, respectively. In general the magnification of the second mirror $K_2 = q_2/p_2$ is different from that of the first one and for the special case of identical radii and periods one can find:

$$K_1 = \frac{1}{K_2}$$

Kirkpatrick and Baez (KB) developed this crossed mirror geometry to eliminate astigmatism of a single spherical (or cylindrical) mirror used at glancing incidence. The spatial resolution of the KB system was limited mainly by spherical aberration. Therefore, the mirrors with elliptical cylinder shapes instead of spherical or cylindrical are used to remove spherical aberration.

The advantages with respect to other focusing optics are that optical system with small aberration can be designed, the focusing properties do not depend on the incident X-ray energy, some types of mirror figure can be manufactured with high accuracy and the working distance from the focusing element to the sample can be relatively long. Nanometer beam size can be achieved using high quality KB mirror systems.

In the beamline ID16A, where the experiments have been carried out, the distance of the end station from the source is very high (185 m). This long distance is necessary to have a high de-magnification factor, and to reach in this way nanometer beam size. The beamline is optimised for high-resolution quantitative 3D imaging techniques with a specific focus on X-ray fluorescence and projection microscopy and is mainly dedicated to problems in biology, biomedicine and

nanotechnology. It is optimised for hard X-ray focusing of the beam (< 20 nm) at specific energies (17 and 33.6 keV, $\Delta E/E \sim 10^{-2}$). The beamline uses fixed curvature multilayer coated KB optics. A detailed description of the beamline is done in chapter V.

2.3 X-ray Fluorescence Microscopy

As seen before, one of the basic interaction of X-rays with matter is the photoelectric absorption In this process a photon is absorbed by an atom creating a hole in the atom with the ejection of an electron. The energy of this photo-electron is the difference between that of the incident photon and the binding energy of the electron. The electron vacancies created by the incoming photon are filled by electrons cascading in from outer electron shells. These have higher energy states than inner shell electrons, and the rearrangement of electrons results in emission of Auger electrons and of X-ray photons characteristic of the given atom (Figure 2.3).

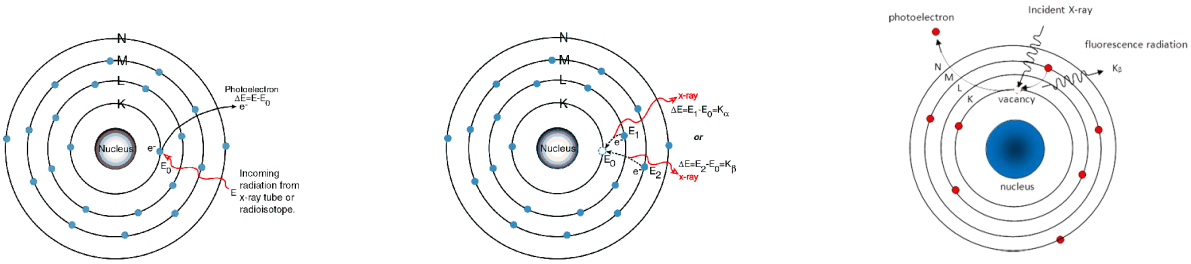

Figure 2.3: *Schematic picture of the X-ray fluorescence. The inner shell electron hit by the energetic photon is expelled from the atom. The vacancy is filled by other electrons and characteristic X-ray radiation is emitted.*

This emission of photons is called X-ray fluorescence and it is emitted isotropically. The X-ray fluorescence lines are historically termed by the letter K, L, or M (Figure 2.4), indicating which shell had the original vacancy, and by a subscript alpha (α) or beta (β), which indicates the higher shell from which electrons fell to fill the vacancy and produce the X-ray. For example, a Kα line is produced by a vacancy in the K shell filled by an L shell electron, whereas a Kβ line is produced by a vacancy K shell filled by an M shell electron. The K lines are by far the most intense; moreover, the Kα transition is on average 6 to 7 times more intense than the Kβ ones. Therefore, the Kα line is in general the choice for quantification purposes. Obviously, to generate K lines the incoming photons must have enough energy to excite the innermost electrons.

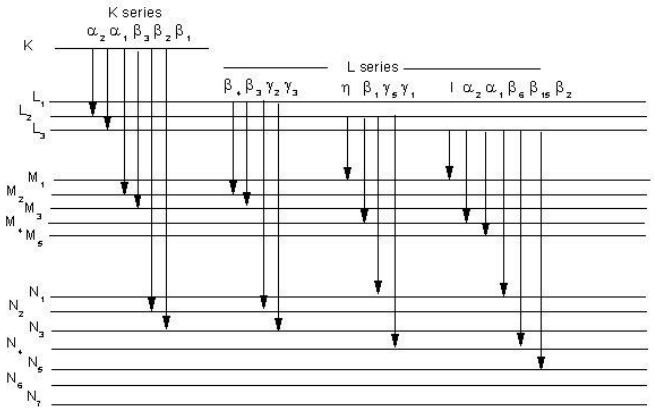

Figure 2.4: *Nomenclature of X-ray transitions.*

Since the X-ray fluorescence spectrum is characteristic and different for each elements, X-ray fluorescence spectroscopy has been used since the discovery of X-rays for elemental analysis. However, only with the advent of third generation synchrotron radiation sources, the X-ray Fluorescence Microscopy (XRFM) could become a technique able to give information at micrometer and sub-micrometer scale. This because the generation of X-ray fluorescence photons is very inefficient, and only with SR it is possible to obtain an intense finely focused X-ray beam able to get measurable fluorescence intensity from very small volumes. Furthermore, the monochromatic beam and the polarization of the synchrotron beam improves the Signal/background ration, which is one of the most important figure of merit in fluorescence analysis. Anyway, in relatively few years XRFM has opened up new applications, such as trace element analysis, surface analysis, chemical state analysis and microanalysis [7]. XRFM works in scanning mode. Digital images of the sample at micrometer or nanometer spatial resolution are built, pixel by pixel, by scanning the sample through the beam. The resulting X-ray fluorescence spectrum is characteristic of the chemical elements at that pixel. Mathematical deconvolution of the fluorescence spectrum reveals the chemical composition, from which quantitative elemental images of the sample are assembled. One of the most important application is in the biomedical field. XRFM provides an excellent trace element sensitivity; and, due to the large penetration depth of hard X-rays, an opportunity to image whole cells and quantify elements on a per cell basis. Moreover, because specimens prepared for XRFM do not require sectioning, they can be investigated close to their natural, hydrated state with cryogenic approaches [8], [9].

However, a limitation of XRFM resides in its pixel-by-pixel nature that, combined with the low sensitivity and slow readout of conventional energy dispersive X-ray detectors, severely limits the size of images that can be made during a scan. For example acquiring images of just 200 x 200 pixels with a dwell time of 100 ms would take more than 1 h.

The advantages of synchrotron-based XRFM over conventional XRFM derive directly from the characteristics of synchrotron radiation (see Chapter I). While comparing synchrotron-based XRFM, analysis with other alternative possibilities one must highlight the much higher sensitivities and lower detection limits achievable at synchrotron light sources. The sensitivity, defined as the detected signal intensity from a unit mass per unit of time, is proportional to the incident X-ray intensity. It can be sufficiently enhanced due to the photon flux density, which at synchrotron sources is modulable through focusing. In addition, the high degree of polarization of synchrotron radiation is beneficial, causing spectral backgrounds due to scatter to be greatly reduced when the detector is placed at 90° to the primary beam and in the storage ring plane. An important aspect of XRFM analysis is the Signal to Background ratio (S/B). While in the case of continuous (white) spectrum of radiation this value is not the best, it turns out to be optimum with the use of monochromatic excitation. The excitation energy should be slightly higher than the absorption edge to avoid overlapping of the fluorescent signal with the elastically and inelastically scattered radiation. The value closely related to S/B ratio is the minimum detection limit (MDL) formulated as:

$$MDL = 3\sigma(I_B)C_F/I_F \qquad \textbf{(2.10)}$$

where I_B, I_F are the background and fluorescence signal intensities respectively, C_F is the concentration of the measured sample and $\sigma(I_B)$ is the uncertainty of the I_B below the peak of interest. The value of MDL strongly depends on the experimental conditions and on the sample matrix and for the synchrotron monochromatic radiation it is situated at the sub-ppm level [8].

2.4 X-Ray Phase Contrast Imaging

Absorption radiology is the most common way imaging is working since the X-ray imaging was born.The absorption contrast depends only on the linear absorption coefficient μ and it is independent on the spatial degree of coherence of the beam. Instead, phase contrast imaging such as that based on free space propagation (defocused imaging) requires some degree of coherence of the incident beam. This technique permits to image weak absorbing samples that would not provide enough contrast in absorption. A typical example are biological samples. With the third generation

synchrotron radiation sources generating a highly coherent beam, many techniques based on phase imaging have been developed.

The main difficulty in phase contrast imaging is that the phase cannot be measured directly and therefore several indirect methods have been developed to transform phase modulations into intensity modulations. The principle of the free space propagation phase imaging is that differences in optical path for the beam transmitted through an object are directly converted, after interference, into inhomogeneous intensity, hence contrast.

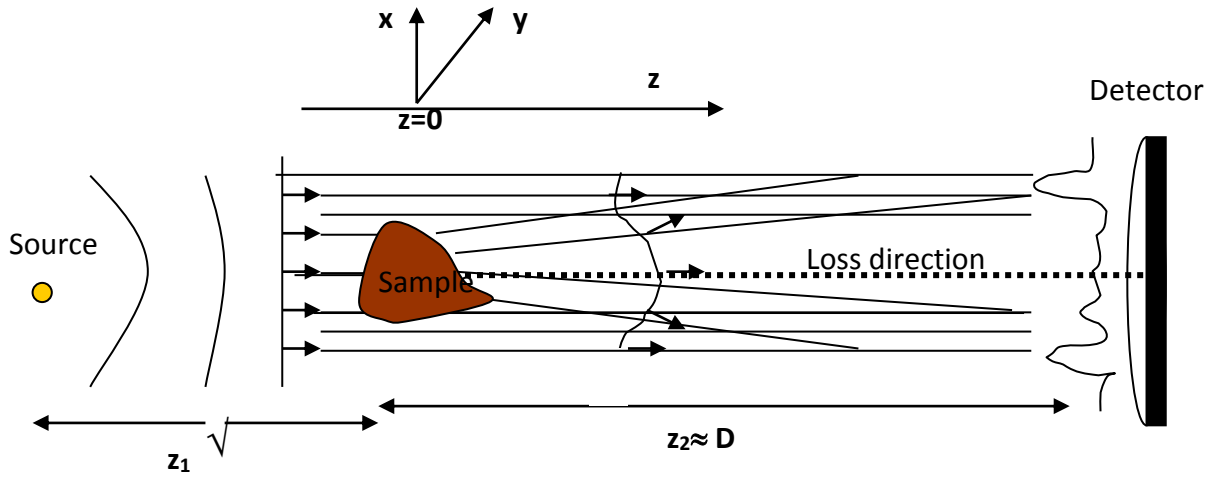

Figure 2.5: *Schematic representation of the set-up used to record the defocused image. The incoming plane wave is deformed by the modulation of the index of refraction inside the sample. The direction of propagation is perpendicular to the wavefront.*

The propagated field A_D at a distance D can be considered as the convolution between the field A_0 at z=0 and a kernel (propagator) P_D which represents the propagation:

$$A_D(\boldsymbol{r}) = \iint_{\infty} d\bar{\boldsymbol{r}}\, A_0(\bar{\boldsymbol{r}}) \iint_{\infty} \boldsymbol{e}^{-2\pi i[\boldsymbol{f}(\boldsymbol{r}-\bar{\boldsymbol{r}})]} e^{-ik_z D} d\boldsymbol{f} = \iint_{\infty} A_0(\bar{\boldsymbol{r}}) P_D(\boldsymbol{r}-\bar{\boldsymbol{r}}) d\bar{\boldsymbol{r}} \qquad \textbf{(2.11)}$$

where **r** = (x,y) and $\bar{\boldsymbol{r}} = (\bar{x}, \bar{y})$ identify points on the image and object planes respectively, **f**=(p,q) where p and q are spatial frequencies [10]:

$$p = \frac{k_x}{2\pi} \qquad q = \frac{k_y}{2\pi} \qquad \textbf{(2.12)}$$

$$k_z = \sqrt{\left(\frac{2\pi}{\lambda}\right)^2 - (2\pi p)^2 - (2\pi q)^2}$$

and

$$P_D(\boldsymbol{r}) = \iint_{\infty} e^{2\pi i(\boldsymbol{fr})} e^{-ik_z D} d\boldsymbol{f} \qquad \textbf{(2.13)}$$

The problem of propagation can be better solved by decomposing the field after the object (A_o) into plane waves and by describing the effect of propagation from the sample to the image plane as a linear filter, i.e. by applying Fourier transformation.

In the Fourier space the convolution becomes the product between the Fourier transformed functions.

$$\tilde{A}_D(\boldsymbol{f}) = \tilde{A}_0(\boldsymbol{f}) \cdot \tilde{P}_D(\boldsymbol{f}) \qquad \textbf{(2.14)}$$

To describe the image formation in phase contrast, we can start from the definition of the transmission function of the object as:

$$T(x,y) = \frac{A_0(x,y)}{A_i(x,y)} \qquad \textbf{(2.15)}$$

where A_0 is the field emerging from the object at z=0 and A_i is the incident field. Here we consider propagation along the z axis.

Starting from the definition of the refraction $r = n - i\beta = 1 - \delta - i\beta$ (see par. 2.1), the transmission function of the object can be written as:

$$T(x,y) = e^{i\varphi(x,y)} e^{-\mu(x,y)} \qquad \textbf{(2.16)}$$

or:

$$T(x,y) = M(x,y) e^{i\varphi(x,y)} \qquad \textbf{(2.17)}$$

T(x,y) describes the action of the object on the incident beam, and therefore it involves the real and the imaginary part of the refraction index of the object itself:

$$M(x,y) = \exp\left[-\frac{1}{2}\int \mu(x,y,z)dz\right]$$
$$\varphi(x,y) = \frac{2\pi}{\lambda}\int \delta(x,y,z)dz \qquad \textbf{(2.18)}$$

If the object does not modify the phase of the incident field A_i but only its amplitude, it is an amplitude object. If it modifies the phase and M(x, y) is independent on x and y, the object is a pure phase object.

For objects, which are well approximated as weak phase and weak absorption objects, the transmission function (eq 2.19) can be written, expanding the exponential:

$$T(x) \sim 1 + i\varphi(x) - \mu\ (x) \qquad \textbf{(2.19)}$$

For simplicity, we consider here only a one-dimensional object, with coordinate x. The application to 2-D objects is trivial. Illuminating the object represented by the transmission function T with a coherent plane wave, the imaged intensity on the object plane is proportional to the square modulus of T(x) and therefore the recorded intensity does not give information on the phase φ(x). However, in phase contrast imaging the image is not taken close to the sample, but at a certain distance D from it. The distance D is called the defocusing distance, and if the incoming field is a plane wave it simply corresponds to the distance between the sample and the detector. The free-space propagation from sample to detector allows the wavelets exiting the sample to interfere. This creates black-white fringes at the detector, whose analysis gives information about the phase changes, and therefore about the sample refraction index. We therefore have to consider propagation from the sample to the detector. Recalling eq. (2.11), the field A_D at a certain distance D from the sample illuminated by a coherent field can be described as the convolution of the field emerging from the sample A_o and a propagator P_D .Considering eq. 2.15, we can write:

$$A_D^{coh}(x) = \int A_i(x_0) T(x_0) P(x - x_0) dx_0 \qquad \textbf{(2.20)}$$

As pointed out before, to deal with propagation is better to work in the Fourier space. We can then take the Fourier transform of T(x):

$$\tilde{T}(f) = \delta_D(f) + i\tilde{\varphi}(f) - \tilde{\mu}(f) \qquad \textbf{(2.21)}$$

where δ_D is the Dirac distribution and *f* is (in one dimension) the spatial frequency. The Fourier transform of the propagator $\tilde{P}_D$ can be expressed in the simple form [10]:

$$\tilde{P}_D = \cos(\pi\lambda D f^2) + i\sin(\pi\lambda D f^2) \qquad \textbf{(2.22)}$$

The Fourier transform of the amplitude can then be written [Pogany, 1997]:

$$\tilde{A}_D^{coh}(f) = \tilde{T}(f)\cdot\tilde{P}_D(f) = \delta_D\cos(\pi\lambda Df^2) + i\delta_D\sin(\pi\lambda Df^2) + i\tilde{\varphi}(f)\cos(\pi\lambda Df^2) + \\ -\sin(\pi\lambda Df^2)\tilde{\varphi}(f) - \tilde{\mu}(f)\cos(\pi\lambda Df^2) - i\tilde{\mu}(f)\sin(\pi\lambda Df^2) =$$

$$= \left[\delta_D(f) - \tilde{\varphi}(f)\sin(\pi\lambda Df^2) - \tilde{\mu}(f)\cos(\pi\lambda Df^2)\right] + i\left[\tilde{\varphi}(f)\cos(\pi\lambda Df^2) - \tilde{\mu}(f)\sin(\pi\lambda Df^2)\right] \quad \textbf{(2.23)}$$

Therefore:

$$A_D{}^{coh}(x) \approx \left[1 - \mu\otimes\cos\tilde{}\left(\pi\lambda Df^2\right) - \varphi\otimes\sin\tilde{}\left(\pi\lambda Df^2\right)\right] + i\left[\varphi\otimes\cos\tilde{}\left(\pi\lambda Df^2\right) - \mu\otimes\sin\tilde{}\left(\pi\lambda Df^2\right)\right] \quad \textbf{(2.24)}$$

and to first order in φ and μ the intensity can be written:

$$I_D^{coh}(x) \approx 1 - 2\mu\otimes\cos\tilde{}\left(\pi\lambda Df^2\right) - 2\varphi\otimes\sin\tilde{}\left(\pi\lambda Df^2\right) \quad \textbf{(2.25)}$$

Going once more to the Fourier space the expression for A_D^{coh} can be easily simplified. Taking only the leading order in μ and φ , we can obtain [Cloetens, 1996]:

$$\tilde{I}_D^{coh}(f) = \delta_D(f) - 2\sin\left(\pi\lambda Df^2\right)\tilde{\varphi}(f) - 2\cos\left(\pi\lambda Df^2\right)\tilde{\mu}(f) \quad \textbf{(2.26)}$$

From this the field can be written:

$$\tilde{A}_D^{coh}(f) = \delta_D(f) - \sin\left(\pi\lambda Df^2\right)\tilde{\varphi}(f) - \cos\left(\pi\lambda Df^2\right)\tilde{\mu}(f) \quad \textbf{(2.27)}$$

The expansion leading to expressions (2.26) and (2.27) is valid [Guigay, 1977; Cloetens, 1996] provided the phase varies smoothly according to:

$$\left|\varphi(x) - \varphi(x - \lambda Df)\right| << 1$$

The δ_D corresponds to a homogeneous background in the image. As it is clear from (2.2), the phase modulation has been transformed in a detectable intensity modulation.

From the coefficients $\tilde{\varphi}$ and $\tilde{\mu}$ in (2.2), it is apparent that the absorption will in general complement phase contrast. In particular, for a given spatial frequency range spatial details of order $d \approx \frac{1}{f}$ will be resolved due to either phase contrast or absorption contrast.

Optimal phase contrast is obtained when the coefficient of $\tilde{\varphi}(f)$ in (2.2) is maximum, i.e. for the frequency [Cloetens, 1996]:

$$f_{\max} = \frac{1}{\sqrt{2\lambda D}} \quad \textbf{(2.28)}$$

For this value of f the contrast due to absorption is minimal ($\cos(f_{max})=0$) and the phase contrast is maximal. On the other hand at D = 0 the phase drops and, as seen in the previous subsection, there is only absorption contrast. For frequencies around f_{max}, the intensity in (2.26) becomes:

$$\tilde{I}_D^{coh}(f) \approx \delta_D(f) - 2\tilde{\varphi}(f) \qquad \textbf{(2.29)}$$

Depending on the defocusing distance, there are three different regions of interference, near-edge, Fresnel and Fraunhofer, having different interference characteristics. In the near-edge region in practice only the edges gives detectable contrast with a characteristic black-white fringe. In the Fresnel region a complex system of fringes is built, whereas in the Fraunhofer region the image is the Fourier transform of the object transmission function.

With the phase retrieval procedure, it is possible to obtain the spatial distribution of the sample refractive index, in its real and imaginary components, starting from the analysis of the images at the detector. This is the so-called inverse problem. Several algorithms have been developed, here we will use the transfer function approach [Cloetens 1996]. In the case of biological samples, the absorption can be neglected, and only variations of phase must therefore be considered, i.e.the sinus term in 2.26 and 2.27. From these equations it appear that different defocusing distances are optimal for different spatial frequencies. In order to reconstruct the phase, it is therefore convenient to make inages at several defocusing distances. In this way, it is possible to optimize the response for all the spatial frequencies, and to avoid "blindness" for some frequency. In the experiment, we made imaging at four distances.

The phase retrieval procedure is based on minimization of the difference between the measured and the calculated intensity distributions using the least square criterium:

$$\tilde{\phi}(f) = \frac{1}{N}\sum W_m(f)\tilde{I}_m^{\exp}(f) \qquad \textbf{(2.30)}$$

$$W_m = \frac{\sin\left(\pi\lambda D_m |f|^2\right)}{\frac{1}{N}\sum 2\sin^2\left(\pi\lambda D_m |f|^2\right)} \qquad \textbf{(2.31)}$$

Up to now, we considered illumination by a plane wave. However, to get magnified image of the sample, a divergent beam must be used. In beamline ID16A the mirrors focalize in a very small spot. Thje sample is displaced from the focus position a distance z_1, and the detector is placed at a distance z_2 from the sample. In this way a magnified view of the sample is obtained, with a

magnification ratio $M = (z_1 + z_2)/z_1$ In this magnifying geometry, the defocusing distance D becomes:

$$D_{mag} = (z_2\, z_1)/ (z_2 + z_1) \quad \textbf{(2.32)}$$

All the equations desfribed before are still valid substituting D with D_{mag}. In practice, however, since z_2 is much larger than z, $D_{mag} \approx D$.

2.5 X-Ray Nanotomography

Tomography, involves the process of recording several radiographs of a sample at different angular positions (Figure 2.6), which can then be used to reconstruct its inner composition in 3D. This technique can be applied in many scientific areas, among them material science, paleontology, cultural heritage, biomedical sciences, on scales ranging from macro to nano. It is usually known as Computed Tomography (CT), in which reconstruction of such projection data sets are done by computer processing.

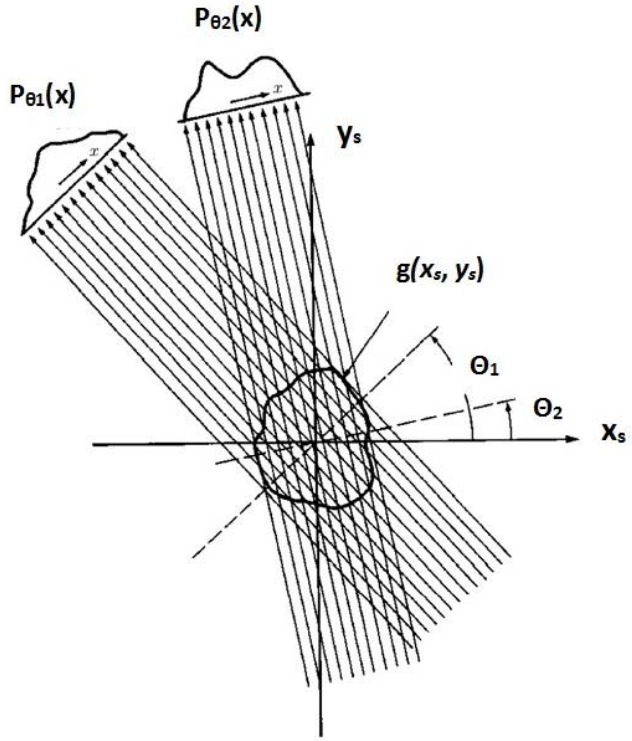

Figure 2.6: *The principle of tomography: parallel projections are acquired over a range of angular positions.*

2.5.1 Principle of tomography

As we know from the paragraph 2.5 the modifications to the incoming waveinduced by the object as projections through the absorption and refractive index distributions can be described respectively, with:

$$B(x) = (2\pi/\lambda)\int \beta(x,y,z)dz \qquad \textbf{(2.33)}$$

$$\phi(x) = (2\pi/\lambda)\int \delta n(x,y,z)dz \qquad \textbf{(2.34)}$$

Choosing the sample as our reference point, the sample cross-sectional coordinate system $x_s = (x_s, y_s)$ is fixed relative to the sample. The imaging plane and propagation direction coordinate system (x,y,z) will appear to rotate relative to the sample, and the relation between the two systems will be dependent on the angle of incidence of the beam relative to x_s (Figure 2.7).

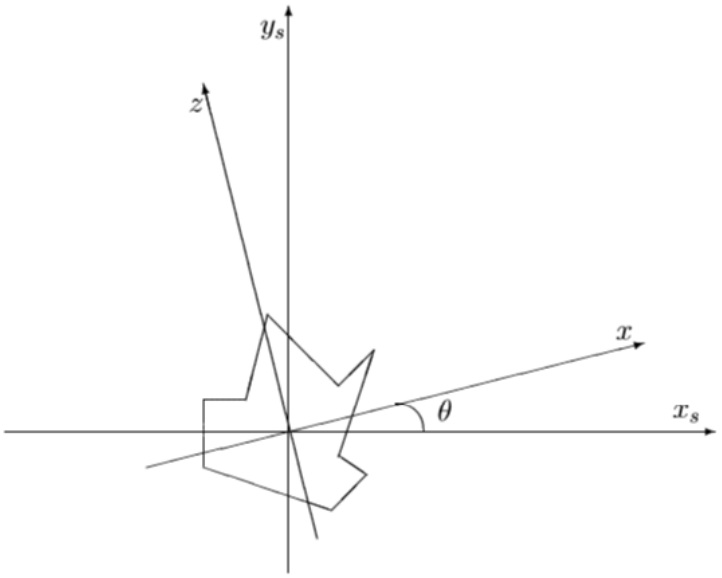

Figure 2.7: *Coordinate systems used in tomography. (x_s,y_s) are fixed to the sample. The beam propagation and image plane coordinate system (x,z) seems to rotate around the object.*

We start describing the tomographic procedure considering just absorption. Given a row of the absorption (Eq. 2.33), we can define a projection through the sample along a line in the beam direction $L_{\theta,x}$ for a fixed angle θ and position along x as:

$$B\theta(x) = (2\pi/\lambda) \int_{L\theta,x} \beta(xs)ds \qquad \textbf{(2.35)}$$

It is from this set of projections over the angle θ (Fig. 2.6) that we want to reconstruct the 2D absorption index distribution $\beta(x_s,y_s)$.

2.5.2 Fourier slice theorem

Consider again the (x,z) coordinate system in Figure 27. Change between the (x,z) and (x_s,y_s) systems can be described by a rotation (Kak and Slaney, 1998).

$$\begin{pmatrix} x \\ z \end{pmatrix} = \begin{pmatrix} \cos\Theta & \sin\Theta \\ -\sin\Theta & \cos\Theta \end{pmatrix} \begin{pmatrix} x_s \\ y_s \end{pmatrix} \quad \textbf{(2.36)}$$

A projection $P_\theta(x)$ along lines of constant x through an arbitrary object function $g(x_s,y_s)$ is given in the (x,z) coordinate system as:

$$P_\theta(x) = \int_{-\infty}^{\infty} g(x,z)dz \quad \textbf{(2.37)}$$

Taking the Fourier transform of this projection, we have:

$$\tilde{P}_\theta(f_x) = \int P_\theta(x)\exp(-i2\pi f_x(x))dx \quad \textbf{(2.38)}$$

Substitution of Eq. 2.37 into Eq. 2.38 gives:

$$\tilde{P}_\theta(f_x) = \int\int g(x,z)\exp(-i2\pi f_x(x))dxdz \quad \textbf{(2.39)}$$

By using the coordinate transformation in Eq. 2.36, we can transform Eq. 2.39 into the (x_s,y_s) coordinate system:

$$\tilde{P}_\theta(x) = \int\int g(x,z)\exp\{-i2\pi f_x[x_s \cdot n(\theta)]\}dx_s \quad \textbf{(2.40)}$$

where $n(\theta) = (\cos\theta,\sin\theta)$. This is nothing else than the two-dimensional Fourier transform of the object function at the spatial frequencies ($u = f_x\cos\theta$, $v = f_x\sin\theta$), which can be written as:

$$\tilde{P}_\theta(f_x) = \bar{g}(f_x\cos\theta,\sin\theta) = \tilde{g}(u,v) \quad \textbf{(2.41)}$$

This is the central result of straight ray tomography: the Fourier transform of a parallel projection through an object is the 1D Fourier transform along a line through the 2D object Fourier transform (Figure 2.8).

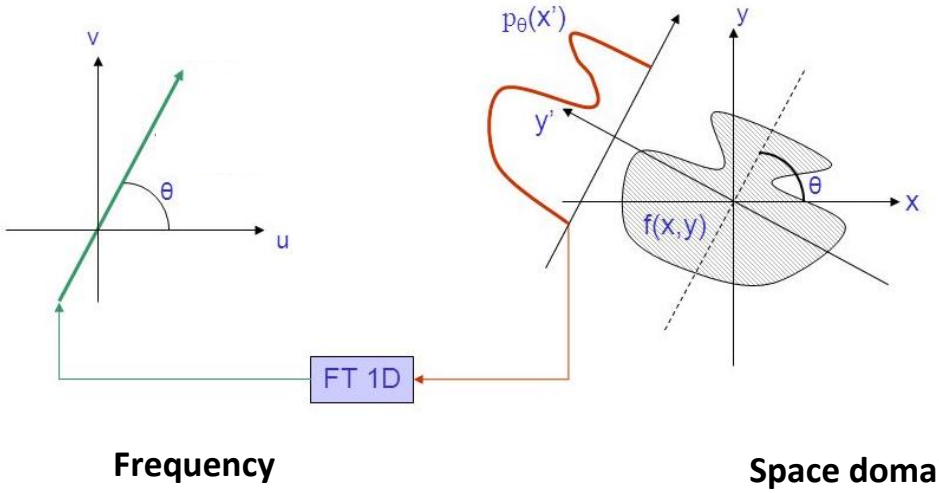

Figure 2.8: *Illustration of the Fourier slice theorem. The Fourier transform of a parallel projection through an object at an angle θ is equal to the values along a line through the 2D Fourier transform of the object with the same pitch θ.*

2.5.3 Fourier reconstruction

The Fourier slice theorem can be used to devise a conceptually simple tomographic reconstruction algorithm. From a set of projections, we can determine the values of $\tilde{g}$ (u) on radial lines (Fig. 2.14). If we could take an infinite number of projections, then $\tilde{g}$ (u) would be known in every point in the frequency domain. The object function could then be easily recovered by the inverse Fourier transform,

$$g(x_s) = \int\int \tilde{g}(u)\exp(i2\pi \cdot x_s)du \qquad \textbf{(2.42)}$$

where**: u** = (u,v).

The data obtained by Fourier transforming projections lie on a polar grid, and not an Euclidean one, and to go from one to the other requires advanced interpolation techniques.

2.5.4 Filtered back-projection

Another reconstruction algorithm can be formulated by considering Eq. 2.38 in a different way. If we change to polar coordinates in Eq. 2.38 and substitute u = $f_x \cos\theta$ and $v = f_x \sin\theta$, we obtain:

$$g(x_s) = \int_0^{2\pi}\int_0^{\infty} \tilde{g}(f_{x,}\theta) f_x \exp\{i2\pi f_x[x_s \cdot n(\theta)]\}df_x d\theta \qquad \textbf{(2.43)}$$

Using the Fourier slice theorem (Eq. 2.35), that is substituting $\tilde{P}_\theta(f_x)$ for $\tilde{g}(f_x,\theta)$ we get:

$$g(x_s) = \int_0^{\pi} \int P_\theta(x) h([x_s \cdot n(\theta)] - x) dx d\theta \quad \textbf{(2.44)}$$

Where h is the reconstruction filter.

We can observe that Eq. 2.42 can be rewritten as:

$$g(x_s) = \int_0^{\pi} Q_\theta(x_s \cdot n\ (\theta)) d\theta$$

$$Q_\theta(x) = \int P_\theta(x') h(x - x') dx' \quad \textbf{(2.45)}$$

$Q_\theta(x)$ is the convolution of $P_\theta(x)$ with h(x), the filtered projection, $g(x_s)$ is the sum of all $Q_\theta(x)$ over θ. For a certain projection angle θ_i, each point (x_s,y_s) in the object function is given the value in $Q_{\theta i}(x)$ with $x = x_s \cos\theta_i + ys \sin\theta_i$. It is easy to see that points along lines parallel to the projection direction will be given the same value. This algorithm is known as filtered backprojection and can be considered as the standard tomographic reconstruction algorithm [Kak and Slaney, 1998].

The number of projections, which have to be acquired, is given by the sampling theorem. To achieve sufficient sampling in the Fourier domain, the number of projection angles should be large enough to sample the highest frequency uniformly, that is the same angular rate as radial. If we let N be the number of picture elements horizontally, along the detector, M the number of projection angles and |fmax| the maximum radial frequency, the distance A between two points in the radial direction is:

$$A = \frac{4\pi |f_{max}|}{N} \quad \textbf{(2.46)}$$

The tangential distance between two points is:

$$B = 2\pi |f| \Delta\theta = \frac{2\pi^2 |f_{max}|}{M} \quad \textbf{(2.47)}$$

If we require the tangential distance B to be at least as small as A, we have:

$$M \approx \frac{\pi |}{2} N \quad \textbf{(2.48)}$$

2.5.5 Phase contrast tomography

From Eq. 2.34, we can see that the procedure for pure phase tomographic reconstruction is the analogue of the absorption tomographic reconstruction, substituting the absorption B with the phase Φ. Therefore, for phase contrast tomography, it is necessary to carry on initially the phase retrieval

procedure described in the previous paragraph for each projection, and then the tomographic reconstruction.

Riassunto del Capitolo 2 in Italiano

In questo capitolo sono presentati i principi teorici alla base della generazione dei raggi X in una sorgente da sicrotrone come quella di ESRF. Sono qui brevemente descritti i differenti tipi di interazione dei raggi X con la materia: assorbimento, rifrazione, riflessione e diffrazione. Si decrivono poi i principi di ottica che stanno alla base della microscopia a raggi-X: distanza focale, risoluzione e spot-size. Vengono infine descritti i differenti sistemi di focalizzazione dei raggi X e i relativi principi di focalizzazione utilizzati nella beamline ID16A nella quale si sono svolti gli esperimenti riportati e an alizzati nella seguente tesi.

Si descrivono inoltre due delle tecniche oggetto di studio nella suddetta tesi:

- la Fluorescenza a raggi–X,
- l'Imaging a contrasto di fase,
- la Tomografia a contrasto di fase.

Chapter 3

AFM Technique

3.1 Principles

Atomic force microscopy or AFM provides a 3D profile of a surface at nanoscale, by measuring forces between a sharp probe (<10 nm) and surface at very short distance (0.2-10 nm probe-sample separation). The method applies to hard and soft synthetic materials as well as biological structures (tissues, cells, biomolecules). The probe is supported on a flexible cantilever. The AFM tip "gently" touches the surface and records the small force between the probe and the surface.

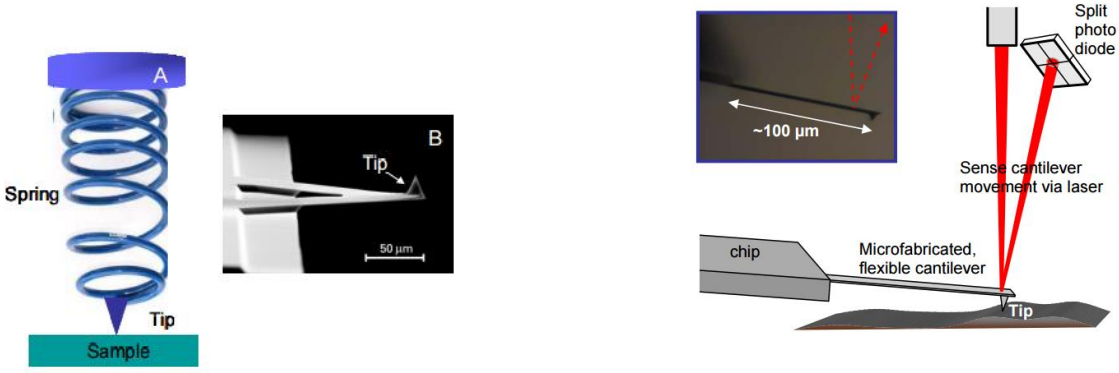

Figure 3.1: *A_ Spring depiction of cantilever B_ SEM image of triangular SPM cantilever with probe (tip).*

The probe is placed on the end of a cantilever (which one can think of as a spring). The amount of force between the probe and sample depends on the spring constant (stiffness of the cantilever), and on the distance between the probe and the sample surface.

This force can be described using Hooke's Law:

$$F = -Kx \qquad \textbf{(3.1)}$$

Where: F=Force,

K= the spring constant of cantilever (typically ~ 0.1-1 N/m),

x = cantilever deflection.

Probes are typically made from Si_3N_4, or Si. Different cantilever lengths, materials, and shapes allow for varied spring constants and resonant frequencies. Probes may be coated with other materials for additional Scanning Probe Microscopy (SPM) applications such as chemical force microscopy (CFM) and magnetic force microscopy (MFM). The motion of the probe across the surface is controlled similarly to the STM using feedback loop and piezoelectronic scanners. The primary difference in instrumentation design is how the forces between the probe and sample surface are monitored. The deflection of the probe is typically measured by a "beam bounce" method. A semiconductor diode laser is bounced off the back of the cantilever onto a position sensitive photodiode detector. This detector measures the bending of cantilever during the tip is scanned over the sample. The measured cantilever deflections are used to generate a map of the surface topography.

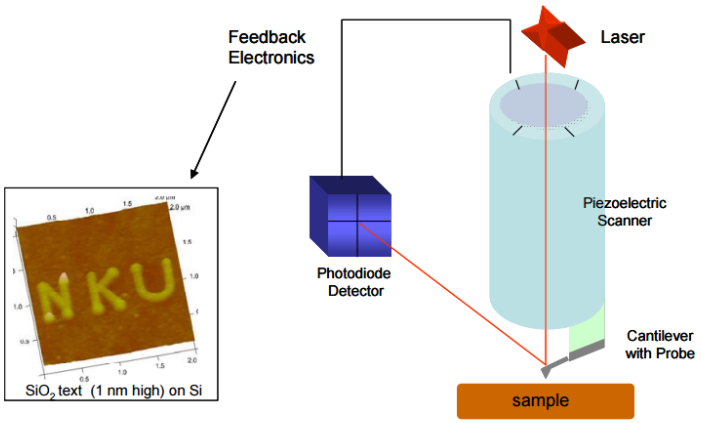

Figure 3.2: *Schematic of AFM instrument showing "beam bounce" method of detection using a laser and position sensitive photodiode detector.*

The forces that are measured are Van der Waals (VdW) interactions, because this is the dominant interaction at short probe-sample distances in the AFM. During contact with the sample, the probe predominately experiences repulsive Van der Waals forces (contact mode). This leads to the tip deflection described previously. As the tip moves further away from the surface attractive Van der Waals forces are dominant (non-contact mode). For soft materials as the biological one, the tip could damage the sample. In this case, the tapping mode is used, avoiding direct contact between the tip and the surface. In this mode, the cantilever system is excited near to its resonant frequency using a dedicated piezoelectric crystal. Due to the excitation, the cantilever oscillates with amplitude which depends on the distance between the tip and the surface. Monitoring this distance, the surface topography is obtained.

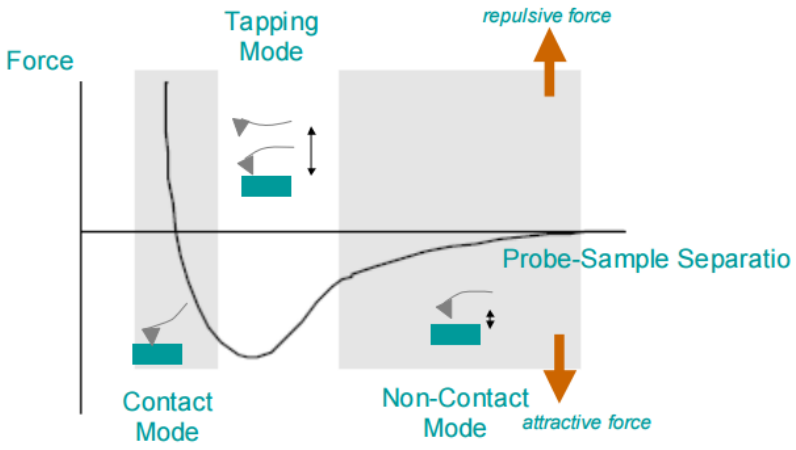

Figure 3.3: *Plot of force as a function of probe-sample separation.*

Riassunto del Capitolo 3 in Italiano

In questo capitolo è stata fatta una breve introduzione sui principi alla base della tecnica dell'Atomic Force Microscopy.

Chapter 4

BEAMLINE LAYOUT

4.1 ID16A Beamline layout

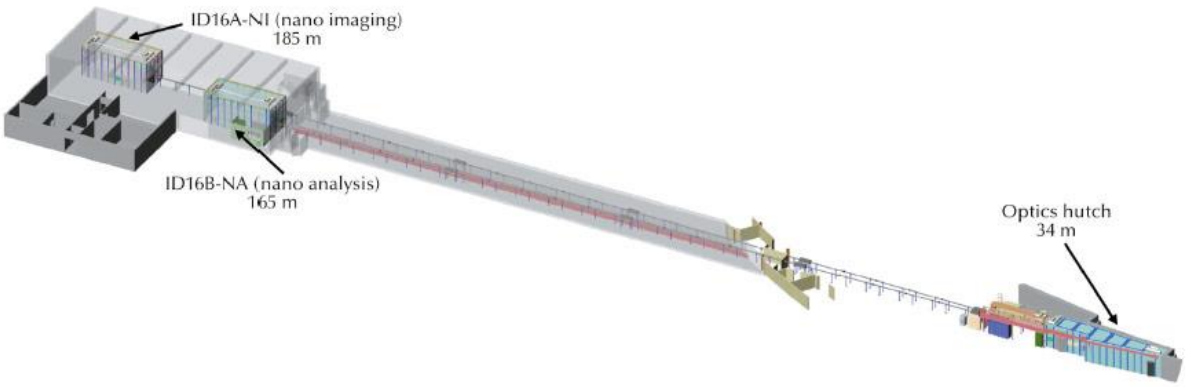

Figure 4.1: *Layout of upgrade beamlines ID16A and ID16B.*

The ID16NI beam line is part of the upgrade program of ESRF, and is one of the first to be implemented. The 185 m long beamline is equipped with a multilayer monochromator af a Kirkpatric-Baez crossed mirror system, which produces a focal spot 30x30 nm^2 (min) 400x400 μm^2 (max). Two fixed energies can be choosed: one at 17 keV, and one at 33.6 keV. In our experiment the energy at 17 keV has been used. . The sample environment is in vacuum, to avoid air scattering. Loading of the sample is completely automated. For fluorescence measurements, the sample is placed in the focal position. To help the alignment of the sample in the beam, an optical microscope in line with the beam direction is installed, which can be removed for x-ray measurements. A piezo driven translation stage allows for accurate scanning of the sample in front of the beam in the x,y directions. The fluorescence detectors are constituted by two arrays of 6 silicon drift diode detectors, placed symmetrically with respect to the sample position, and lie in a perpendicular

direction respect the incoming beam direction. This geometry minimizes both the Rayleigh and Compton scattering. The energy resolution of the solid state array detectorsis of the order of 144 eV, with the new system recently implemented. In addition to fluorescence, phase contrast (and holotomography) measurements can be carried out. In this case, the sample is displaced downstream to allow for projection geometry. The distance between the sample and the focal position can be choosed according the required magnification (see chapter II for details). The images are recorded with a FReLoN camera (a specially designed imaging camera based on a scintillator lens-coupled with CCDs) with 2048x2048 pixels and a pixel size of 1.1 μm. For measurements with frozen hydrated samples, a cryo stage has been assembled which guarantees the liquid nitrogen temperature at the sample. Figures 4.2, 4.3 and 4.4 show different details of the beam-line

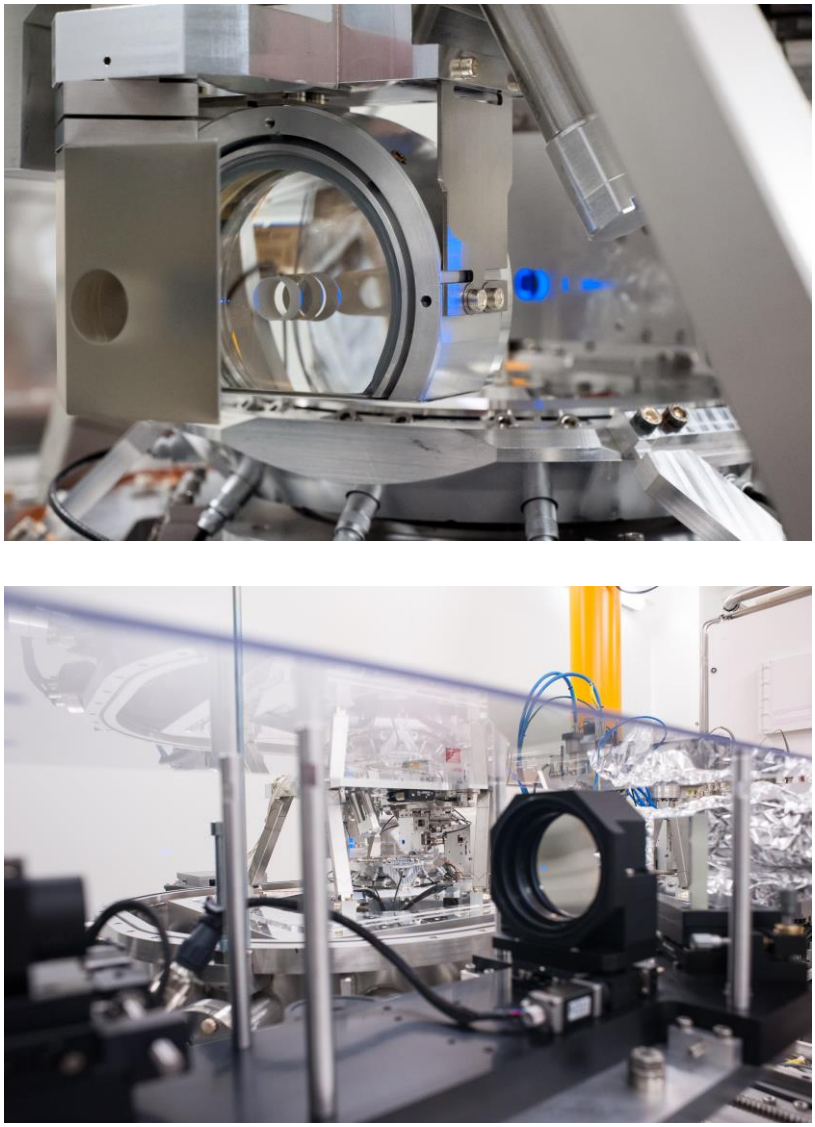

Figure 4.2: *KB mirrors and video microscope of the beamline ID16A at ESRF.*

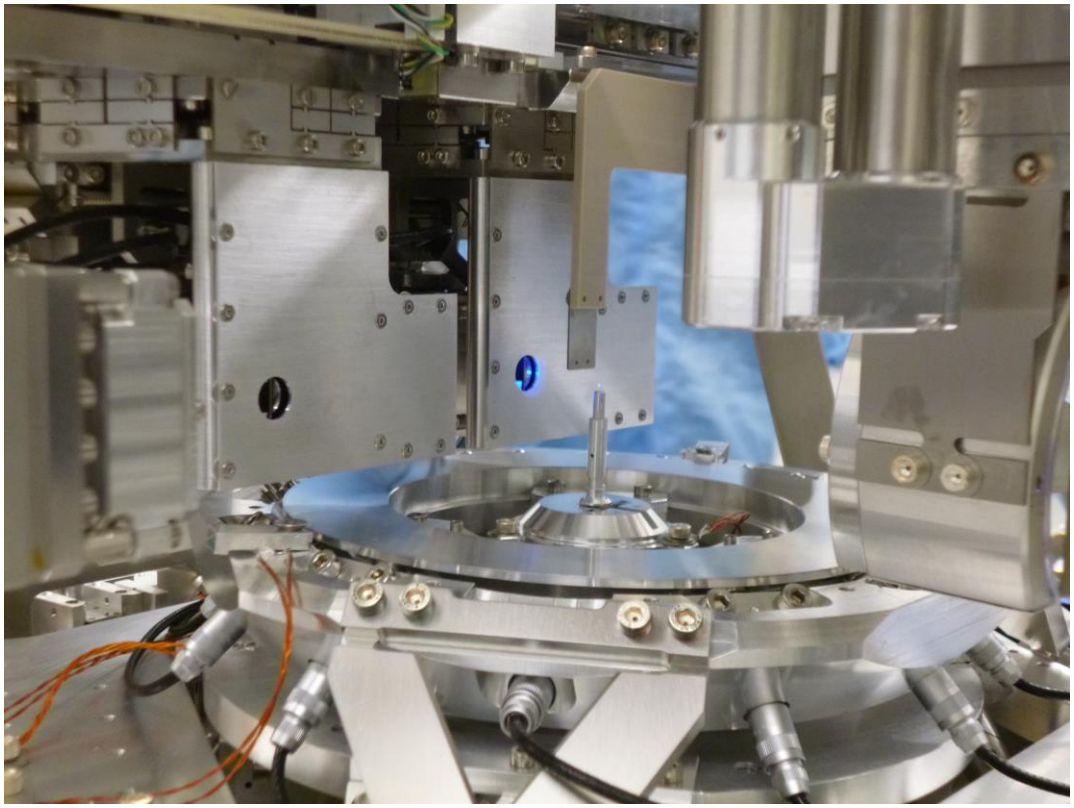

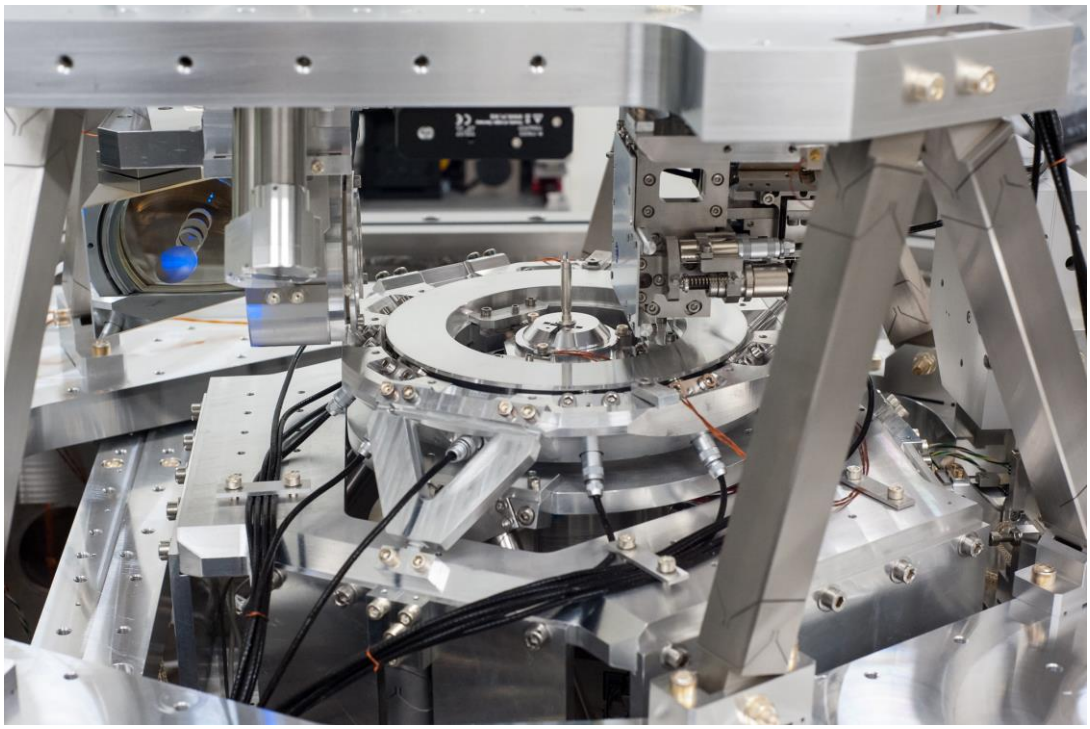

Figure 4.3: *Sample stage of the beamline ID16A at ESRF.*

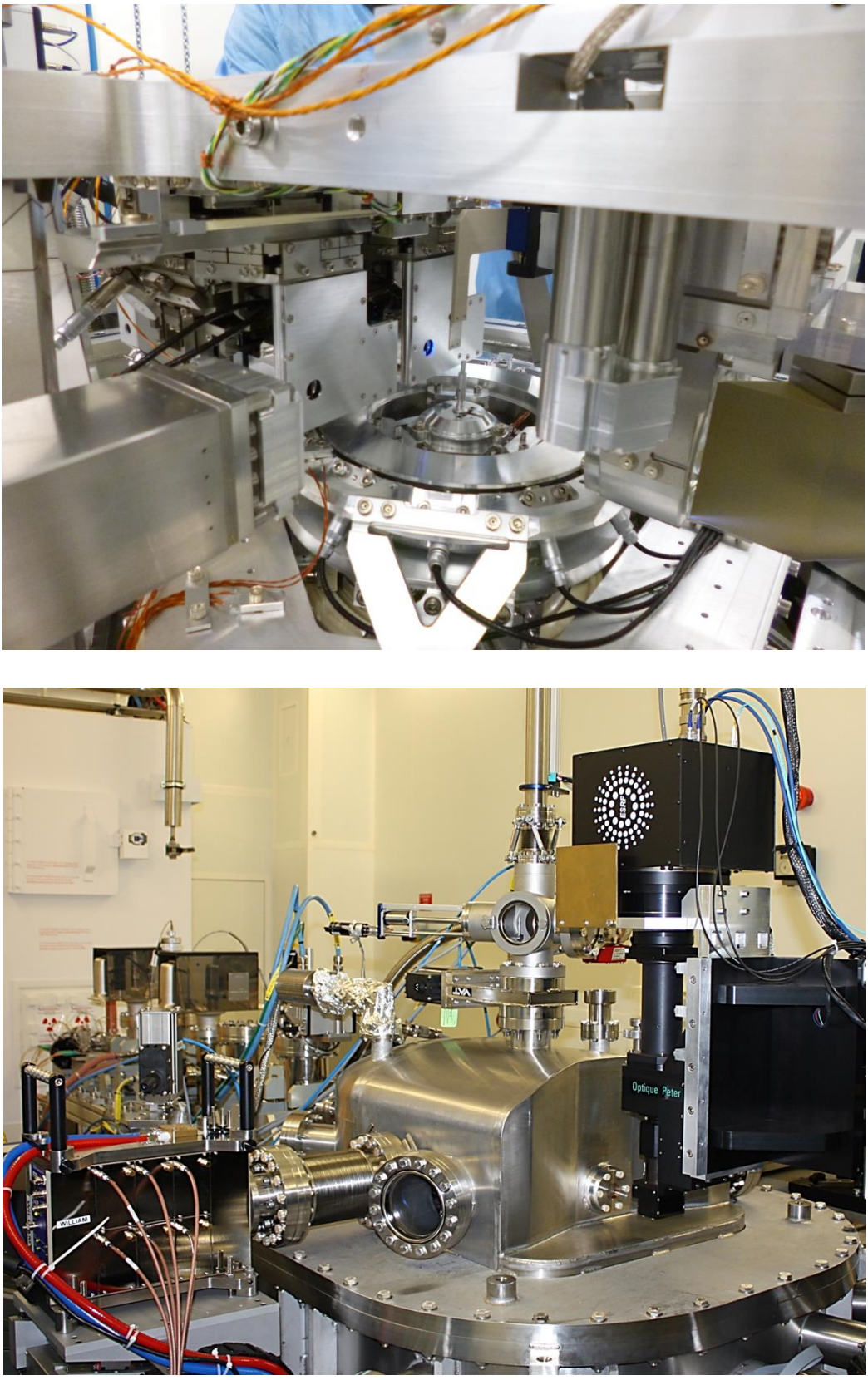

***Figure 4.4: A** Sample stage **B** Cryostage of the beamline ID16A at ESRF.*

Riassunto del Capitolo 4 in Italiano

In questo capitolo è stata fatta una breve della beamline ID16A dove si sono condotti gli esperimenti oggetto dela presente tesi.

Chapter 5
SAMPLE PREPARTION

5.1 Methods

5.1.1 Sample preparation

THP-1 cells, a myelomonocytic cell line derived from the blood of a 1-year-old boy with acute monocytic leukemia [14] (ECACC, European Collection of Cell Cultures), were maintained in RPMI 1640 medium (Euroclone, Italy) supplemented with 10% fetal calf serum and 2 mM glutamine, in an atmosphere of 95% air and 5% CO_2 as describet by Scorneaux et al., (1996) [15]. Cells, which grow spontaneously in loose suspension under these conditions, were subcultured twice a week by gentle shaking followed by pelleting and reseeding at a density of approximately 10^6 cells/ml [16] e [17].

The membranes of silicon nitride (Si_3N_4), with a window of 1×1 mm^2 and a thickness of 200 nm (Silson, UK), have been kept with 96% ethanol overnight and washed in distilled water in 24 well plates. THP-1 cells were seeded at the concentration of 10^5 cells/ml in 24 well plates, where the silicon membranes were already present, in 2 ml of RPMI medium, supplemented with 100 µM penicillin-streptomycin, 2 mM glutamine, 10% fetal calf serum, and containing 0.16 µM phorbol myristate acetate (PMA, Sigma Chemical Co.) for differentiation. The plates were incubated for 48 h, at 37° C in an atmosphere of 95% air and 5% CO_2. Differentiated THP-1 cells were washed twice with 2 ml of PBS without calcium and magnesium and stimulated with 1 µg/ml LPS from *E. coli* (InvivoGen, USA) for 48 h in an atmosphere of 95% air and 5% CO_2, at 37° C. 100 µg/ml bLf [18] were added to adherent THP-1 cells, without removing the culture medium, after 3 and 24 h from the stimulation. After 48 h of incubation, the membranes, with adherent macrophages, were then used to prepare freeze-dried cells, with two dehydration methods, and frozen hydrated cells as described in the next sections.

In both cases the cells must be initially rapidly freezed, in order to avoid formation of ice that would break the cells. In other words, the liquid water must transform to a solid glassy form. To this purpose, the cells are rapidly plunged into liquid ethane, maintained at low temperature by liquid

nitrogen. After this procedure, to obtain freeze-dried cells, the samples are put in a vacuum environment to allow for water sublimation. Instead, if frozen hydrated cells are required, the platelets are simply stored in a cryogenic environment, and the measurements are then carried out with suitable cryogenic apparatus, as that available at the ID16A.
A schematic that outlines the most common techniques is shown in Figure 5.1. They can be separated into one of two fundamental categories: either the cells are dehydrated prior to analysis, or the intracellular water is conserved and the cells are analyzed frozen-hydrated. The methods may also be organized by the mechanism that removes the culture media from a cells' surface before analysis. Either the media is removed with an isotonic rinsing solution, or the cells are freeze-fractured, removing a portion of the cell and all of the media above it, creating a pristine surface for analysis [19,20].

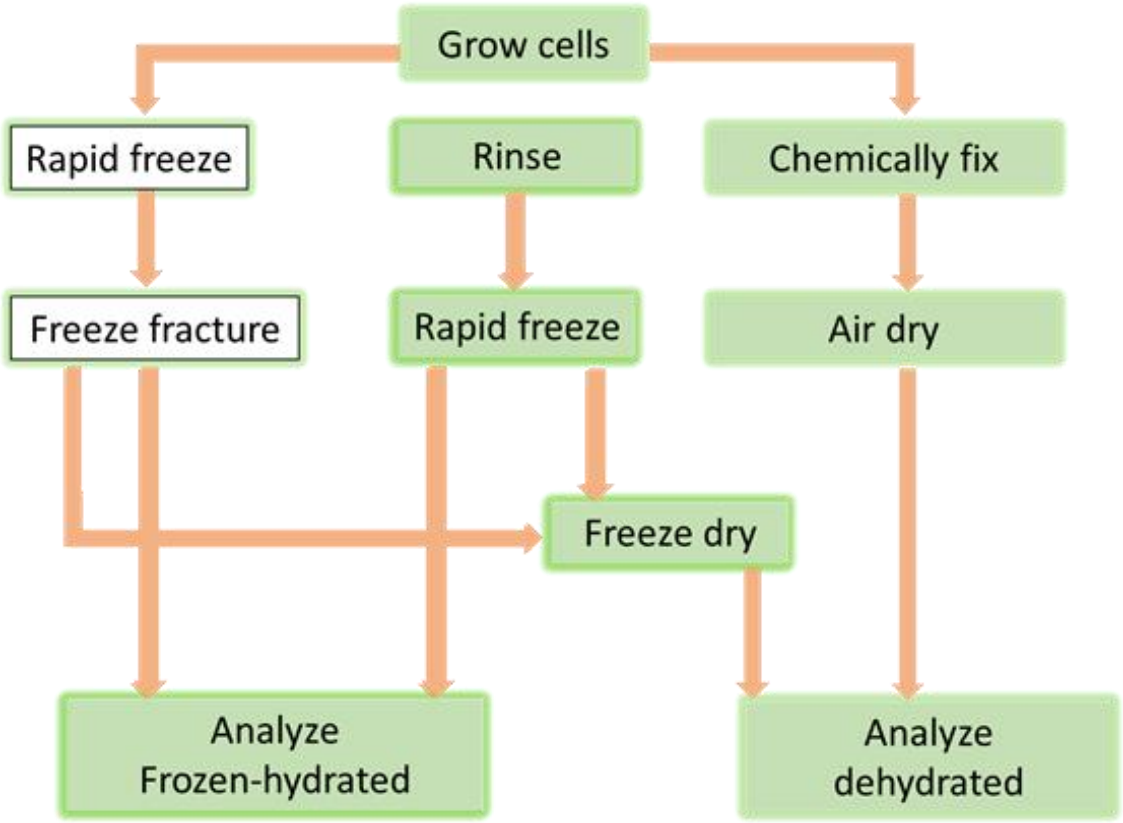

Figure 5.1: *A schematic of several of the methods used to prepare biological cells for ToF-SIMS analysis. Cells can either be analyzed following dehydration, or can be analyzed frozen-hydrated with incorporated water still present. Cells can be dried either by chemical fixation and air drying, or plunge-frozen and freeze-dried. Additionally, frozen cells can either be analyzed whole or following freeze-fracture.*

5.1.2 Chemical fixation

Cells on silicon chips were washed briefly in 100 mM ammonium acetate for three times, then fixed in methanol / acetone 1:1 at the temperature of -20° C for 5 minutes. Then the solution of methanol-acetone was removed and the cells on silicon chips was dried at room temperature inside a laminar flow hood.

5.1.3 Cryofixation

The cells on silicon membranes were washed by 100 mm ammonium acetate and then, at room temperature, criofixed quickly immersing them in liquid ethane for 5 second. Excess liquid was removed by Dehydrated at low temperature under vacuum overnight. The main features of cryofixation process are:

- protects cell structures,
- does not alter the chemical distribution of the elements,
- avoids the intrusion of exogenous factors that can lead to contamination.

Figure 5.2: *Cryo loading chamber and transfer system.*

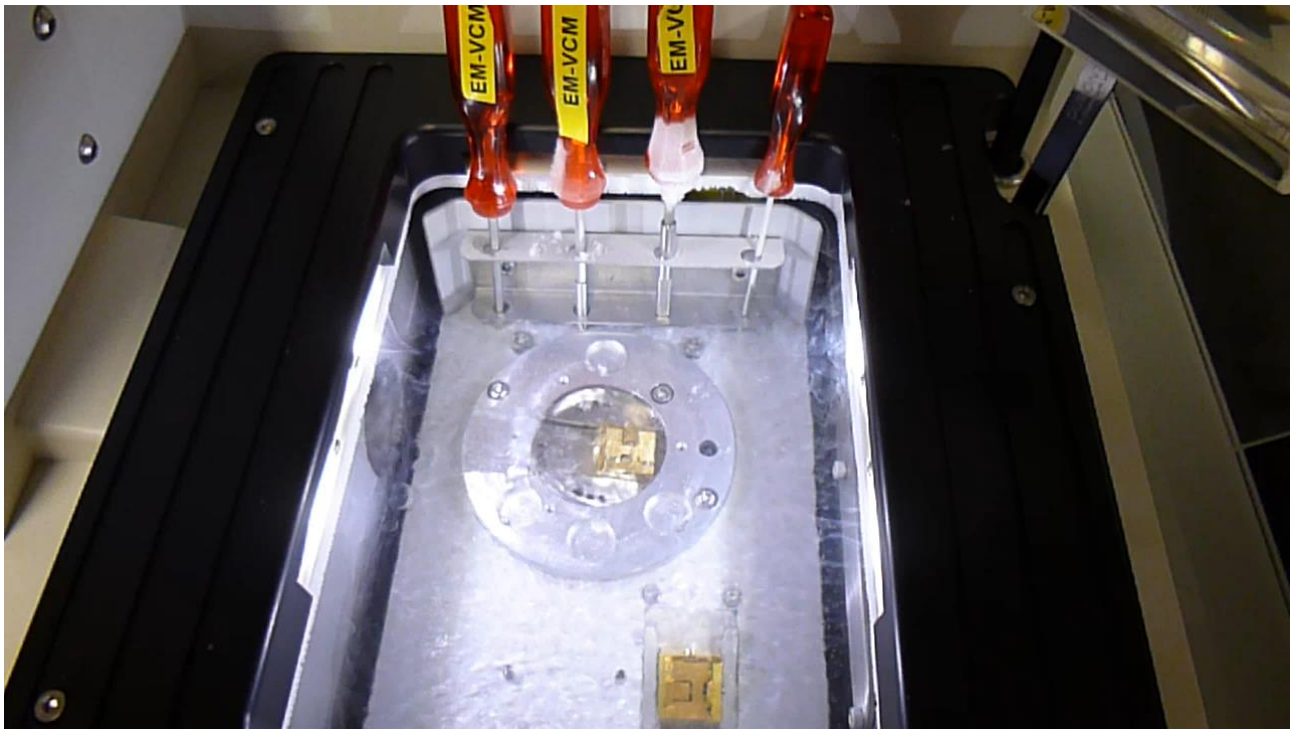

Figure 5.3: *Sample goes into the transfer shuttle.*

5.1.4 Frozen-hydrated: preparation of cells

Cells on silicon membranes were washed by 100 mm ammonium acetate at room temperature and without sterile conditions. The membranes were criofixed quickly immersing them in liquid ethane for 5 second. Prior to freezing, it is important to reduce, through blotting with Whatman paper (Sigma-Aldrich) for 1-2 second, the thickness of the liquid layer to a minimum in order to ensure the best freezing results. After cryofixation in liquid ethane, the cells will be maintained under cryogenic condition in liquid nitrogen in shipping dewar. The cells will be contained in the dewar up to the assembly in the beamlines and will be maintained under cryogenic conditions in the vacuum chamber. The sample will be transferred via a cryo transfer system at the temperature of -160°C into the chamber and onto the rotation stage.

Riassunto del Capitolo 5 in Italiano

In questo capitolo sono presentati i descritti brevemente i vari modi di fissazione delle cellule che si sono utilizzati per gli esperimenti in oggetto e si decrive la culura delle cellule utilizzate per la seguente tesi.

Chapter 6

DATA ANALYSIS AND STRATEGY FOR ELEMENT QUANTIFICATION

6.1 Combination of different techniques for quantitative evaluation

The result of the x-ray meaurements is a map showing the spatial variations of the x-ray fluorescence intensity. However, the thickness and the density of the cell are not uniform; therefore if quantitative result in concentration are the object of the research, the fluorescence measurements must be complemented by some technique which gives information about the cell topography, i.e. the volume distribution. The first choice is the Atomic Force Microscopy that, as explained in chapter 4, gives directly the thickness of the object, taking as reference the platelet where the cell is grown. The volume of the sample excited by the incoming beam, for each pixel of the scan in the fluorescence measurements, is therefore simply the product of the thickness for every pixel location, by the size of the focused beam. Therefore, the concentration can be simply found dividing the fluorescence intensity by the volume. The procedure will be better explained in the course of this chapter see also *Annex 1*. Another possibility for quantitative measurements is to use x-ray absorption or phase contrast measurements: In both case what is obtained is a quantity proportional to the product of the thickness by the electronic density.Normalization of the fluorescence intensity by this quantity gives not the concentration, but the mass fraction, which can be different of the concentration. However, in the case of AFM the measurements must be carried out off-line, therefore in conditions in principle different from those pertaining to the fluorescence measurements. Instead, X-ray absorption or phase contrast measurements cn be carried out simultaneously, or at least with the same apparatus, as the X-ray fluorescence. Furthermore, AFM can only be carried out on freeze-dried cells. In the case of frozen hydrated cells, which must be maintained at cryogenic temperature, AFM cannot be used, and only x-ray techniques must be adopted. To use absorption or phase contrast depends essentially on the energy of the x-ray beam.

Chapter VI – Data Analysis and strategy for element quantification

For soft x-rays, up to 1-2 keV, the absorption contrast from biological structure is still enough, but for higher energies the contrast in absorption is too weak and phase contrast is necessary, as in this work. Another distinction must be made regarding the element that one wants to study. If the element is light, then the fluorescence line has a low energy, and therefore is strongly absorbed by the sample itself, this is the effect of self-absorption. In this case, a correction must be made to the measured fluorescence intensity. To make this correction the density must be known. If both the AFM and absorption of phase imaging have been done, the density can be obtained by normalizing the results of the x-ray imaging measurement (which give a quantity proportional to the product of the thickness by the density), by the thickness obtained with the AFM [7]. In our work, this procedure is not necessary because the fluorescence line of Fe is practically not absorbed by the cell, which has a thickness of the order of 1 micrometer. To overcome the limitations of both AFM and 2-D imaging, X-ray nanotomography can be used, as demonstrated in this work. With nanotomography, in our case holotomography because the contrast is given by phase variations, both the thickness and the density can be known independently. Therefore, with this powerful technique both concentration and mass fraction maps can be obtained, giving a complete morphological and compositional quantitative information at the nanoscale. The last technique that can be considered for quantitative measurements is the fluorescence tomography, where fluorescence scan are made for a number of projections. In this case, the concentration and the mass fraction are directly obtained, without the need of normalization of fluorescence intensity by some other quantity. This last technique is obviously the best one in principle, but requires very long acquisition time, and for sensitive material, as the biological one, can be hardly adopted because of the radiation damage. The table below summarizes the information that can be obtained with the combined use of the different technques, distinguishing between freeze-dried and frozen hydrated cells. Inside these two categories, we distinguish also between fluorescence by light elements, which requires correction of the outcoming fluorescence intensity because of the self-absorption effect, and fluorescence by heavy elements where the self absorption is not relevant. Summarizing, the techniques we took into consideration are:

i) Scanning X-ray fluorescence microscopy (XRFM) in two dimensions;

ii) X-ray imaging in one projection (two-dimensional), either in absorption and in phase contrast;

iii) X-ray tomography either in absorption and in phase contrast;

iv) Fluorescence tomography.

	Freeze dried						Frozen hydrated					
	Light elements (need for self-abs. corr)			Heavy elements (no self-abs. corr)			Light and heavy		Light el.		Heavy el.	
	AFM	Fluo (2D)	X-ray imaging (2D)	AFM	Fluo (2D)	X-ray imaging (2D)	Fluo (2D)	X-ray Tomo (3D)	Fluo tomo (3D)	X-ray Tomo (3D)	Fluo tomo (3D)	X-ray Tomo (3D)
Density	X		X	X		X		X		X		X
Weight Fraction.	X	X	X		X	X	X	X	X	X	X	X
Conc.	X	X	X	X	X		X	X	X	X	X	

Table 6.1: *X-ray techniques that can be used for quantitative mapping of relevant morphological and compositional quantites.*

In the following, we describe the experimental details and the data analysis procedures for fluorescence, phase contrast imaging, AFM and nanotomography.

6.1.1 Detection and processing of the X-ray fluorescence signal

The fluorescence measurements have been carried out scanning the sample in front of the focused beam with Focus size (H x V) 23 nm x 37 nm. The energy of the incoming photon beam was 17.05 keV. The total scanning area was between 10 and 20 micrometer, depending on the cell size, and taking into account that it is important to leave some free space around the cell to individuate clearly the borders of the cell. The pixel size was fixed at 100 nm, as a good trade-off between spatial resolution and the total acquisition time. For each pixel the acquisition time was of the order of few seconds. To detect the fluorescence signal, energy dispersive detectors are used. They can be placed at different angles with respect to the beam (depending on the beam line layout) but ideally at 90º to fully utilize the advantage of linear polarization. This is the case for the present

work (see chapter IV on the beamline layout). The energy dispersive detectors record at one time the spectra of all the elements in the specimen.

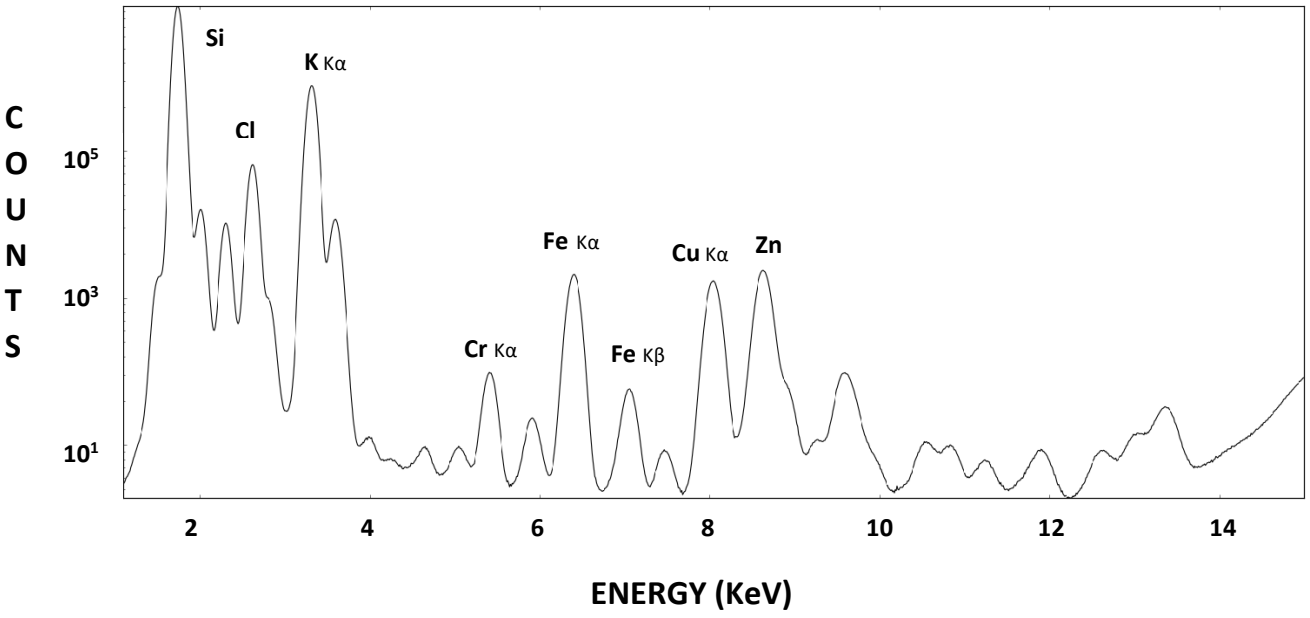

Figure 6.1: *Typical fluorescence spectrum of our samples. Incident photon energy: 17.05 keV*

To analyse the fluorescence data, we used PyMCA, a free available software, which was developed at the European Synchrotron Radiation Facility [11]. The program allows interactive as well as batch processing of large data sets and is well suited for X-ray fluorescence microscopy. The quantification of the fluorescence intensity is based on a fitting procedure of the recorded fluorescence spectra. Spectrum evaluation is made by nonlinear least-squares fitting of a mathematical model to the spectral data in order to deal with background and resolve peak overlaps.

$$\chi^2 = \frac{1}{n-m} \sum_i \frac{[y_i - y_{fit}(i)]^2}{y_i} \qquad \textbf{(6.1)}$$

Where y is the content of channel i, y_{fit} is the calculated value of fitting function in this channel, n is the number of channels and m is the number of parameters in the fitting function. As the background in XRF spectrum is the result of many processes, its evaluation is not straightforward. However, there are some established strategies how to deal with it. It can be estimated before and thus subtracted from the data before fitting. After this procedure, the area under each peak is obtained, giving the number of counts for that specific fluorescence line. A map giving the spatial distribution of the fluorescence intensity can be obtained (see Figure 6.2)

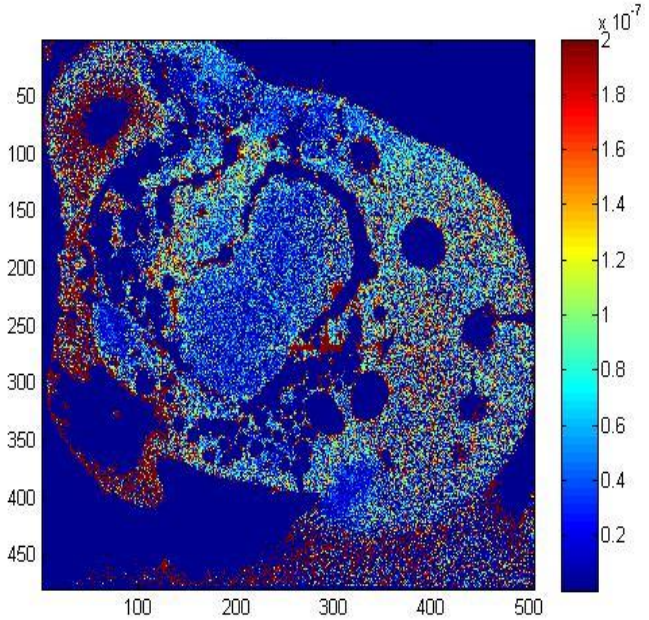

Figure 6.2: *Iron Fluorescence intensity map of our samples.*

To obtain quantitative information from the measure of the fluorescence radiation, we used the fundamental parameter method [7] based on the relation:

$$dR_i = dm_i \times dV \times Y\left(E_{0,i}\right) \times I_0 \exp\left(-\chi \rho z\right) \qquad \textbf{(6.2)}$$

Where:

dR_i is the contribution to the total counts for that specific X-ray fluorescence emission line of a particular elemental species (e.g. Fe), given by the sample mass $dm_i = w_i \, \rho \, dV$ contained in the infinitesimal volume $dV=S \, dz_i$, at the depth z. w_i is the mass fraction, ρ the density and dV the volume illuminated by the incident beam of energy E_0 as show in figure 6.3.

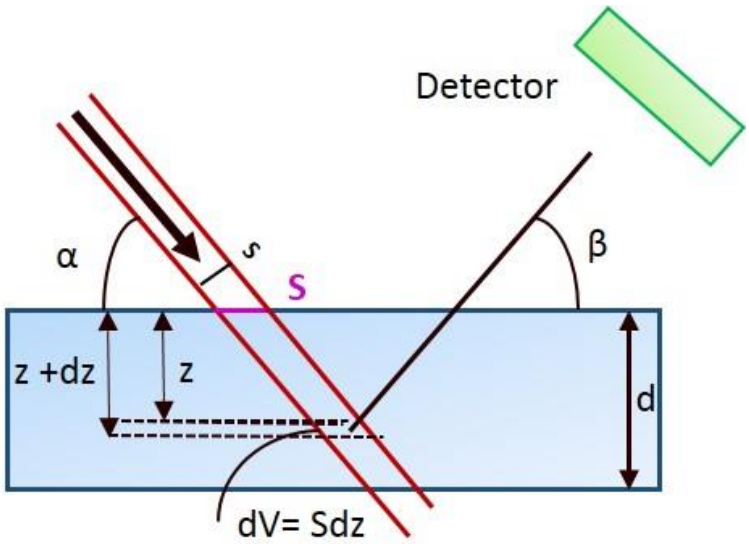

Figure 6.3: *Irradiation geometry during μ-XRFexperiments: α= angle of incidence of the primary beam, β= (average) take-off angle of the fluorescent radiation, S= beam footprint on sample surface.*

$$Y(E_{0,i}) = \varepsilon_i(\Omega/4\pi)\omega_i p_i \tau(E_{0,i}) \quad \textbf{(6.3)}$$

where ε_i is the detector efficiency, (Ω) the solid angle seen by the detector, ω_i the fluorescence yield, p_i the transition probability and $\tau(E_{0,i})$ the photoelectric cross section at $E_{0,i}$ where the index i refers to a particular elemental species.

I_0 is the incident intensity and

$$\chi = [\mu_m(E_0)cosec(\alpha) + \mu_m(E_i)cosec(\beta)] \quad \textbf{(6.4)}$$

represents the total self-absorption of primary and fluorescent radiation in the sample, where E_i is the energy of the specific fluorescence radiation of element i. $\mu_m(E_0)$ is the sample mass absorption coefficient at the energy E_0 of the incident beam, α is the incident angle, $\mu_m(E_i)$ is the mass absorption coefficient at the energy E_i of the specific fluorescence line, and β is the exit angle of the fluorescence radiation as seen by the detector. In our case, for the Fe ka fluorescence line at 6.4 keV the self absorption is negligible, and the exponential factor in eq. 6.2 can be approximatyed to 1. The mass fraction $(w_p)_i$ for each pixel p for each element i can be calculated by the following expression derived from equation (6.3):

$$(w_p)_i = \frac{(R_p)_i}{\rho_p \cdot V_p \times Y(E_{0,i}) \times F_p} \quad \textbf{(6.5)}$$

where V_p is the volume of the pixel p, expressed in cm^3, and F_p is the correction factor for the self absorption of both the incident beam and the fluorescence radiation. Analogously, the concentration $(M_p)_i$ in the single pixel p, expressed in molarity, is derived by the following expression:

$$(M_p)_i = \frac{(m_p)_i}{A_i \cdot V_p} \times 10^3 = \frac{(w_p)_i \cdot \rho_p \cdot V_p}{A_i \cdot V_p} \times 10^3 = \frac{(R_p)_i}{A_i \cdot V_p \times Y(E_{0,i}) \times F_p} \times 10^3 \quad \textbf{(6.6)}$$

where m_i is the mass expressed in grams and A_i is the atomic weight of the i^{th} element. It is evident that equation (6.6) is a modified version of the fundamental parameter equation (6.5) simplified for the density ρ. As a consequence, concentrations can be directly calculated if the volume of the sample illuminated by the beam in each pixel is known. However, in the equations (6.3), (6.5) and (6.6), the factor Y is not known, because it contains also the efficiency and the solid angle seen by the detectors. It is difficult to know exactly these parameters that can be different for the different detectors constituting the array, therefore we obtained these values using a standard. Figure 6.4 shows the fluorescence spectrum of the reference sample.

	Mass	Emission Lines (eV)		
	(ng/mm²)	Kα	Lα	Mα
Pb	7.7±1.3	85335	10541	2346
La	9.0±1.9	33298	4649	833
Pd	1.9±0.8	21123	2838	
Mo	0.9±0.1	17444	2293	
Cu	2.4±0.5	8040	930	
Fe	4.0±0.4	6401	747	
Ca	11.4±5.5	3691	341	
Si	Substrate	1740		

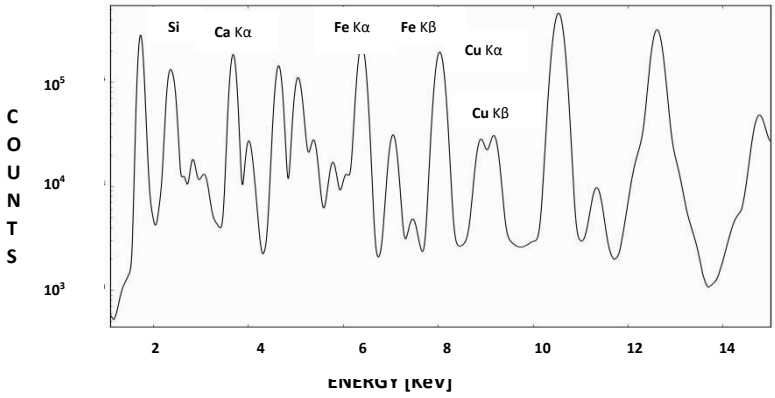

Figure6.4: *Energy spectrum of the 7-element reference sample RF4-200-S1749 (similar to the RF7) measured at 17 keV excitation. The energy range from ~2 keV to ~17 keV is covered with peaks of comparable intensity.*

The standard has been measured in the same conditions as the sample, and the Fe peak has been analysed in the same way as the sample. Because the concentration of iron in the standard is known,

it is possible to extract from the eq. 6.6 applied to the standard, the value of the factor Y, that can then be used to calculate the Fe concentration in the sample.

6.1.2 Atomic Force Microscopy measurements

The AFM measurements were carried out at the Institute for Photonics and nanotechology of national Research Council in Rome (IFN-CNR), using a Digital Instruments D3100 AFM equipped with a Nanoscope IIIa controller. The Tapping Mode was used in order to avoid damage of the cells, at a resonance frequency of about 260 kHz using monolithic silicon tips with an apex curvature radius in the 5÷10 nm range and a typical force constant of ~40 N m-1. Typically, the scan size was of the order of 50 μm x 50 μmm with 512x512 pixels. The scanning parameters (including scan size and angle, tip speed, feedback setpoint and gains) were carefully selected in order to prevent artefacts and/or cell damage. Images were collected without filtering or flattening. Quantitative thickness maps were obtained with a careful data analysis procedure. AFM height data were corrected for the substrate level offset and tilt: to this purpose, the scan size was much larger than the cell dimension. Typically, we had about 10-micron-wide substrate surface surrounding the cell in the image. The cell thickness at each pixel was then estimated as the height measured with respect to the substrate level.

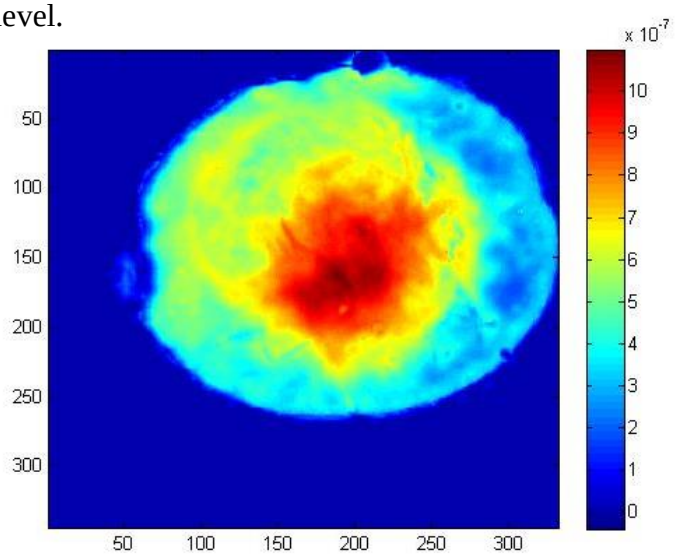

Figure 6.5: *Atomic Force Microscopy map [μm] of our samples, corresponding to XRF figure 6.1.*

6.1.3 Phase contrast imaging measurements

The phase contrast imaging was obtained in a magnifying geometry translating the sample from the focus position of the mirrors, to a distance z_1. The imaging detector, (see chapter 4) was at a distance z_2 from the sample, then we had a magnification factor M and a defocusing distance D given by:

$$M = \frac{z_1 + z_2}{z_1} \quad \textbf{(6.7)}$$

$$D = \frac{z_1 z_2}{z_1 + z_2} \quad \textbf{(6.8)}$$

As explained in chapter 2, for phase retrieval it is convenient to have measurements at different defocusing distances, because for each distance a given spatial frequency have maximum phase contrast. The sample was then put at different distances (29 mm, 30 mm, 34 mm and 44 mm) downstream of the X-ray focus resulting in different magnification and defocusing distances. To correct for inhomogeneities in the incoming beam and to subtract the electronic noise, we acquired also darkfields (i.e. acquisitions without beam), and flat field images, i.e. acquisitions with the beam but without the sample. Furthermore, to allow for averaging, we acquired 17 images, 10 reference beams and 20 darkfields for each of the four distance. We take average of the 17 images, then we subtracted the average of the dark field and we normalized with the average of the flat field image (to which we subtracted the average of the dark field). After these procedures, we obtain four images, one for each distance, as we can see in the Figures 6.6-6.7-6.8-6.9.

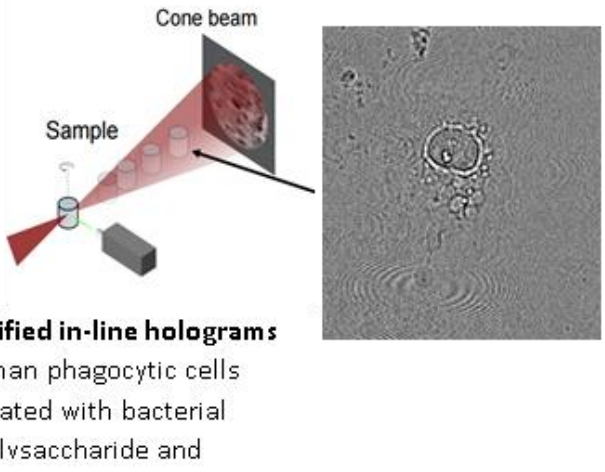

Figure 6.6: *Average of the images at the fourth distance D=44 mm.*

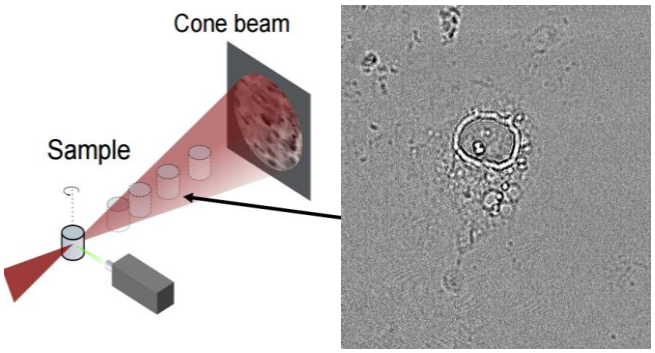

Figure 6.7: *Average of the images at the third distance D=34 mm.*

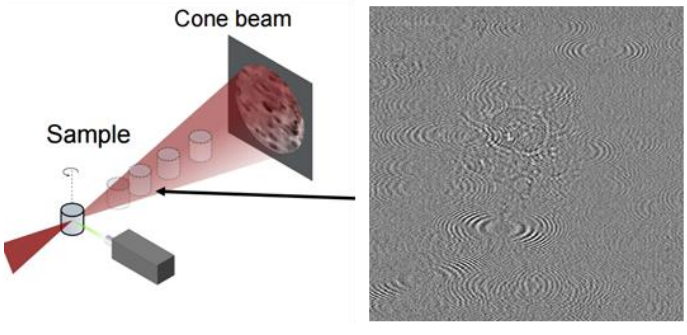

Figure 6.8: *Average of the images at the second distance D=30 mm.*

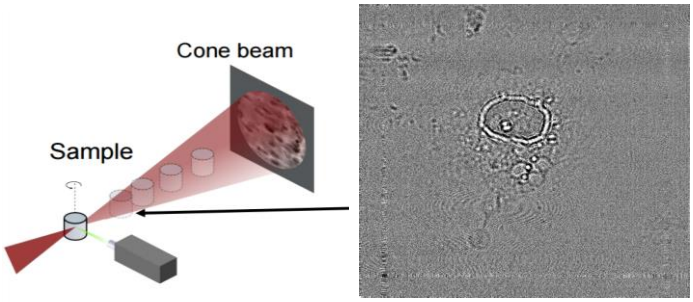

Figure 6.9: *Average of the images at the first distance D=29 mm.*

To retrieve the phase, we carried on the procedure described in chapter 2 (eq. 2.26 and .2.27), considering the four images, each at its own magnification. The final result is the phase map $\phi(x,y)$ displayed in Fig. 6.10.

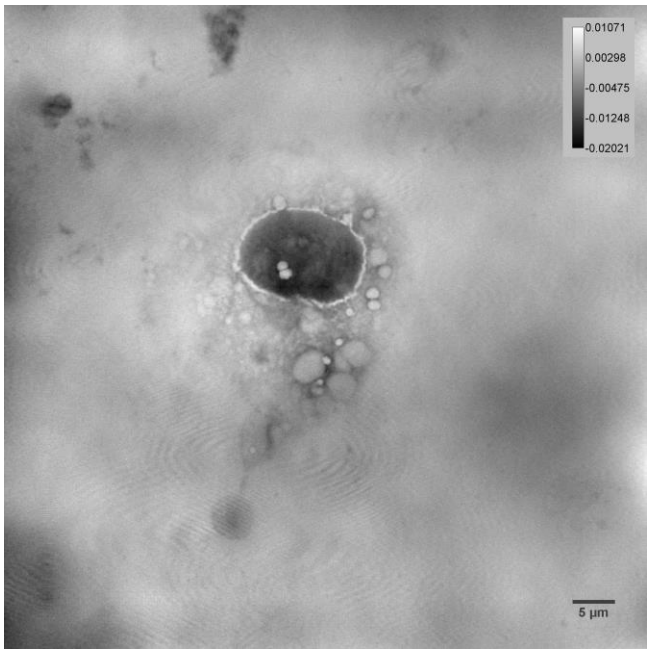

Figure 6.10: *Phase-map of human phagocytic cells stimulated with bacterial lipopolysaccharide and lactoferrin [rad].*

The phase ϕ(x,y) can be described (see chapter II) as:

$$\phi(x,y) = -\frac{2\pi}{\lambda}\int \delta(x,y,z)dz \qquad \textbf{(6.9)}$$

where z is the propagation direction and λ the wavelength. Far from the absorption edges and considering the fact considering the fundamental elements, essentially (C, N, O) in biological systems, we can calculate the real part of the refractive index as:

$$\delta = \lambda^2 (N_0 r_0) \sum \frac{Z_i}{A_i} \qquad \textbf{(6.10)}$$

δ is proportional to the mean density, therefore we can put:

$$\phi = \alpha\langle\rho\rangle T \qquad \textbf{(6.11)}$$

where T is the sample thickness and α is:

$$\alpha = \frac{2\pi}{\lambda}\lambda^2 (N_0 r_0) \sum \frac{Z_i}{A_i} \qquad \textbf{(6.12)}$$

Where: λ = wavelength =7,27677XE^{-9}cm for an Energy of 17000 eV

N_0 = Avogadro number (6,022X10^{-23});

A= Atomic mass of element;

ρ_m = density;

r_0 = classical radius of electron ($2{,}8X10^{-13}$ cm);

Z= atomic number of element;

Carbon (C)	Nitrogen (N)	Oxygen (O)
W_C=0.62	W_N=0.16	W_N=017
A_C=12.01	A_N=14.01	A_N=16
Z_C=6	Z_N=7	Z_N=8

Table 6.2: *Fundamental elements in biological systems.*

In other terms, the result of the phase contrast measurement is not the thickness, as in the AFM, but a quantity proportional to ρT. This implies that normalizing with the resulting phase i.e. the projected density; we cannot obtain the true element concentration, but the mass fraction. In the figures 6.11 and 6.12 we show the Fe fluorescence intensity normalized with the volume measured with the AFM, thus obtaining the Fe concentration, (eq. 6.6), compared with the same Fe fluorescence intensity normalized with the phase, which gives the mass fraction (eq. 6.5).

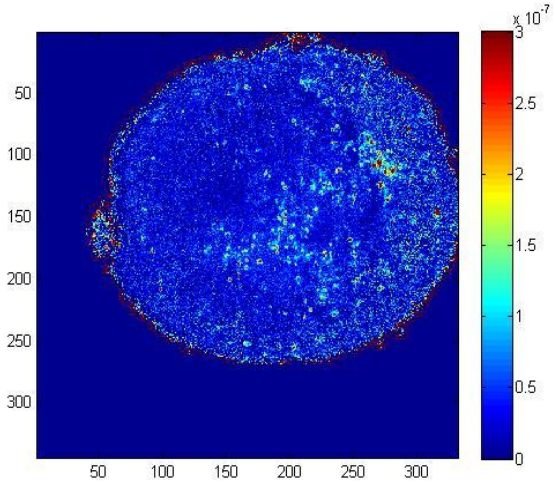

Figure 6.11: *Iron Concentration Map of our samples [nM]. This conversion in nM is an approximation because the concentration expressed in moles is a quantitative measure of the solute present in the solution in this case the sample is freeze-dried and so it is an approximation but useful as reference quantity in the biological field.*

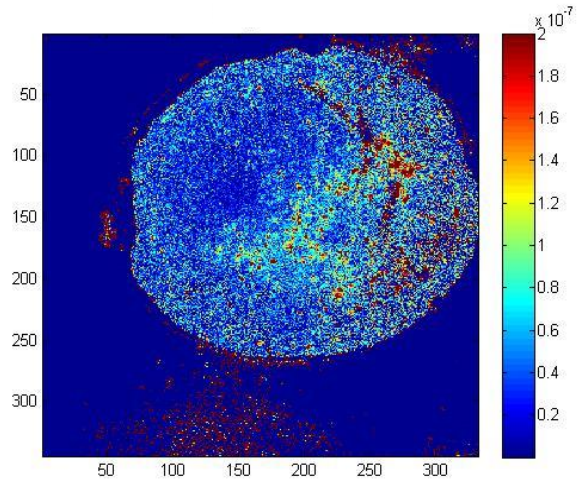

Figure 6.12: *Iron Mass fraction Map of our samples.*

From eq. (6.11), it is clear that combining the phase measurement $\varphi = \alpha\langle\rho\rangle T$ with the AFM which gives T, it is possible to derive the density of the sample, if α is known, as in our case. Fig. 6.13 shows the density of the sample, obtained normalizing the phase result with the AFM. This gives additional information about the cell morphology, and can be relevant if correction for self-absorption in the fluorescence measurements must be carried out.

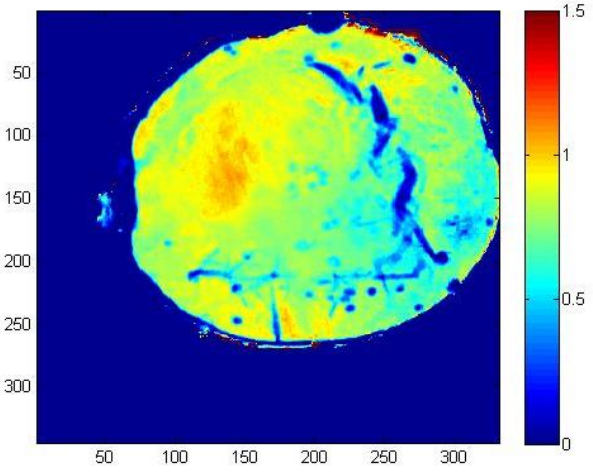

Figure 6.13: *Density Map of our samples [g/cm^3].*

6.1.4 Magnified Holotomography

Figure 6.14 illustrates schematically the procedure for holo-tomographic reconstruction.

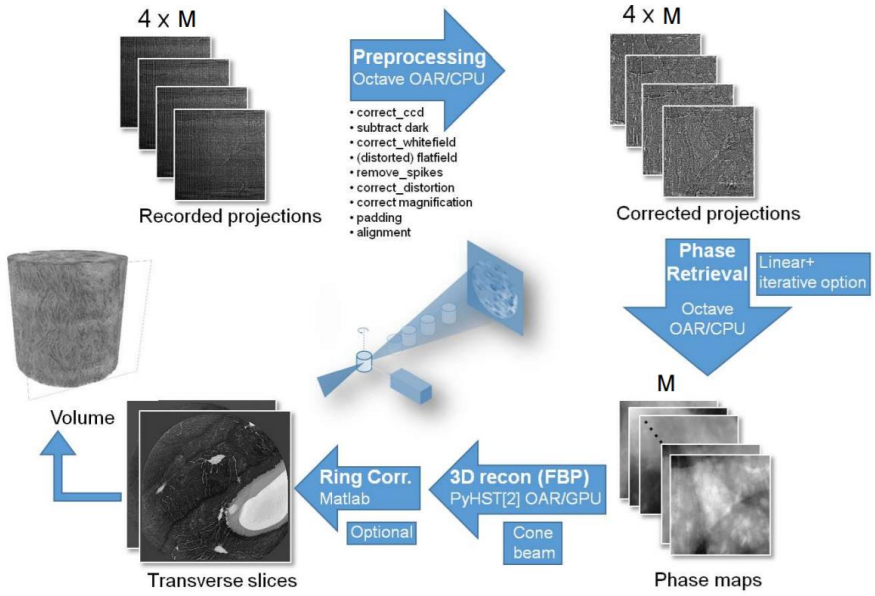

Figure 6.14: *Scheme of the analysis followed to obtain magnified Holotomography.*

As said before, holotomography consists in acquiring phase contrast images for different rotation angles of the beam with respect to the incident beam. For each angle, images are acquired at four different distances, in order to allow for accurate phase retrieval. The four distances were the same as in the phase contrast imaging. For each distance 602 images were acquired, at a distance of 0.5 degrees eachUnfortunately, due to the sample geometry (cells grown on platelets), it was not possible to acquire full angular range of 360 degrees. This can introduce in the tomography some artefacts. An essential point is the alignment of the sample with respect to the rotation axis. This must be very close to the sample surface, but external to the sample, in order not to introduce artifacts to correct for electronic noise and inhomogeneities in the beam, both dark field images without beam and reference images without sample were acquired, as in phase contrast imaging. To analyze the phase contrast tomography data we follow a procedure similar to that described in par. 4.2 for analysis of the magnified phase contrast imaging. We make a preprocessing of recorded projections in order to:

- Normalize with the reference images to correct the whitefield,
- to correct the distortion,
- to substract the darkfield,
- to correct magnification,

- to make the alignment of the images taken at the four distances.

Then we applied the phase retrieval with a linear iterative method, obtaining the phase map for each angle, as described in par. 6.1.3. Then the procedure for tomographic reconstruction, described in par. 2.7, is carried out to finally obtain the 3D reconstruction volume of the cell electronic density. Figure 6.15 shows the reconstructed electronic density.

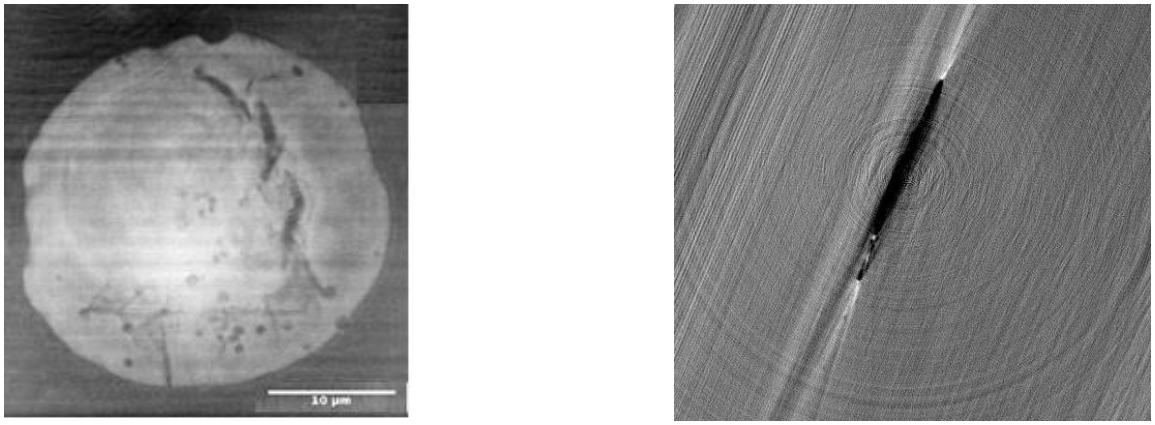

Figure 6.15: *Projected Density Map from Nanotomography [A.U.].*

Some rings appear, indicating a non perfect alignment of the sample with respect to the center of rotation. These rings can be eliminated applying filtering to the image. Figure 6.16 shows the image after this procedure.

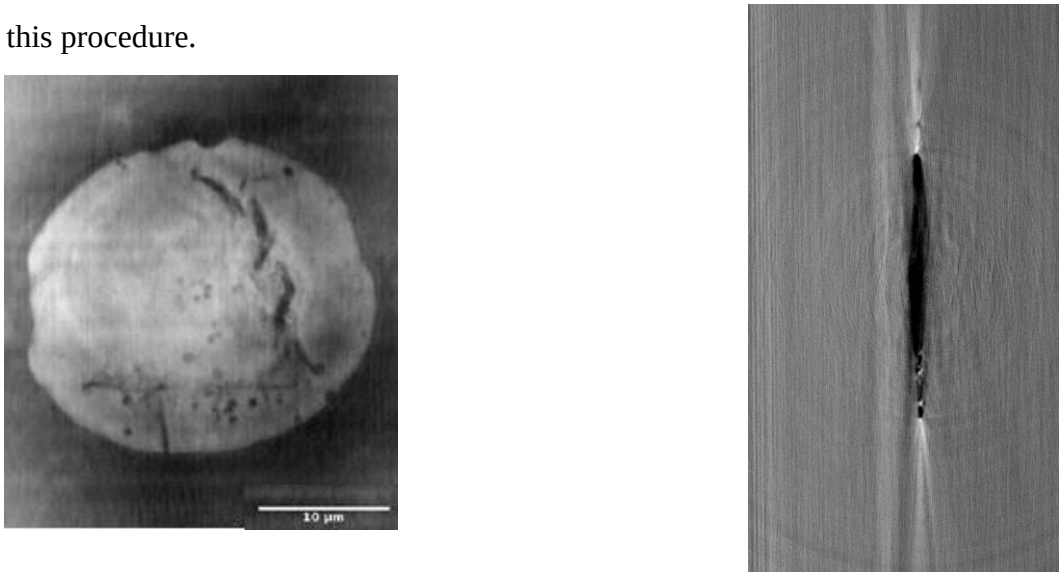

Figure 6.16: *Projected Density Map from Nanotomography after ring correction [A.U.].*

The main scope to make holo-nanotomography is to acquire morphological information and to exploit this information to obtain element concentration, without using AFM. The first step is to determine the cell thickness from the tomographic reconstructios. To this purpose, we have not used directly the reconstructed tomographic image in terms of representation of the local electron

density; instead, we have used it to obtain a morphological segmentation of the cell, and then we projected along the thinnest direction of this 3D mask. We have a 3D matrix with ones inside the cell and zeros outside the cell. The thickness map (see Figure 6.17) is then obtained by summing along the short axis and converting the pixel size into micrometers.

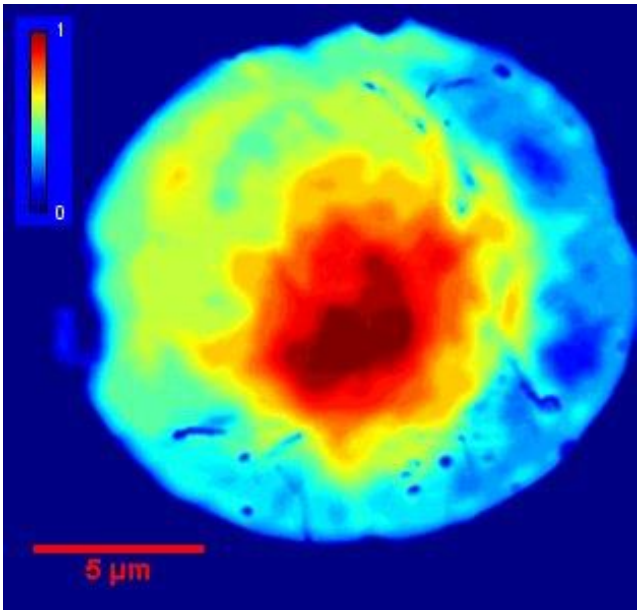

Figure 6.17: *Thickness map from nanotomography [µm]*

After the cell thickness have been determined, we registered it with respect to the x-ray microfluorescence map, and we normalized pixel by pixel the fluorescence intensity with the pixel volume, obtained as the product of the thickness by the pixel surface. In this way, the iron concentration map is determined (see Figure 6.18).

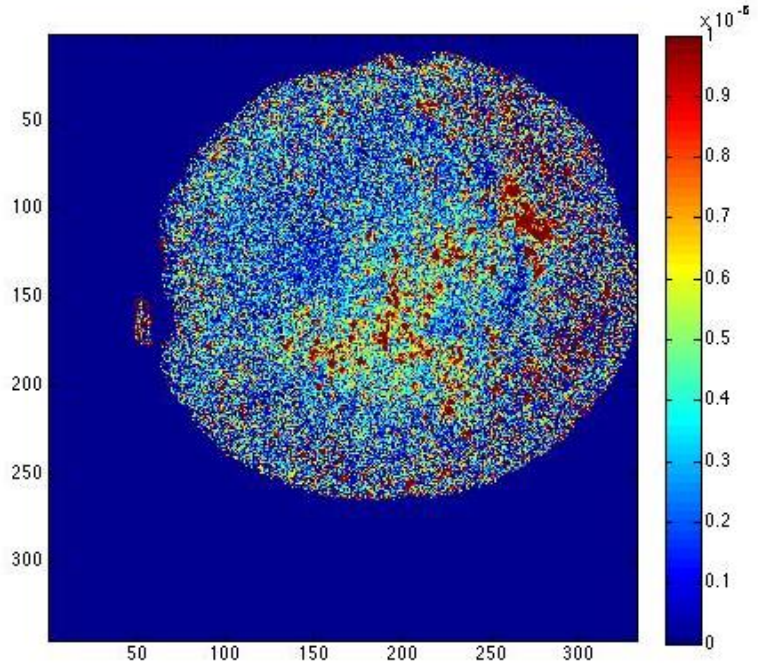

Figure 6.18: *Iron Concentrations maps from Nanotomography [nM]. This conversion in nM is an approximation because the concentration expressed in moles is a quantitative measure of the solute present in the solution in this case the sample is freeze-dried and so it is an approximation but useful as reference quantity in the biological field.*

This is the first time, to our knowledge, that quantitative concentration maps have been obtained by the combination of x-ray flurescence microscopy with quantitative holo-nanotomography. The relevance of this approach is also due to the fact that both these techniques are based on synchrotron radiation, and can be carried out on the same beamline, as in this case, therefore under the same conditions for the cells. In particular, the technique can also be applied to frozen hydrated cells, maintained at cryogenic temperature, therefore in a status as close as possible to the living cells.

Riassunto del Capitolo 6 in Italiano

In questo capitolo sono presentati e descritti tutti i criteri di analisi utilizzati per analizzare le mappe di Phase contrast imaging 2D e 3D, e di fluorescenza in modo da ottenere poi mappe di mass fraction, concentrazione, e di densità.

Chapter 7

DESCRIPTION OF EXPERIMENT ON FREEZE-DRIED CELLS AND RESULTS

This chapter is based on the article published in the Journal of Physics, Conference Series:

Gramaccioni C., Procopio A., Farruggia G., Malucelli E., Iotti S., Notargiacomo A., Fratini M., Yang Y., Pacureanu A., Cloetens P., Bohic S., Massimi L., Cutone A., Valenti P., Rosa L., Berlutti F. and Lagomarsino S. "**Combined use of X-ray fluorescence microscopy, phase contrast imaging for high resolution quantitative iron mapping in inflamed cells.**" Journal of Physics: Conference Series, Volume 849, conference 1.

7.1 Principles

Here we present the results of the experiments described before, i.e. XRFM, AFM, 2D phase contrast imaging and nanotomography, on freeze dried (see chapter V) phagocytic cells, with the purpose to obtain quantitative mapping of Fe mass fraction and concentration (see chapter VI). We recall here that the iron homeostasis, involving the physiological ratio of iron between tissues/secretions and blood, is strictly regulated by ferroportin, the sole protein able to export iron from cells to blood. Inflammatory processes, induced by lipopolysaccharide (LPS) or bacterial pathogens, inhibit ferroportin synthesis in epithelial and phagocytic cells thus hindering iron export, increasing intracellular iron and bacterial multiplication. Therefore, Lf is an important regulator of both iron and inflammatory homeostasis, and it is important to understand its role in the variation of Fe distribution in the cells. To this purpose, we studied phagocytic cells inflamed by bacterial LPS and untreated or treated with milk derived bovine Lf.

7.1.1 Results: Fluorescence maps, Phase reconstruction map, Atomic Force Microscopy map, Density map, Iron Mass Fraction map, Iron Concentration map for all the cells

The X-ray fluorescence emission lines of several elements were collected by the silicon drift energy dispersive detectors positioned in the horizontal plane at 95° of the incoming X-ray beam. After acquisition the fluorescence spectra were analysed using the PyMCA free program [11], and the total counts of the Fe K lines, after subtraction of the backgrounds, were mapped as a function of the sample position with respect to the incoming beam (see chapter 6 paragraph 6.2.1). We analyzed cells treated in four different ways: a) control; b) inflamed by bacterial lipopolysaccharide (LPS) which simulates infection; c) treated with Lf; d) treated with LPS+LF. For some of the conditions more than one cell has been analyzed, to have better statistics. The resulting fluorescence map for each tipology of cell are displayed in Figures 7.1 **A,** 7.2 **A,** 7.3 **A,** 7.4 **A,** 7.5 **A,** 7.6 **A,** 7.7 **A,** 7.8 **A,** 7.9 **A,** 7.10 **A,** 7.11 **A,** 7.12 **A,** 7.13 **A,** 7.14 **A**. The PC projections were acquired at four different distances (29 mm, 30 mm, 34 mm, 44 mm) downstream of the X-ray focus resulting in magnified Fresnel patterns collected by a highly sensitive charge-coupled device (CCD) camera (see chapter VI paragraph 6.2.1). A complex procedure to retrieve the phase has been carried out [16, 7]. The results for each tipology of cells are shown in Figures 7.1 **B,** 7.2 **B,** 7.3 **B,** 7.4 **B,** 7.5 **B,** 7.6 **B,** 7.7 **B,** 7.8 **A,** 7.9 **B,** 7.10 **B,** 7.11 **B,** 7.12 **B,** 7.13 **B,** 7.14 **B**. AFM maps were collected with lateral spatial resolution of 100 nm and accuracy in the cell thickness measurement of about 30 nm (see chapter III). Images were collected without any real-time filtering or flattening, and were post-processed to eliminate all the possible artefacts [23]. The Figures 7.1 **C,** 7.2 **C,** 7.3 **C,** 7.4 **C,** 7.5 **C,** 7.6 **C,** 7.7 **C,** 7.8 **C,** 7.9 **C,** 7.10 **C,** 7.11 **C,** 7.12 **C,** 7.13 **C,** 7.14 **C** show the result of the AFM measurement. With the experimental results presented in Figures 7.1/.14A, and Figures 7.1/.14B, we were able to calculate the iron mass fraction. The iron mass fraction Figures 7.1 **D,** 7.2 **D,** 7.3 **D,** 7.4 **C,** 7.5 **D,** 7.6 **D,** 7.7 **D,** 7.8 **D,** 7.9 **D,** 7.10 **D,** 7.11 **D,** 7.12 **D,** 7.13 **D,** 7.14 **D**, is obtained normalizing the fluorescence map with the projected electron density derived by the analysis of the PCI. Preliminary to normalization is the registration (alignment) procedure between the fluorescence maps and the PC imaging.

Normalizing the phase reconstruction maps Figures 7.1/.14B with AFM map considering a phi-factor correction α calculated from the real part of the refractive index (see paragraph 6.2.3 Chapter6), it is possible to obtain the density distribution 7.1 **E,** 7.2 **E,** 7.3 **E,** 7.4 **C,** 7.5 **E,** 7.6 **E,** 7.7 **E,** 7.8 **E,** 7.9 **E,** 7.10 **E,** 7.11 **E,** 7.12 **E,** 7.13 **E,** 7.14 **E**.

The iron concentration Figures 7.1 **F,** 7.2 **F,** 7.3 **F,** 7.4 **F,** 7.5 **F,** 7.6 **F,** 7.7 **F,** 7.8 **F,** 7.9 **F,** 7.10 **F,** 7.11**F,** 7.12 **F,** 7.13 **F,** 7.14 **F**, is instead obtained by normalizing the fluorescence map Figures 7.1/.14 **A** with the volume of each pixel, as derived by the AFM Figures 7.1/.14 **C** (see paragraph 6.2.1 Chapter 6). As for the mass fraction map, it was necessary to register the fluorescence map with the AFM.

SAMPLE20 CELL 10 (CONTROL SAMPLE):

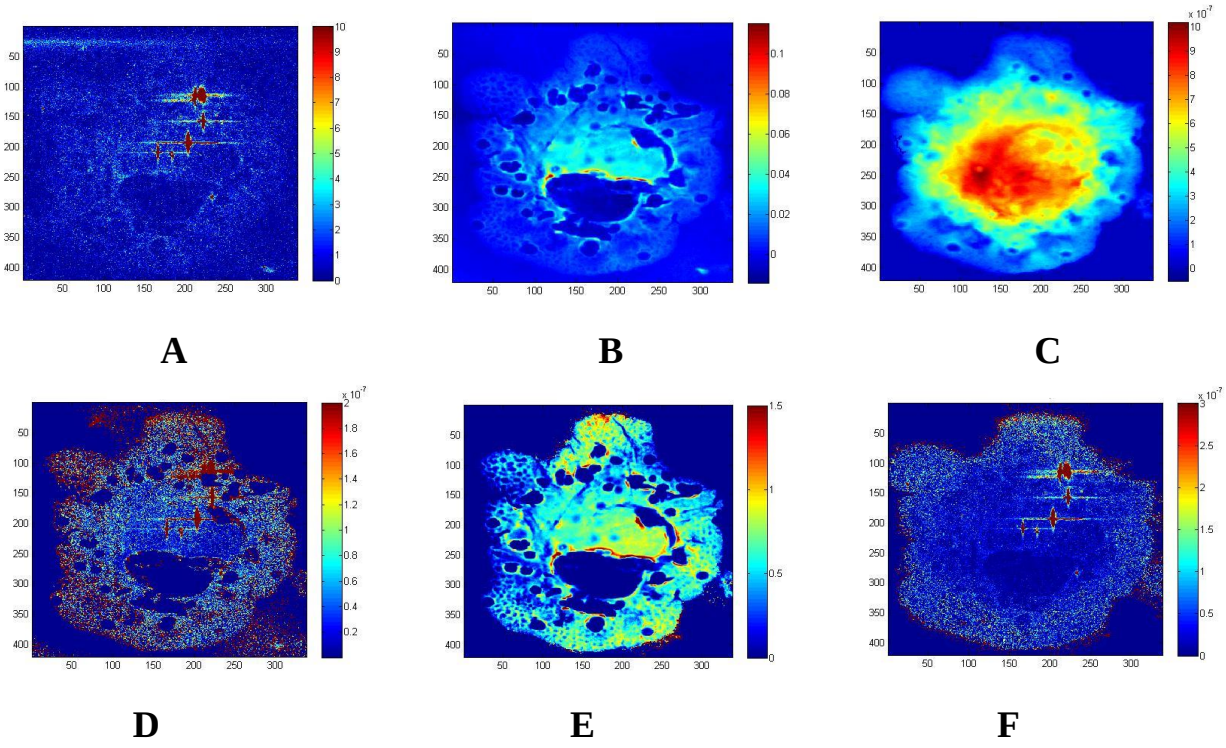

Figure 7.1: **A** *Iron Fluorescence intensity Map*, **B** *Phase contrast Map [rad]* **C** AFM Map *[µm]* **D** *Iron Mass Fraction Distribution Map* **E** *Density Map [g/cm^3]* **F** *Iron concentration map [nM] of the cell 10 of the control sample 20, the iron mass fraction map was obtained by normalizing the fluorescence intensity map with the phase map; the iron concentration map was obtained by normalizing the fluorescence intensity map with the volume information obtained by the AFM.*

+SAMPLE 21 CELL 1 TREATED WITH LF

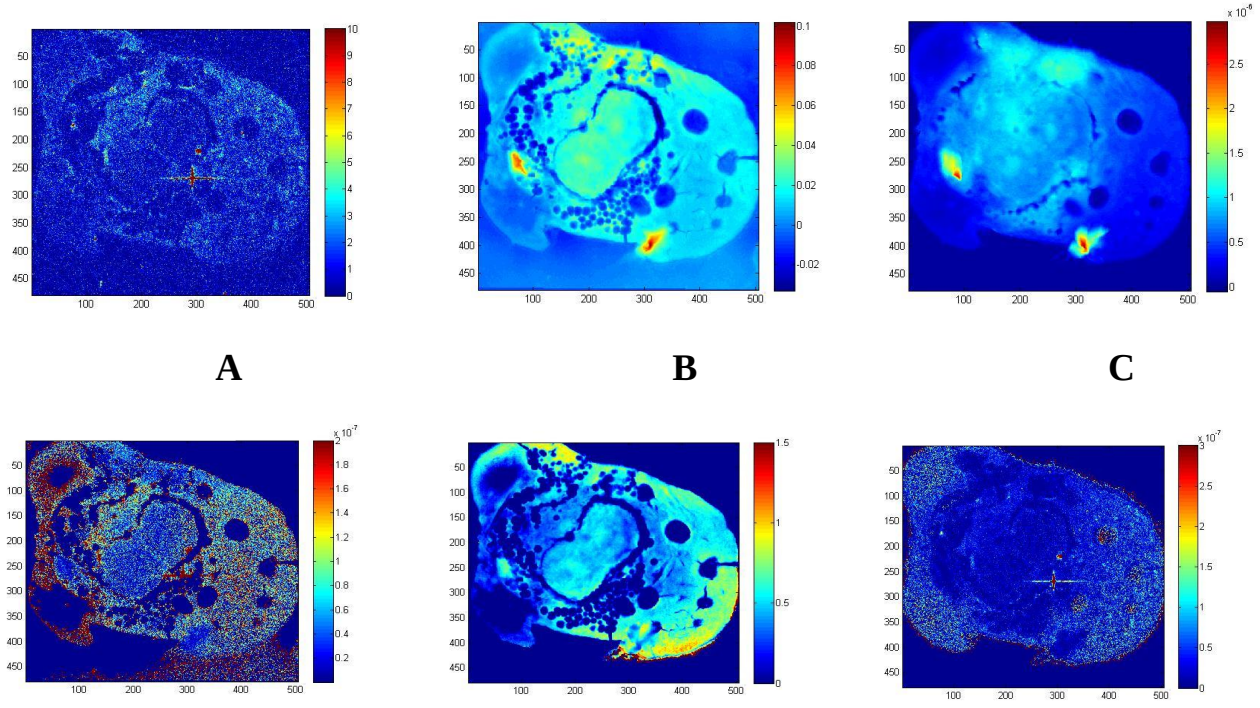

A **B** **C**

D **E** **F**

Figure 7.2: **A** *Iron Fluorescence intensity Map*, **B** *Phase contrast Map [rad]* **C** AFM Map *[µm]* **D** *Iron Mass Fraction Distribution Map* **E** *Density Map [g/cm^3]* **F** *Iron concentration map [nM] of* ***sample 21 cell 1*** *treated with* **Lf**, *the iron mass fraction map was obtained by normalizing the fluorescence intensity map with the phase map; the iron concentration map was obtained by normalizing the fluorescence intensity map with the volume information obtained by the AFM.*

SAMPLE 21 CELL 2 TREATED WITH LF

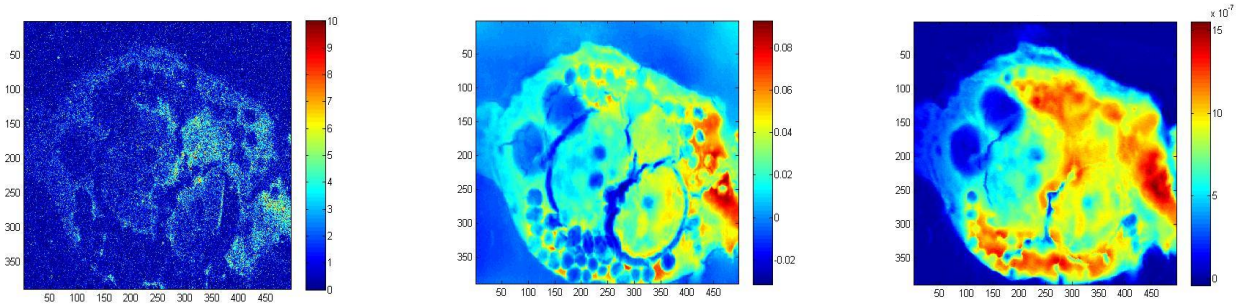

A **B** **C**

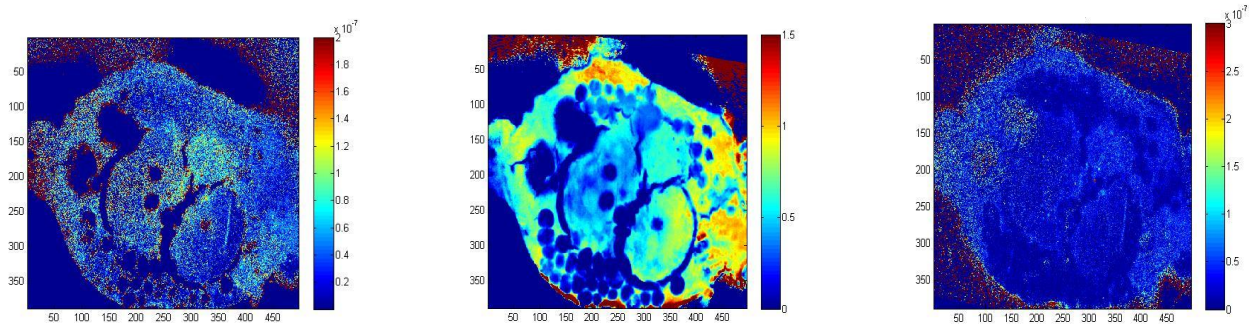

D **E** **F**

Figure 7.3: **A** *Iron Fluorescence intensity Map*, **B** *Phase contrast Map [rad]* **C** AFM Map *[µm]* **D** *Iron Mass Fraction Distribution Map* **E** *Density Map [g/cm^3]* **F** *Iron concentration map [nM] of the* ***sample 21 cell 2*** *treated with* **Lf**, *the iron mass fraction map was obtained by normalizing the fluorescence intensity map with thephase map*; *the iron concentration map was obtained by normalizing the fluorescence intensity map with the volume information obtained by the AFM.*

SAMPLE 21 CELL 4 TREATED WITH LF

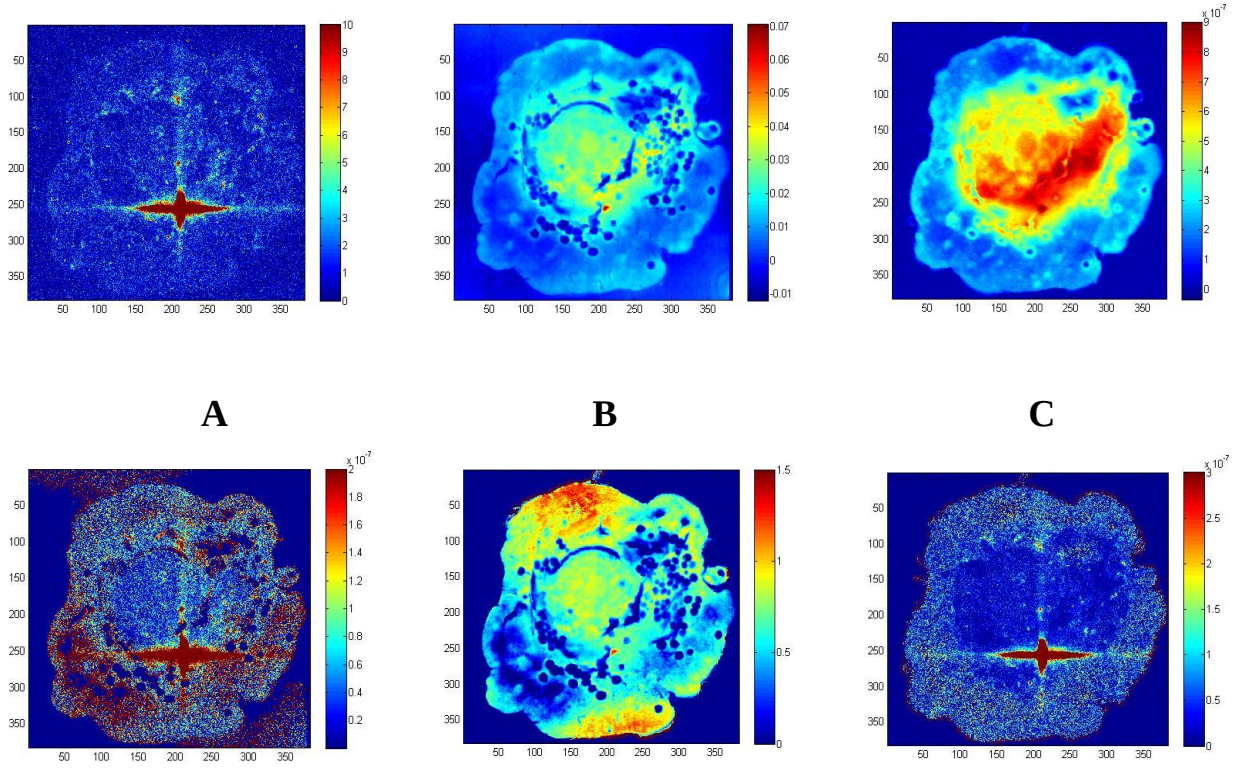

A **B** **C**

D **E** **F**

Figure 7.4: **A** *Iron Fluorescence intensity Map*, **B** *Phase contrast Map [rad]* **C** AFM Map *[µm]* **D** *Iron Mass Fraction Distribution Map* **E** *Density Map [g/cm^3]* **F** *Iron concentration map [nM] of the* ***sample 21 cell 4*** *treated with* **Lf**, *the iron mass fraction map was obtained by normalizing the fluorescence intensity map with thephase map*; *the iron concentration map was obtained by normalizing the fluorescence intensity map with the volume information obtained by the AFM.*

SAMPLE 27 CELL 3 TREATED WITH LF AND LPS

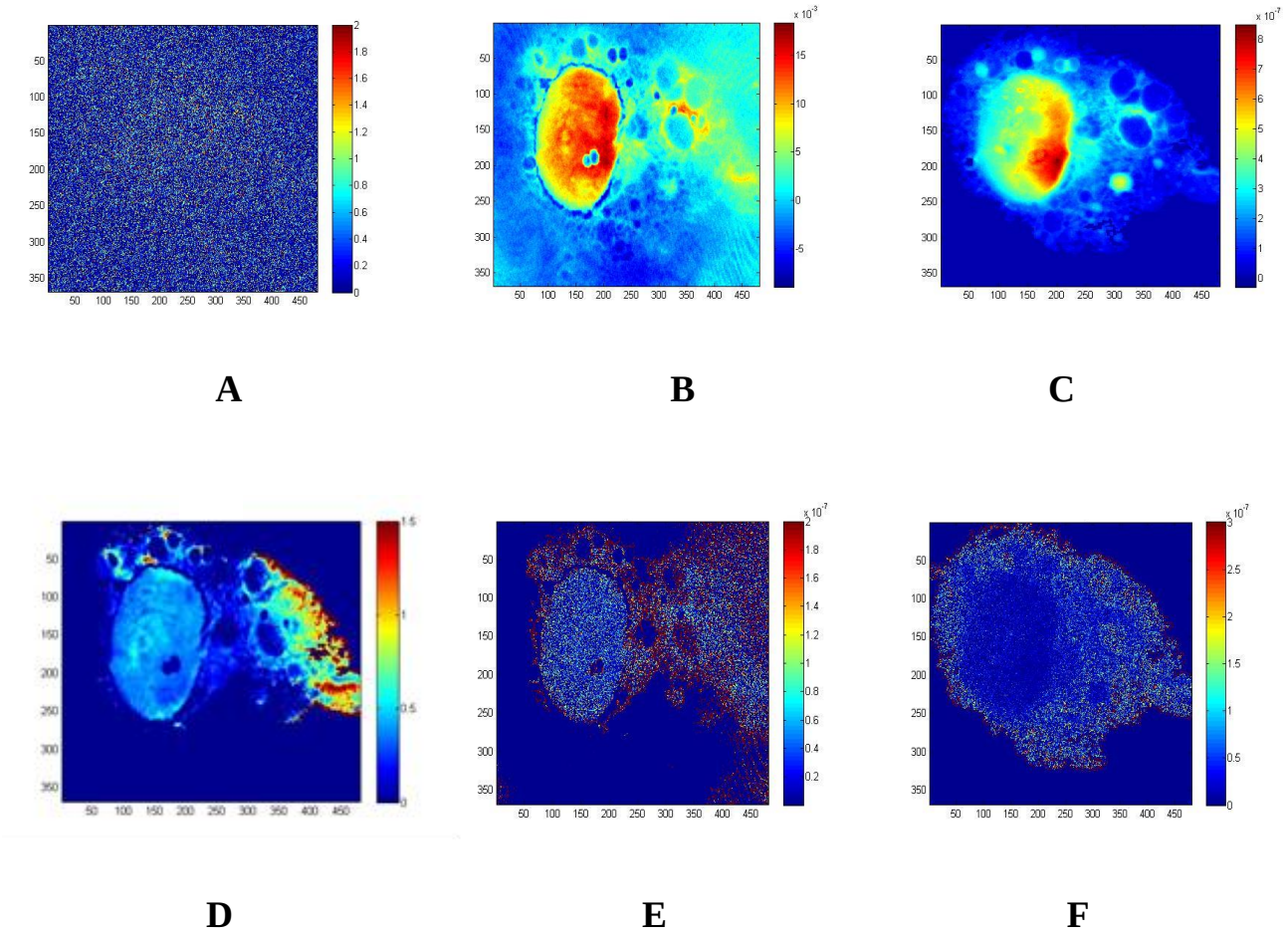

A **B** **C**

D **E** **F**

Figure 7.5: **A** *Iron Fluorescence intensity Map,* **B** *Phase contrast Map [rad]* **C** AFM Map *[µm]* **D** *Iron Mass Fraction Distribution Map* **E** *Density Map [g/cm^3]* **F** *Iron concentration map [nM] of the* ***sample 27 cell 3*** *treated with* **Lf + LPS**, *the iron mass fraction map was obtained by normalizing the fluorescence intensity map with thephase map; the iron concentration map was obtained by normalizing the fluorescence intensity map with the volume information obtained by the AFM.*

SAMPLE 27 CELL 5 TREATED WITH LF AND LPS

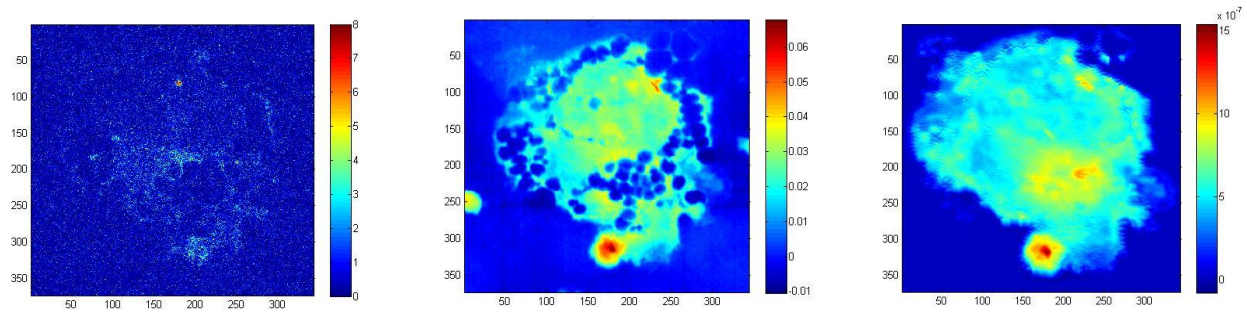

A **B** **C**

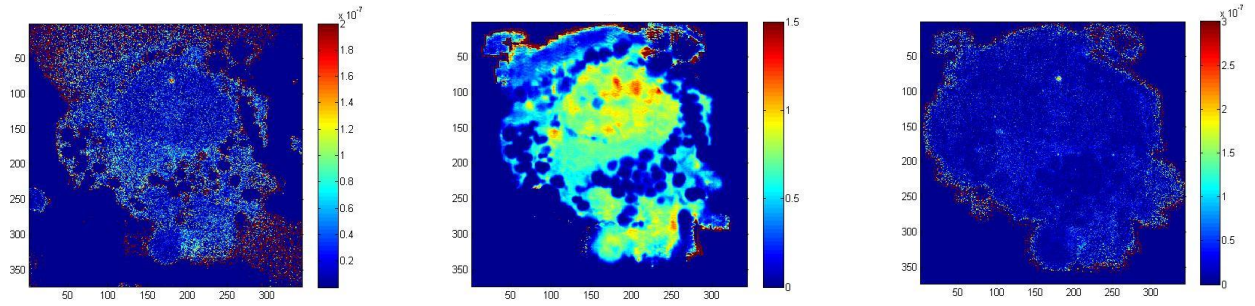

D **E** **F**

Figure 7.6: **A** *Iron Fluorescence intensity Map,* **B** *Phase contrast Map [rad]* **C** AFM Map *[µm]* **D** *Iron Mass Fraction Distribution Map* **E** *Density Map [g/cm^3]* **F** *Iron concentration map [nM] of the* ***sample 27 cell 5*** *treated with* **Lf + LPS**, *the iron mass fraction map was obtained by normalizing the fluorescence intensity map with thephase map; the iron concentration map was obtained by normalizing the fluorescence intensity map with the volume information obtained by the AFM.*

SAMPLE 27 CELL7 TREATED WITH LF AND LPS

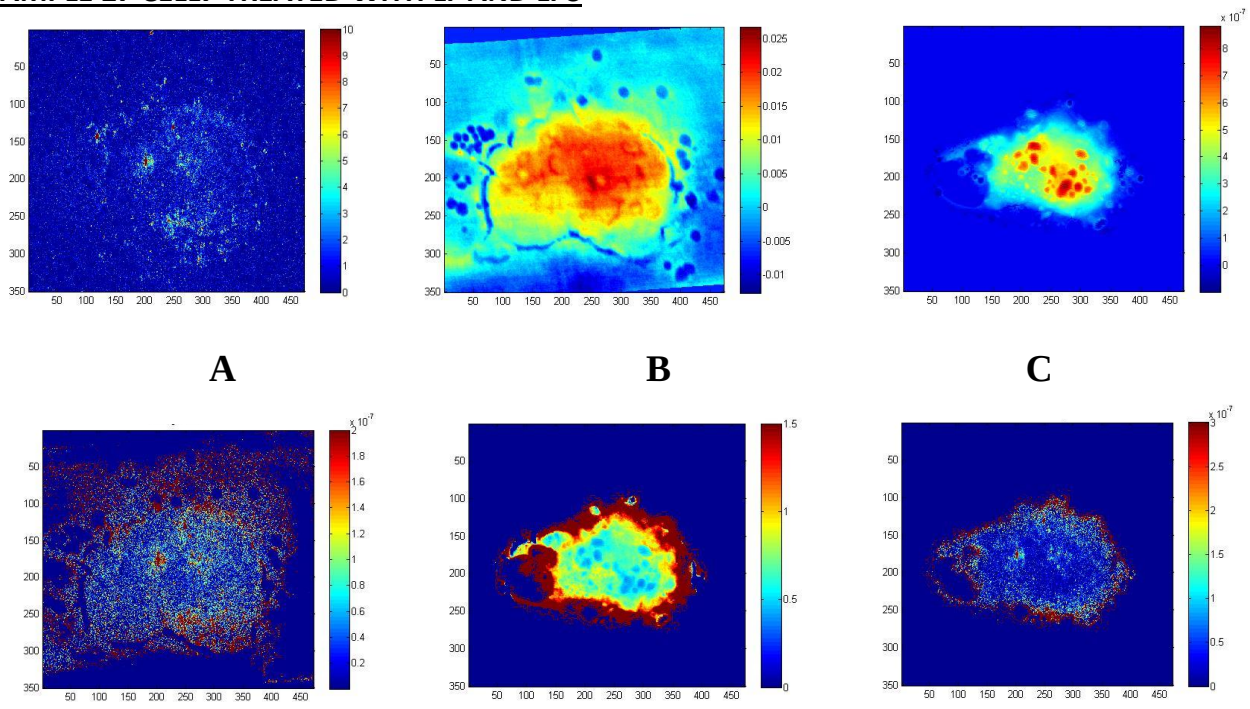

A **B** **C**

D **E** **F**

Figure 7.7: **A** *Iron Fluorescence intensity Map,* **B** *Phase contrast Map [rad]* **C** AFM Map *[µm]* **D** *Iron Mass Fraction Distribution Map* **E** *Density Map [g/cm^3]* **F** *Iron concentration map [nM] of the* ***sample 27 cell 7*** *treated with* **Lf + LPS**, *the iron mass fraction map was obtained by normalizing the fluorescence intensity map with thephase map; the iron concentration map was obtained by normalizing the fluorescence intensity map with the volume information obtained by the AFM.*

SAMPLE 44 CELL 1 TREATED WITH LF

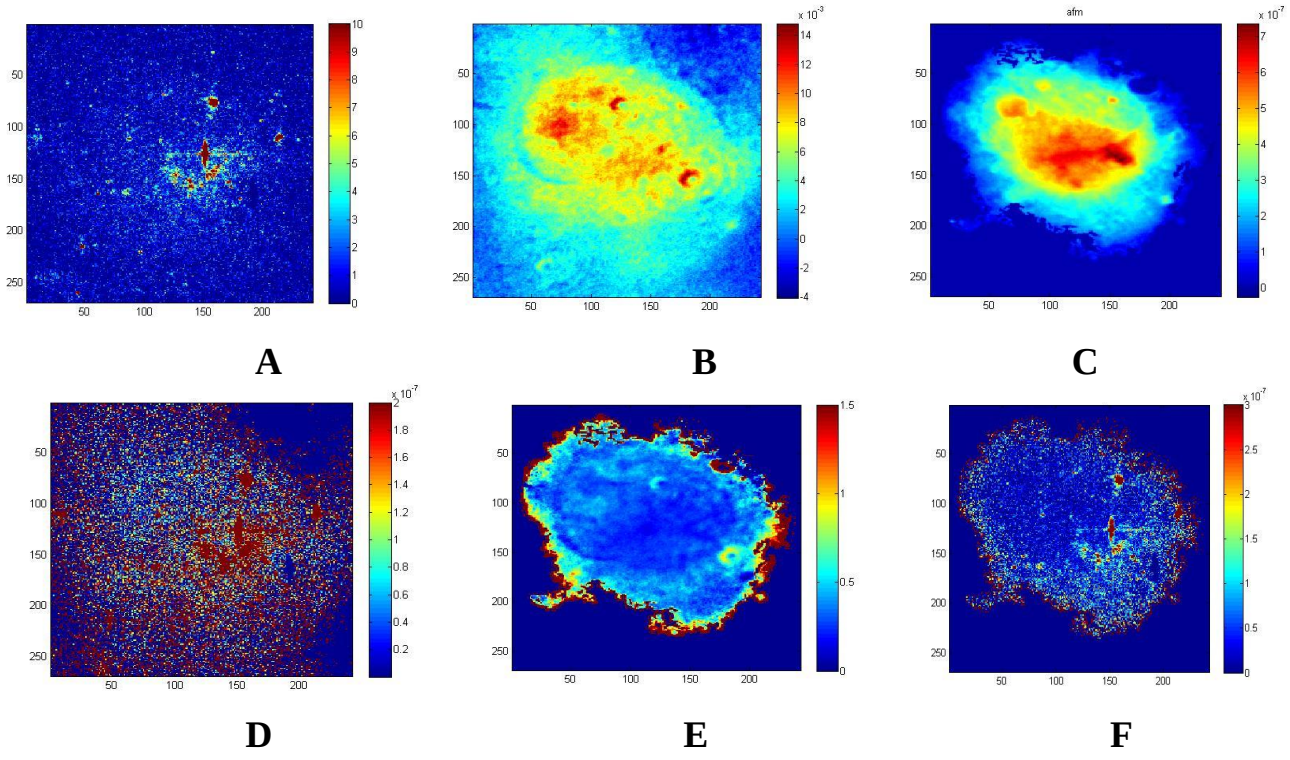

Figure 7.8: **A** *Iron Fluorescence intensity Map,* **B** *Phase contrast Map [rad]* **C** AFM Map *[µm]* **D** *Iron Mass Fraction Distribution Map* **E** *Density Map [g/cm^3]* **F** *Iron concentration map [nM] of the* ***sample 44 cell 1*** *treated with* **Lf**, *the iron mass fraction map was obtained by normalizing the fluorescence intensity map with thephase map; the iron concentration map was obtained by normalizing the fluorescence intensity map with the volume information obtained by the AFM.*

SAMPLE 44 CELL 2 TREATED WITH LF

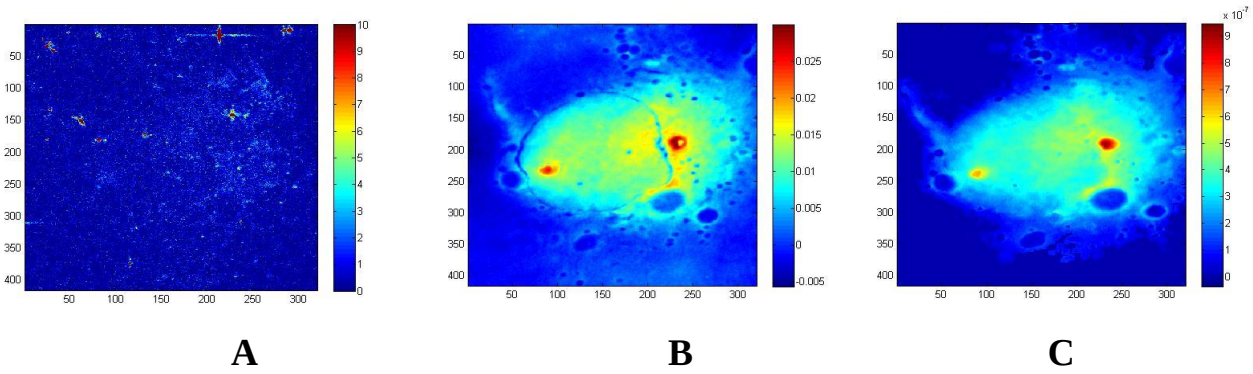

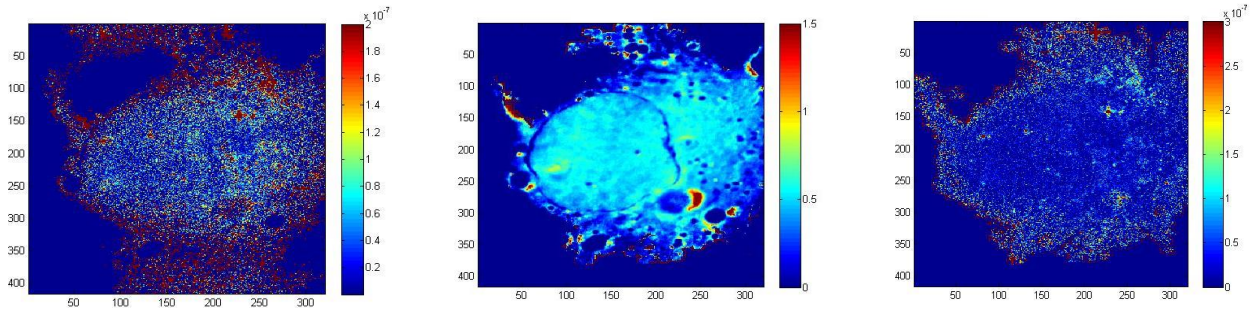

D **E** **F**

Figure 7.9: **A** *Iron Fluorescence intensity Map,* **B** *Phase contrast Map [rad]* **C** AFM Map*[µm]* **D** *Iron Mass Fraction Distribution Map* **E** *Density Map [g/cm^3]* **F** *Iron concentration map [nM] of the* ***sample 44 cell 2*** *treated with* **Lf**, *the iron mass fraction map was obtained by normalizing the fluorescence intensity map with thephase map; the iron concentration map was obtained by normalizing the fluorescence intensity map with the volume information obtained by the AFM.*

SAMPLE 44 CELL 4 TREATED WITH LF

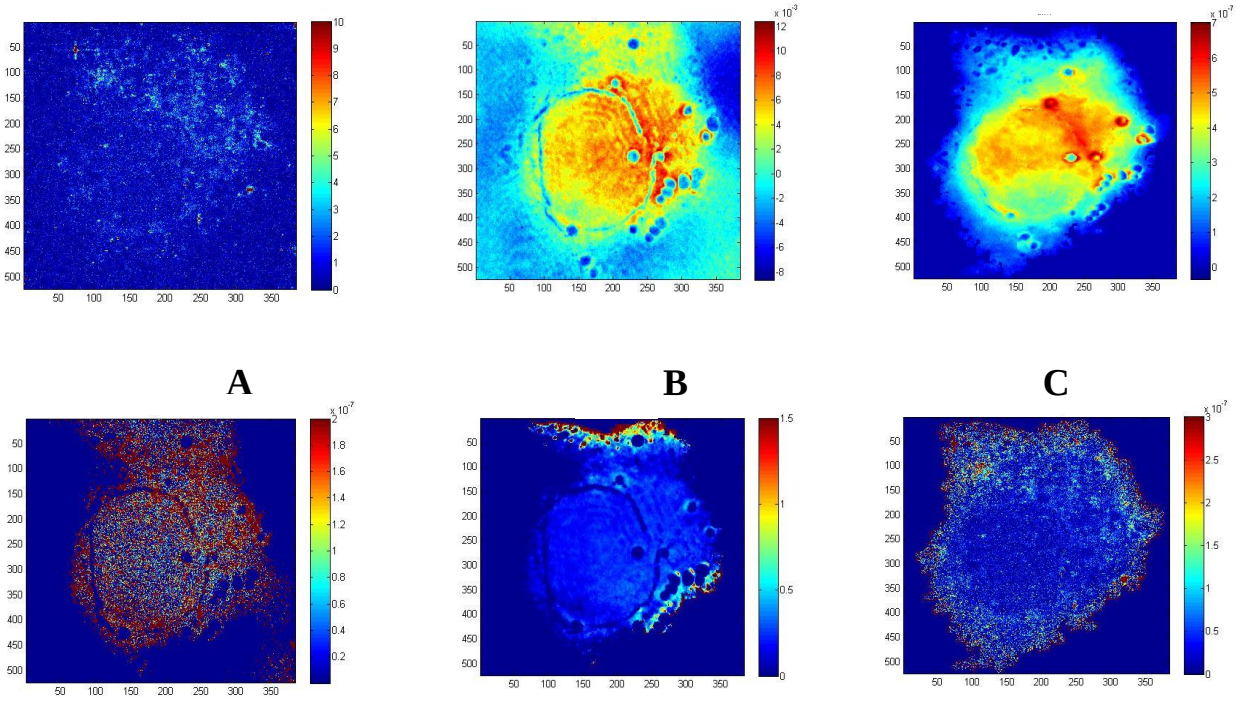

A **B** **C**

D **E** **F**

Figure 7.10: **A** *Iron Fluorescence intensity Map,* **B** *Phase contrast Map [rad]* **C** AFM Map *[µm]* **D** *Iron Mass Fraction Distribution Map* **E** *Density Map [g/cm^3]* **F** *Iron concentration map [nM]of the* ***sample 44 cell4*** *treated with* **Lf**, *the iron mass fraction map was obtained by normalizing the fluorescence intensity map with thephase map; the iron concentration map was obtained by normalizing the fluorescence intensity map with the volume information obtained by the AFM.*

SAMPLE 46 CELL2 TREATED WITH LPS

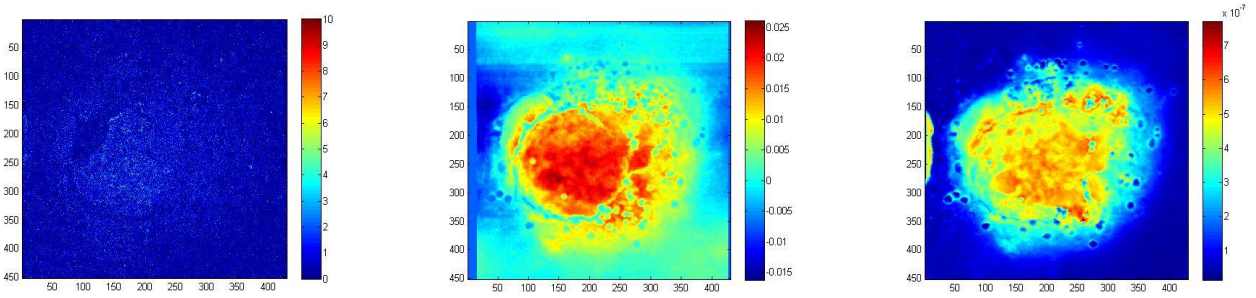

A **B** **C**

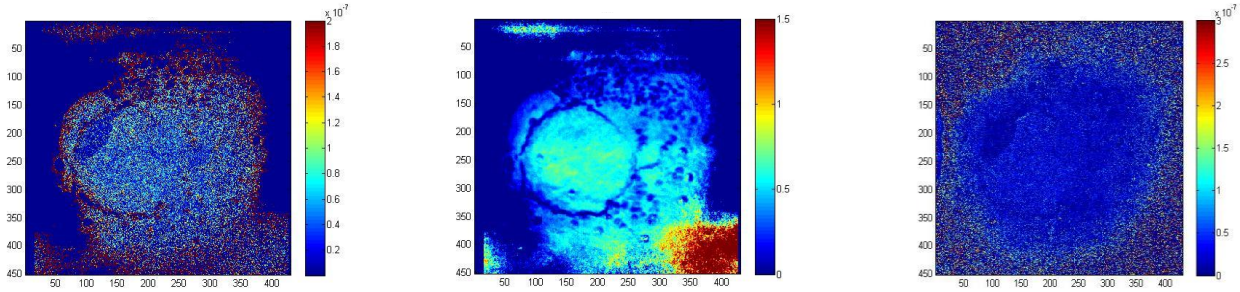

D **E** **F**

Figure 7.11: **A** *Iron Fluorescence intensity Map*, **B** *Phase contrast Map [rad]* **C** AFM Map *[µm]* **D** *Iron Mass Fraction Distribution Map* **E** *Density Map [g/cm^3]* **F** *Iron concentration map [nM]of the* ***sample 46cell 2*** *treated with* **LPS**, *the iron mass fraction map was obtained by normalizing the fluorescence intensity map with thephase map; the iron concentration map was obtained by normalizing the fluorescence intensity map with the volume information obtained by the AFM.*

SAMPLE 46 CELL6 TREATED WITH LPS

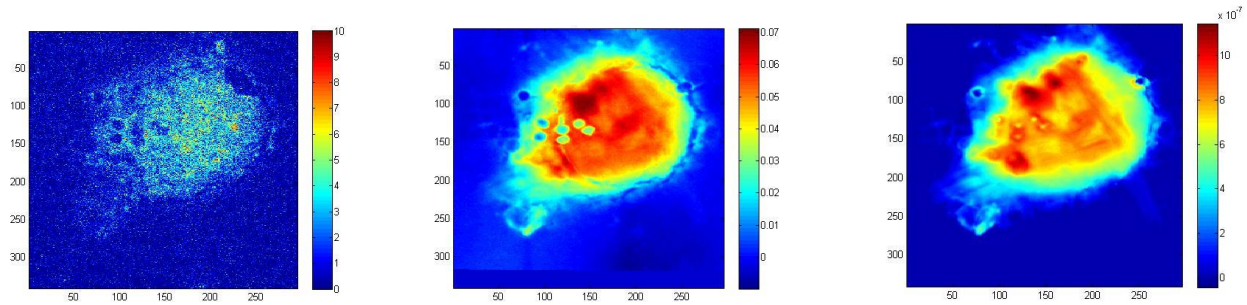

A **B** **C**

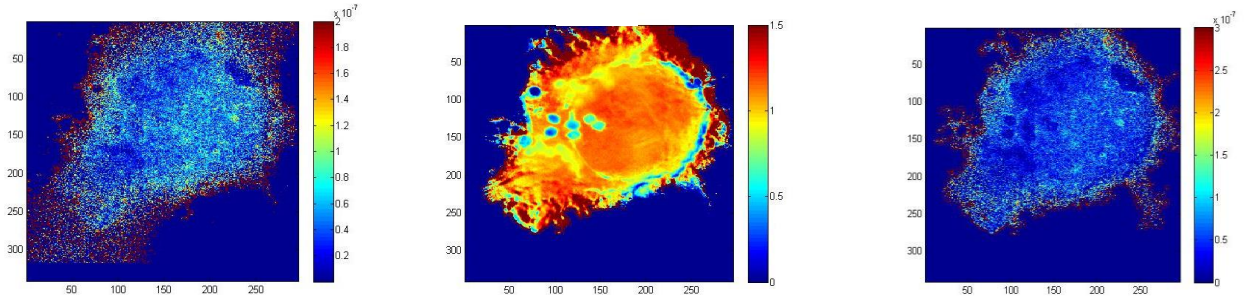

D **E** **F**

Figure 7.12: **A** *Iron Fluorescence intensity Map,* **B** *Phase contrast Map [rad]* **C** AFM Map *[µm]* **D** *Iron Mass Fraction Distribution Map* **E** *Density Map [g/cm^3]* **F** *Iron concentration map [nM]of the* ***sample 46 cell 6*** *treated with* **LPS**, *the iron mass fraction map was obtained by normalizing the fluorescence intensity map with thephase map; the iron concentration map was obtained by normalizing the fluorescence intensity map with the volume information obtained by the AFM.*

SAMPLE 46 CELL7 TREATED WITH LPS

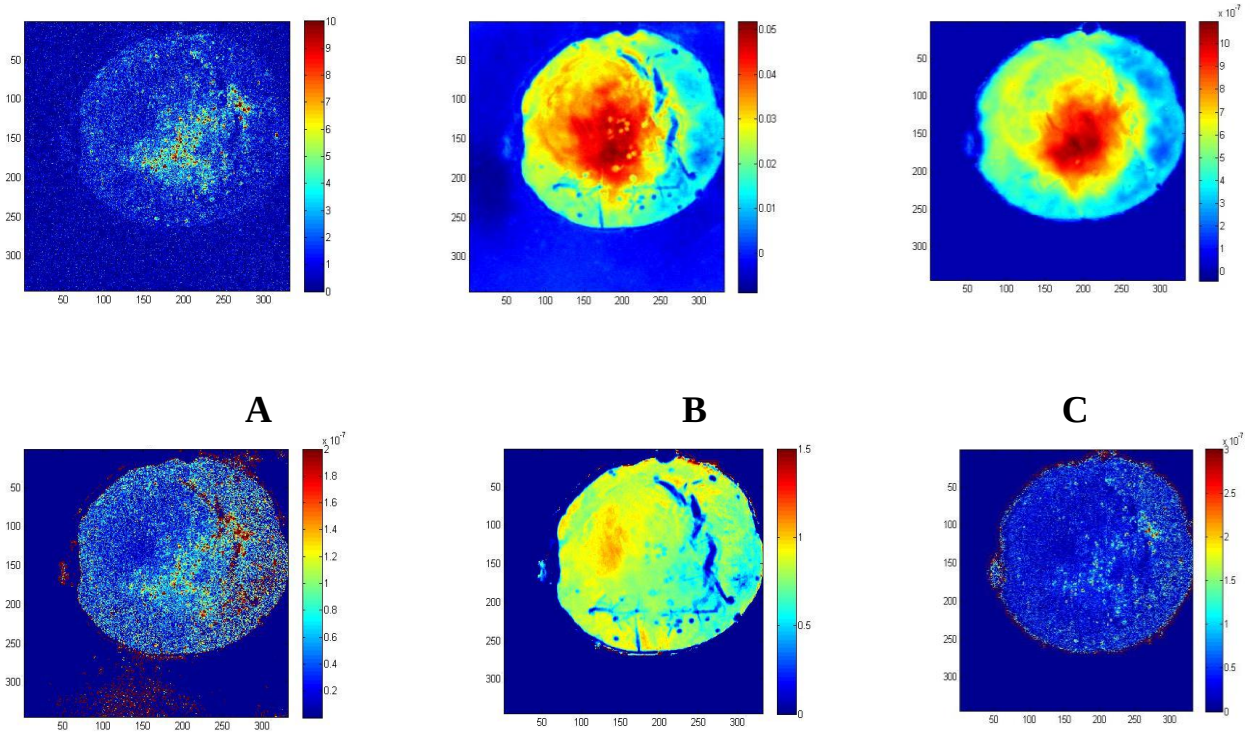

A **B** **C**

D **E** **F**

Figure 7.13: **A** *Iron Fluorescence intensity Map,* **B** *Phase contrast Map [rad]* **C** AFM Map *[µm]* **D** *Iron Mass Fraction Distribution Map* **E** *Density Map [g/cm^3]* **F** *Iron concentration map [nM]of the* ***sample 46 cell 7*** *treated with* **LPS**, *the iron mass fraction map was obtained by normalizing the fluorescence intensity map with thephase map; the iron concentration map was obtained by normalizing the fluorescence intensity map with the volume information obtained by the AFM.*

SAMPLE 46 CELL 8 TREATED WITH LPS

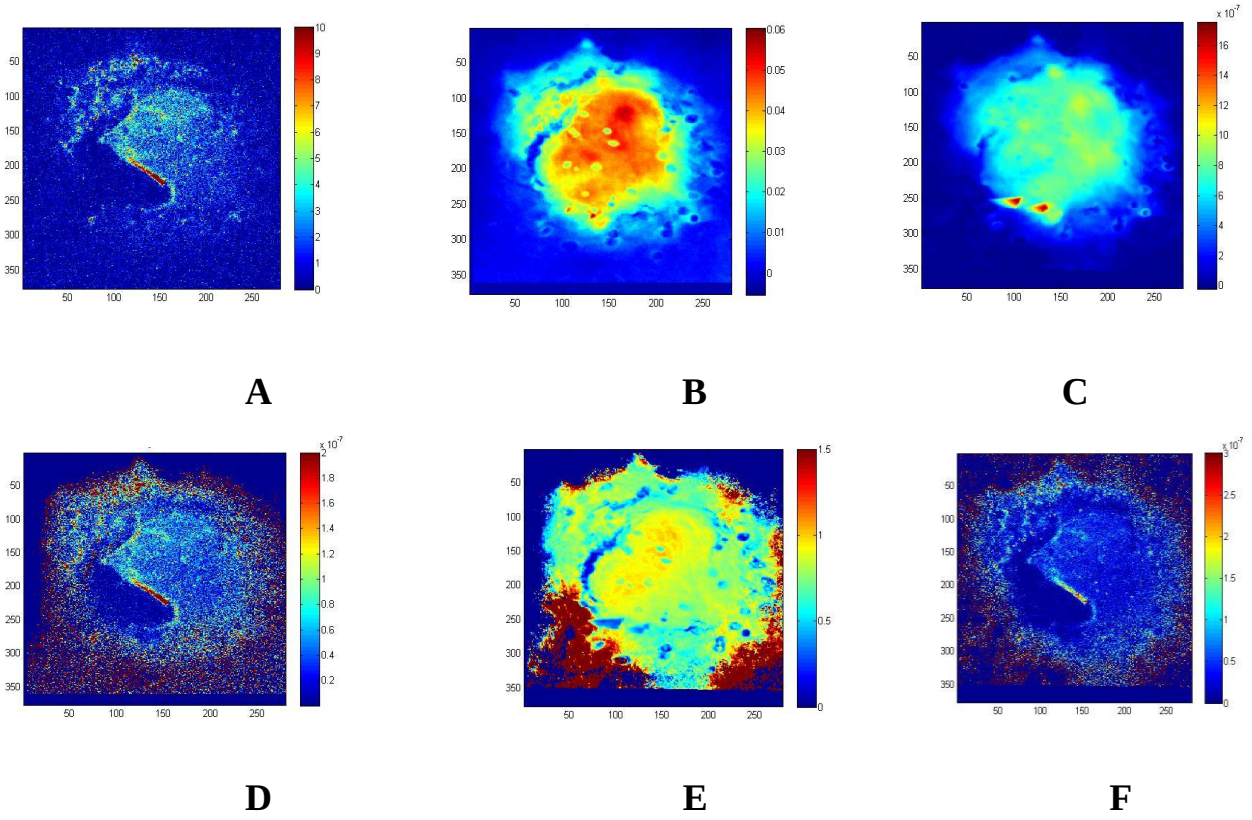

A **B** **C**

D **E** **F**

Figure 7.14: **A** *Iron Fluorescence intensity Map,* **B** *Phase contrast Map [rad]* **C** AFM Map *[µm]* **D** *Iron Mass Fraction Distribution Map* **E** *Density Map [g/cm^3]* **F** *Iron concentration map [nM]of the* ***sample 46 cell 8*** *treated with* **LPS**, *the iron mass fraction map was obtained by normalizing the fluorescence intensity map with thephase map; the iron concentration map was obtained by normalizing the fluorescence intensity map with the volume information obtained by the AFM.*

Interestingly, the cellular iron distribution in LPS-treated cell (Figure 7.13 D) appeared different respect to that of LPS-treated cell in the presence of bLf (Figure 7.9 D) being located around the cytoplasm membrane cell, suggesting the reduction of its export probably associated to the inhibition of ferroportin [21, 13]. Unfortunately, since the cells have been altered by the freeze-drying process, significant biological considerations can not be taken as opposed to frozen hydrated (see chapter VIII) .

7.1.2 Results: Nanotomography and Iron concentrations map with volume informations extracted by Phase contrast Tomography

This paragraph is based on the article submitted in the Applied Physics Letters:

Gramaccioni C., Yang Y., Pacureanu A., Cloetens P., Bohic S., Malucelli E., Iotti S., Procopio A., Bukreeva I., Notargiacomo A., Fratini M., Valenti P., Rosa L., Berlutti F. and Lagomarsino S. **"Nanoscale quantitative determination of intracellular element concentration combining X-ray fluorescence microscopy with holotomography."**

We recall here the results of the nanotomography, carried out on sample 46, cell 7. As described in chapter 6, we were able to obtain the cell thickness from the tomographic reconstruction. We compare here the results obtained with tomography with those obtained with AFM. Fig. 7.15 shows the electronic density map, both viewed in front and from the profile, illustrating the striking difference between the thickness and the width of the cell.

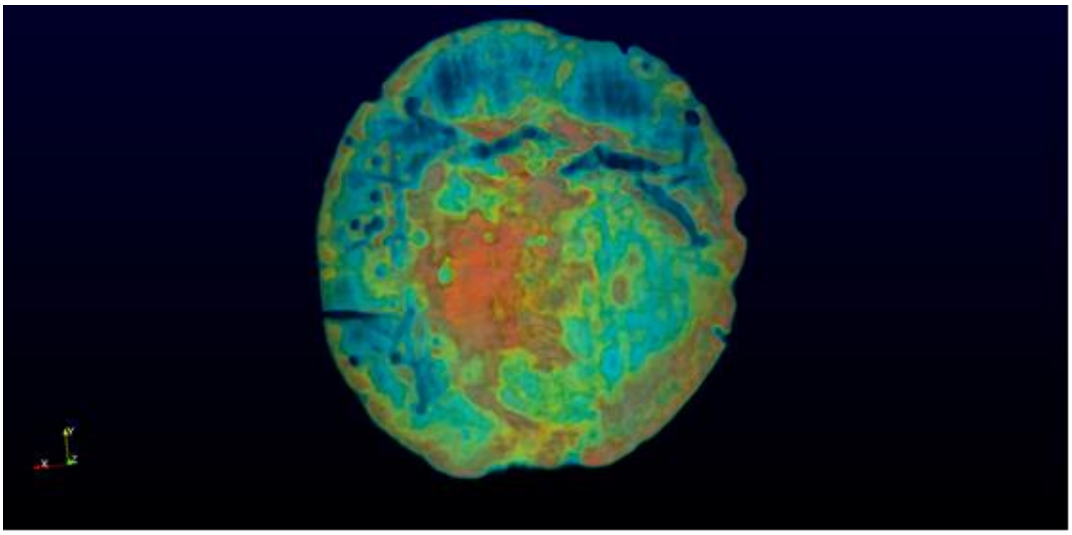

A

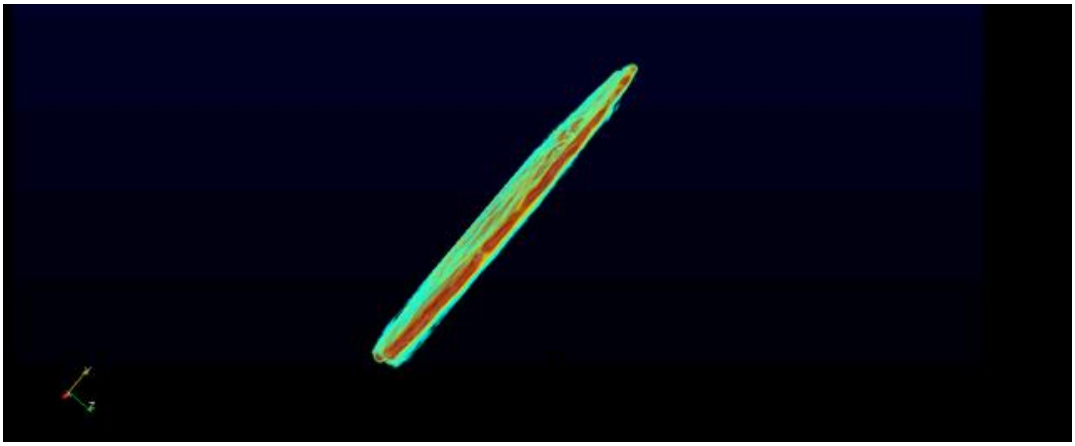

B

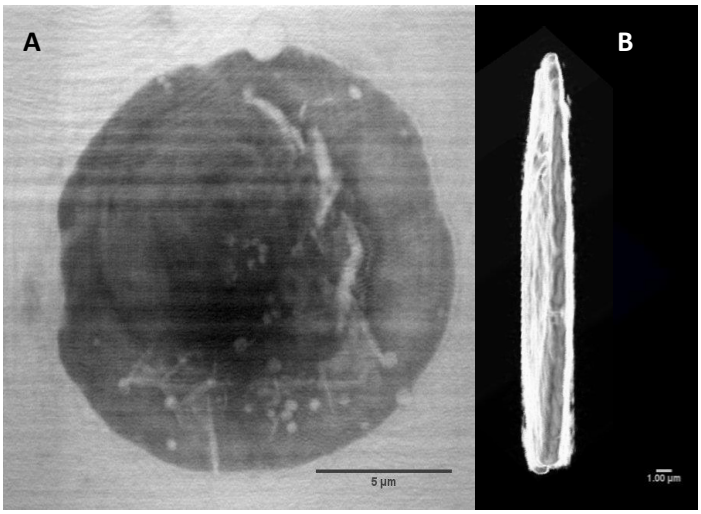

Figure 7.15: *Projected Density Map from Nanotomography of the* ***sample 46 cell 7*** *treated with* **LPS, A** *front and* **B** *side projections.*

The thickness has been determined by using segmentation, for best accuracy. Fig. 7.16 A and B show the comparison between the thickness determined by the AFM (7.16 A) and by tomography (7.16 B). The comparison shows that the main cell feature are reproduced in similar way by the two techniques. Furthermore, in the tomography picture quite deep holes are evident, which are not seen by the AFM. From a careful analysis of the slices, we can affirm that the holes are mainly below the surface, and therefore they cannot be seen by the AFM. This demonstrates the powerful of the tomography technique.

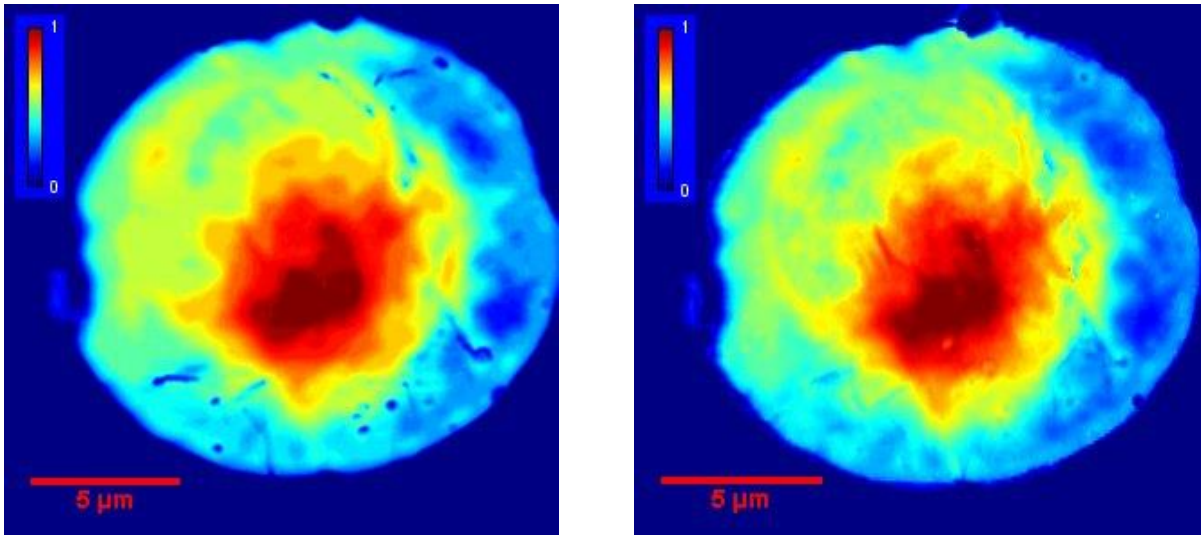

A **B**

Figure 7.15: A *Thickness maps from Nanotomography [µm]*, ***B*** *Thickness maps from AFM [µm] of the* ***sample 46 cell 7*** *treated with* **LPS.**

Then we normalized, after registration, the fluorescence map with the cell thickness, obtained either by AFM or by tomography. The results are compared in fig. 7.16. As usual, where the thickness is zero, and therefore normalization would diverge, we put concentration to zero. The two maps give essentially very similar spatial distribution. This work opens the way to quantitative biological analysis at nanometer spatial resolution using exclusively synchrotron radiation techniques. This makes possible to study also frozen hydrated cells where AFM cannot be used.

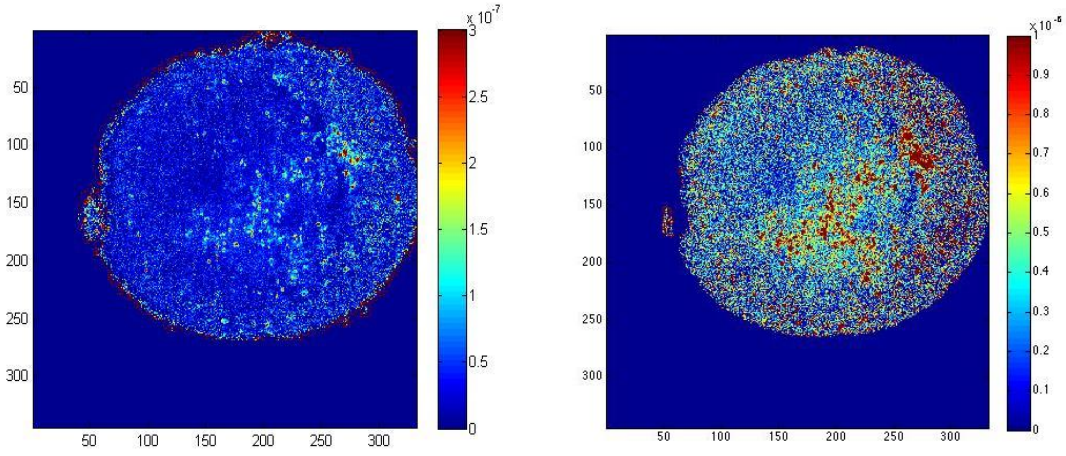

A **B**

Figure 7.16: A *Iron Concentrations maps from AFM [nM]*, ***B*** *Iron Concentrations maps from Nanotomography [nM] of the* ***sample 46 cell 7*** *treated with* **LPS.**

Riassunto del Capitolo 7 in Italiano

In questo capitolo sono presentati e descritti tutti i risultati derivati dall'analisi delle cellule freeze-dried. In particolare sono riportate le mappe di Phase contrast imaging 2D e 3D, e di fluorescenza e di AFM dacui poi si sono ottenute le mappe di mass fraction, concentrazione, e di densità.

Chapter 8

DESCRIPTION OF EXPERIMENT ON FROZEN HYDRATED CELLS AND RESULTS

8.1.1 Results: Fluorescence maps, Phase reconstruction map, Iron Mass Fraction map, Iron for all the cells

We analyzed cells treated in four different ways: a) control; b) inflamed by bacterial lipopolysaccharide (LPS) which simulates infection; c) treated with Lf; d) treated with LPS+LF as presented in the chapter 7 for the freeze-dried cells. Our experiment was the first that acquired Phase contrast 2D and 3D on frozen hydrated cells at ID16NI beamline, so we had some technical problems during the run of the experiment. In this case, we analyzed also the Potassium K line. Potassium is an essential component of the cells, that is found to distribute homogeneously throughout the cell, and can therefore give cell conformation.

The PC projections were acquired at four different distances (29 mm, 30 mm, 34 mm, 44 mm) downstream of the X-ray focus resulting in magnified Fresnel patterns collected by a highly sensitive charge-coupled device (CCD) camera (see chapter VI paragraph 6.2.1). The same procedure to retrieve the phase adopted in the case of freeze-dried cells has been carried out [16, 7]. The results for each tipology of cells are shown in Figures 8.1 **A**, 8.2 **A**, 8.3 **A**, 8.4 **A**, 8.5 **A**, 8.6 **A**, 8.7 **A,** 8.8 **A**, 8.9 **A**, 8.10 **A**,. The resulting fluorescence map for each tipology of cell are displayed in Figures 8.1 **B-C-D**, 8.2 **B-C-D-E**, 8.3 **B-C-D-E**, 8.4 **B-C-D-E**, 8.5 **B-C-D-E**, 8.6 **B-C-D-E**, 8.7 **B-C-D-E**, 8.8 **B-C-D-E**, 8.9 **B-C-D-E**, 8.10 **B-C-D-E**.

The iron mass fraction Figures 8.9 **F,** 8.10 **F**, is obtained normalizing the fluorescence map with the projected electron density derived by the analysis of the PCI.

CTRL 78 CELL 6 A

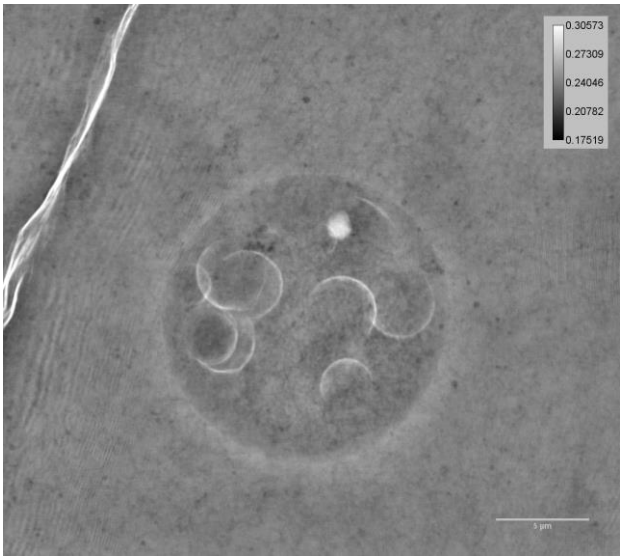

A

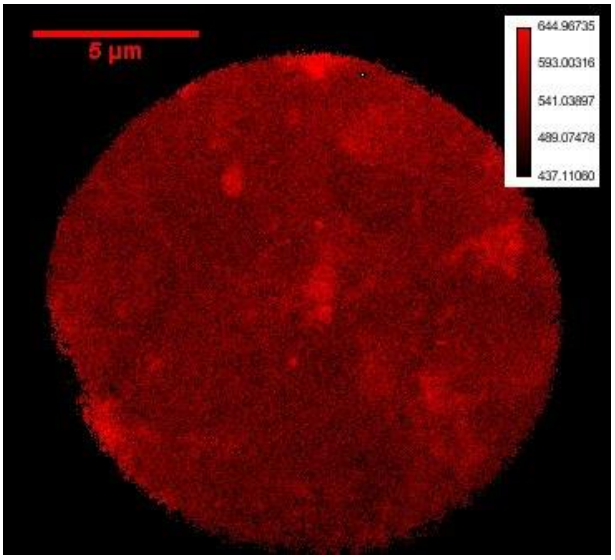

B

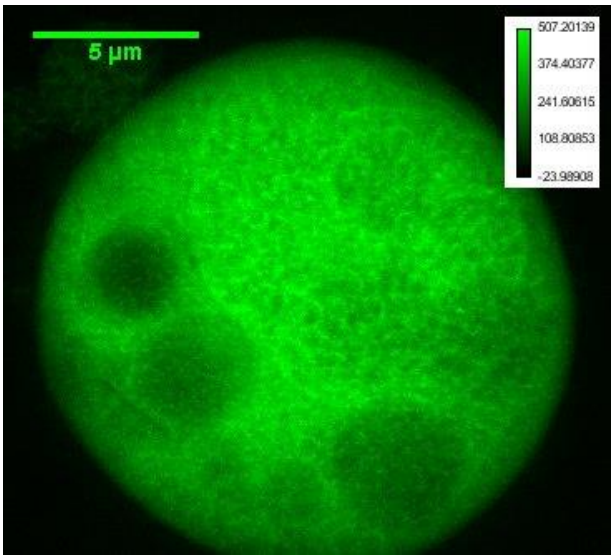

C

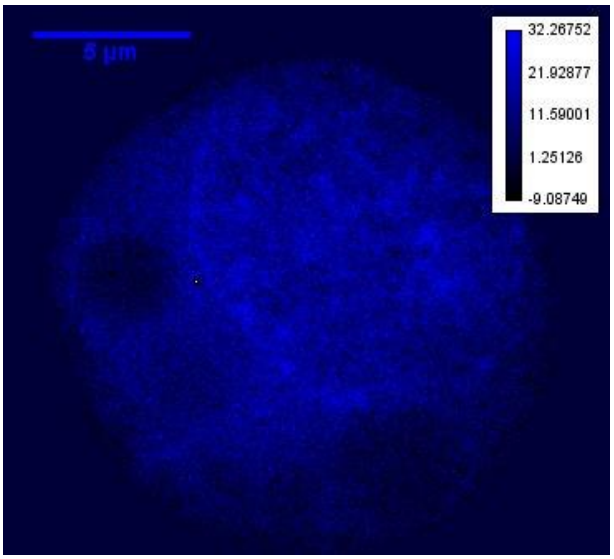

D

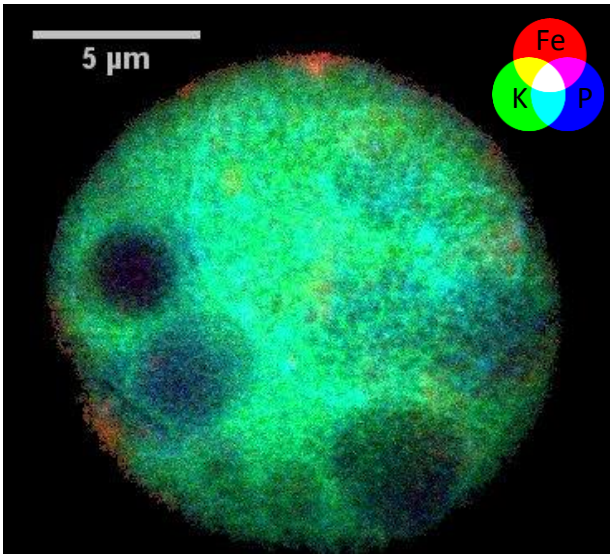

E

***8.1*: A** *Phase contrast Map [rad] [25 nm pixelsize]*, **B** *Iron Fluorescence intensity Map [50 nm pixelsize]*, **C** *Potassium Fluorescence intensity Ma [50 nm pixelsize]*, **D** *Phosphorus Fluorescence intensity Ma [50 nm pixelsize]*, **E** *Fluorescence intensity Composite Map of Phosphorus, Potassium and Iron [50 nm pixelsize]*.

CTRL 78 CELL 6 B

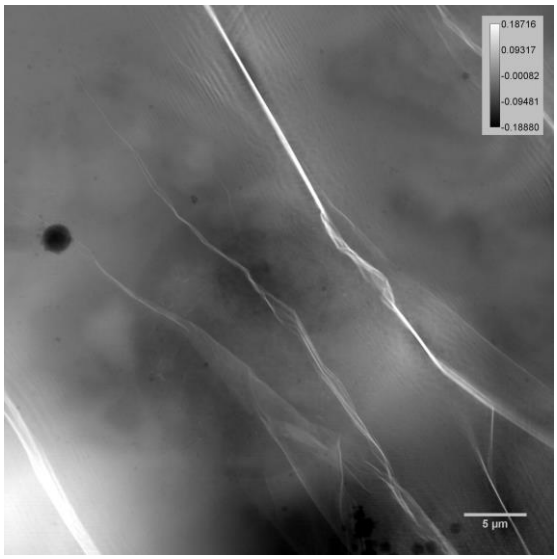

A

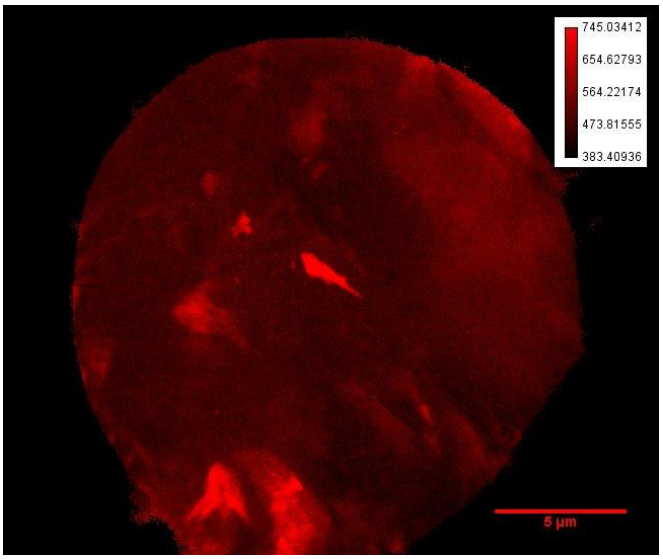

B

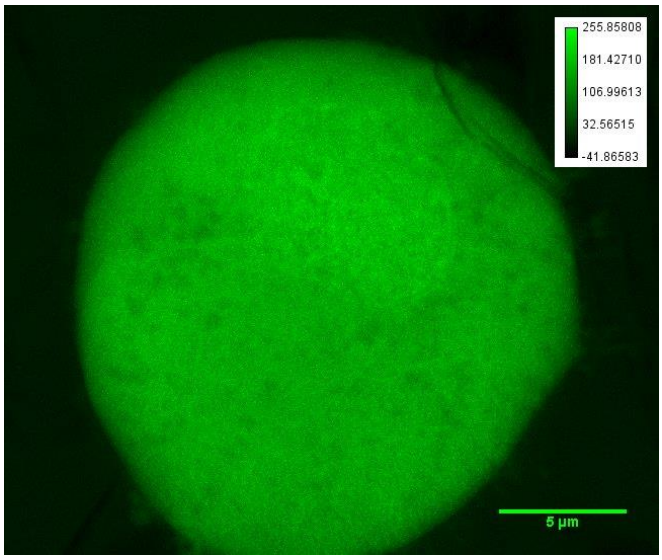

C

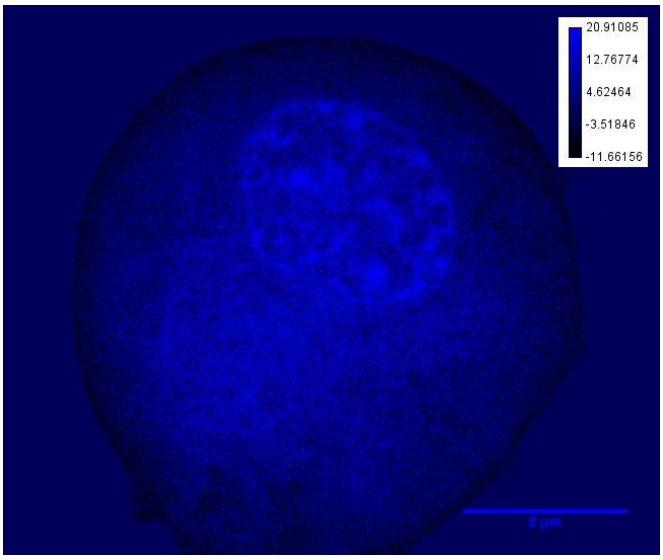

D

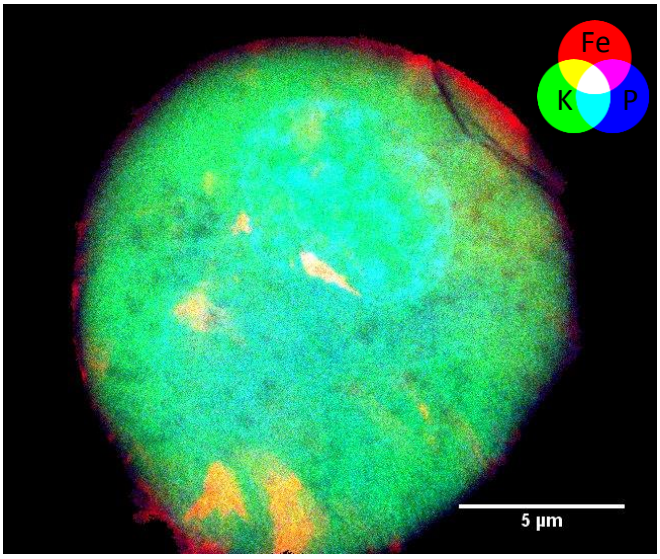

E

***8.2**: **A** Phase contrast Map [rad] [25 nm pixelsize], **B** Iron Fluorescence intensity Map [50 nm pixelsize], **C** Potassium Fluorescence intensity Map [50 nm pixelsize], **D** Phosphorus Fluorescence intensity Ma [50 nm pixelsize], **E** Fluorescence intensity Composite Map of Phosphorus, Potassium and Iron [50 nm pixelsize].*

CTRL 202 CELL 1

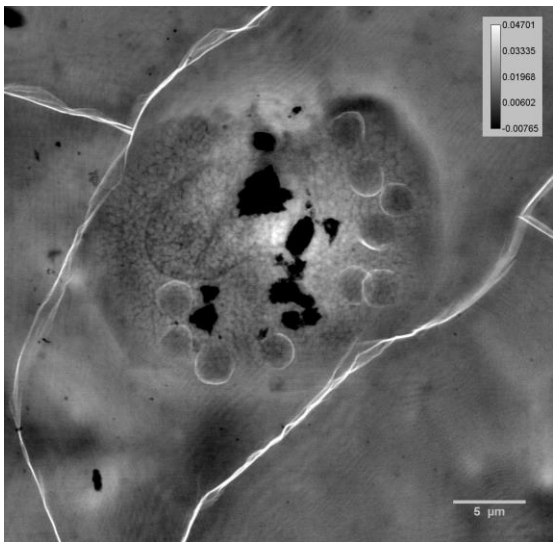

A

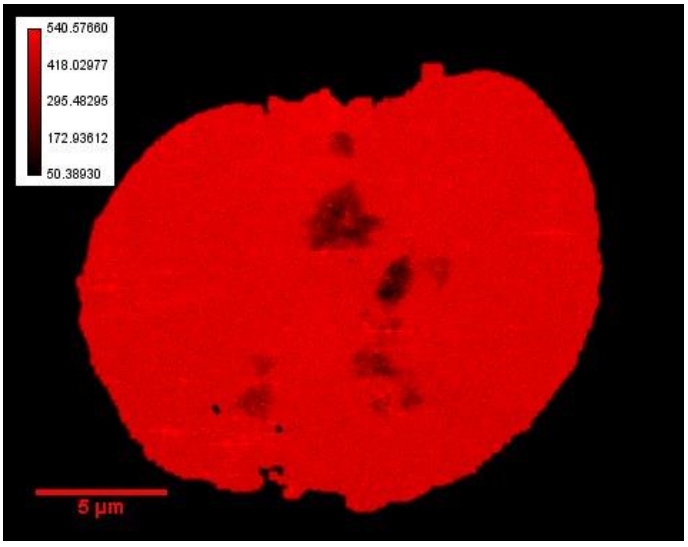

B

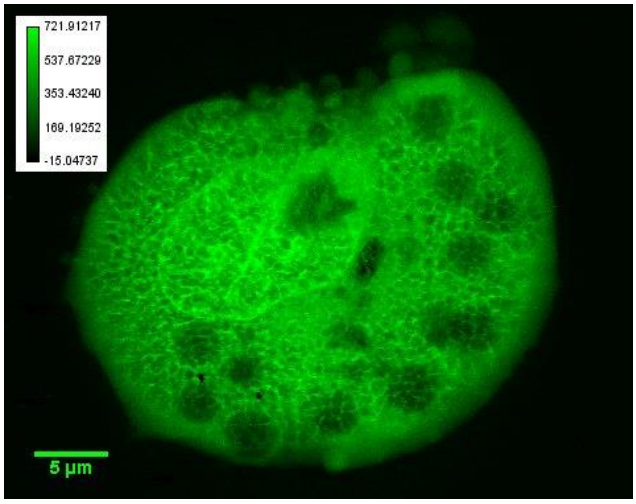

C

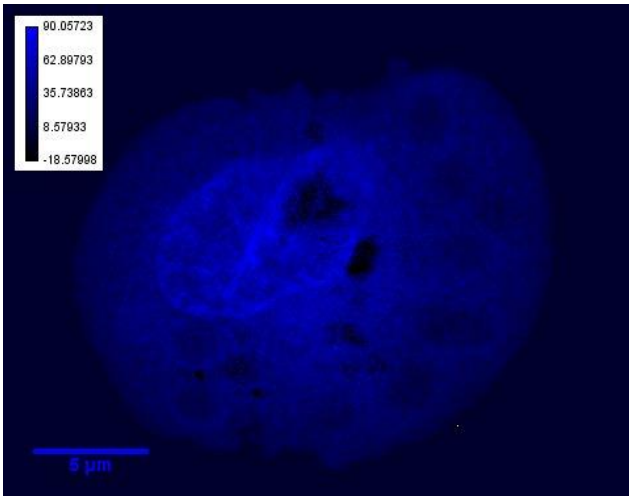

D

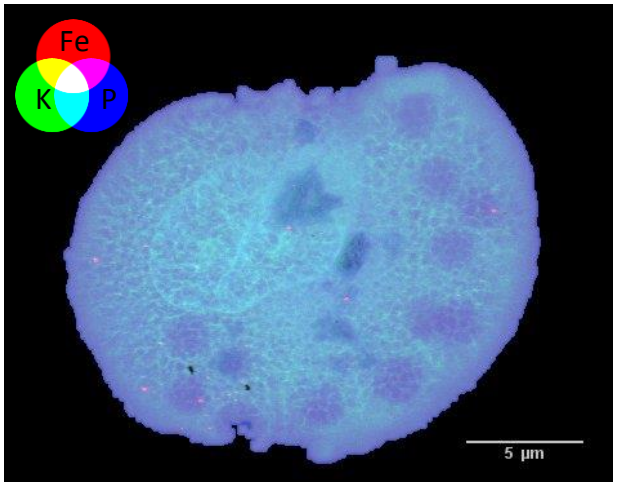

E

8.3: **A** *Phase contrast Map [rad] [30 nm pixelsize]*, **B** *Iron Fluorescence intensity Map [70 nm pixelsize]*, **C** *Potassium Fluorescence intensity Map [70 nm pixelsize]*, **D** *Phosphorus Fluorescence intensity Ma [70 nm pixelsize]*, **E** *Fluorescence intensity Composite Map of Phosphorus, Potassium and Iron [70 nm pixelsize]*.

CTRL 202 CELL 2

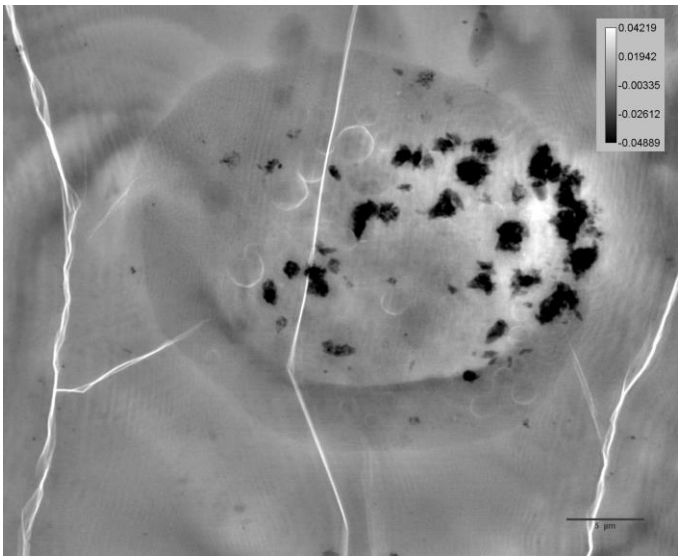

A

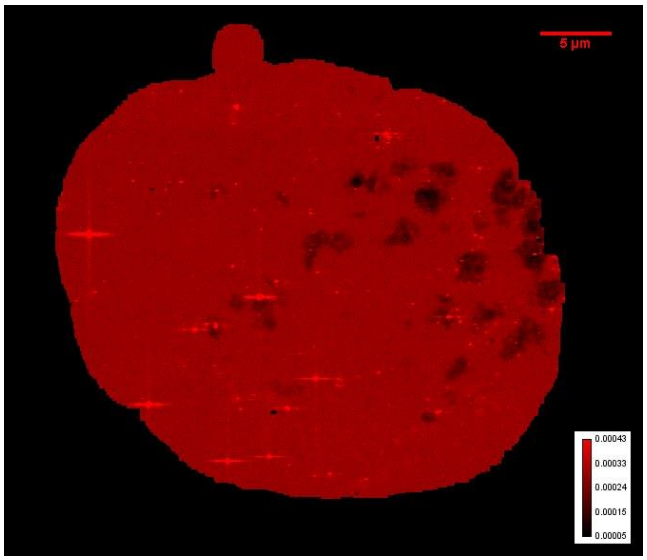

B

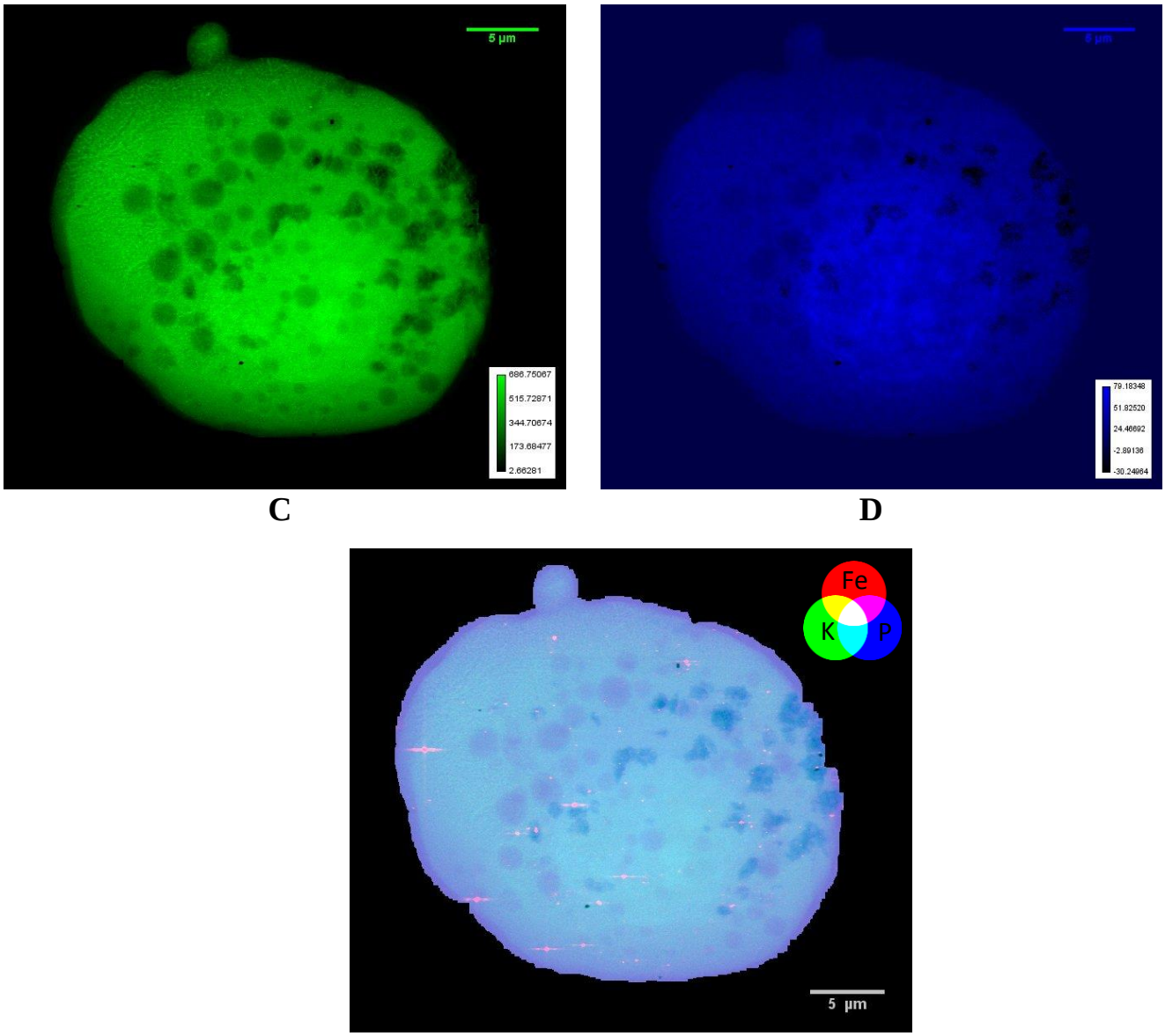

C **D**

E

8.4: **A** *Phase contrast Map [rad] [30 nm pixelsize]*, **B** *Iron Fluorescence intensity Map [70 nm pixelsize]*, **C** *Potassium Fluorescence intensity Map [70 nm pixelsize]*, **D** *Phosphorus Fluorescence intensity Ma [70 nm pixelsize]*, **E** *Fluorescence intensity Composite Map of Phosphorus, Potassium and Iron [70 nm pixelsize]*.

SAMPLE 106 CELL 1 TREATED WITH LF AND LPS

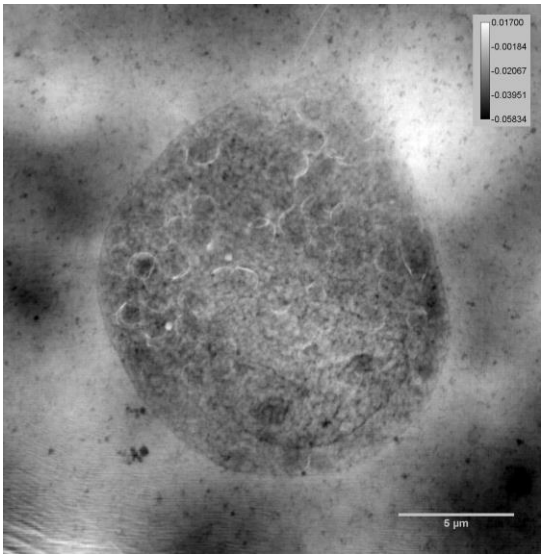

A

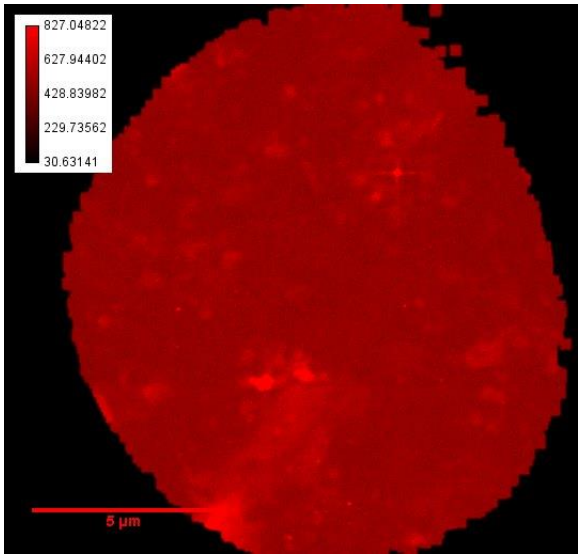

B

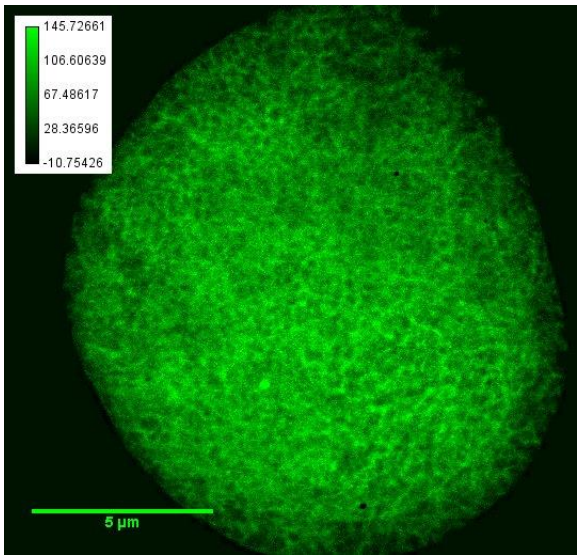

C

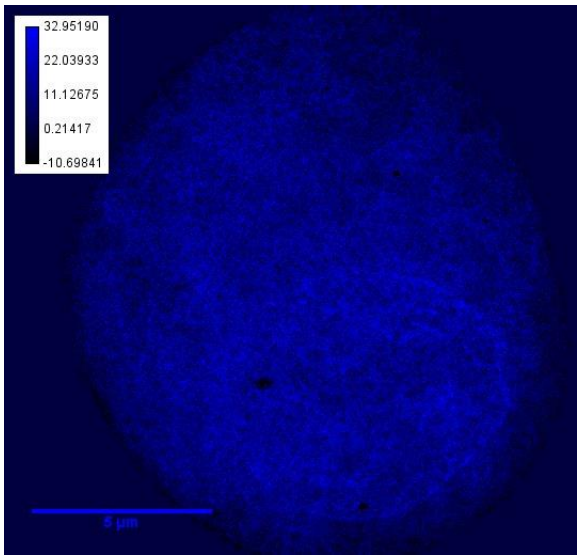

D

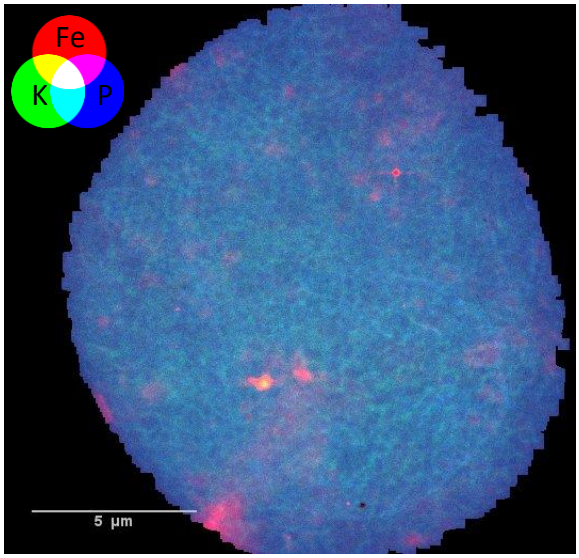

E

***Figure 8.5**: **A** Phase contrast Map [rad] [25 nm pixelsize], **B** Iron Fluorescence intensity Map [50 nm pixelsize], **C** Potassium Fluorescence intensity Map [50 nm pixelsize], **D** Phosphorus Fluorescence intensity Ma [50 nm pixelsize], **E** Fluorescence intensity Composite Map of Phosphorus, Potassium and Iron [50 nm pixelsize].*

SAMPLE 106 CELL 2 TREATED WITH LF AND LPS

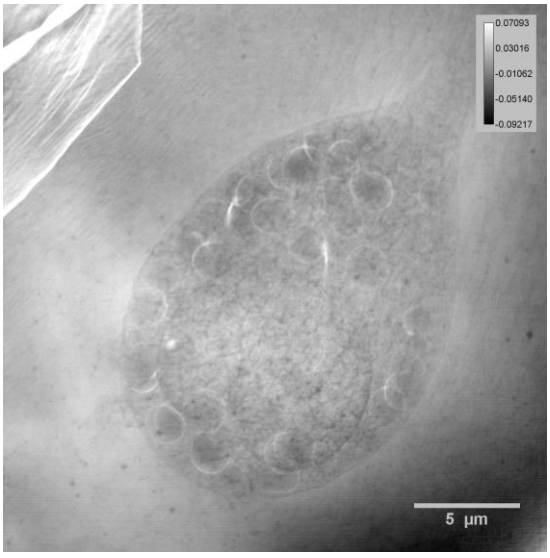

A

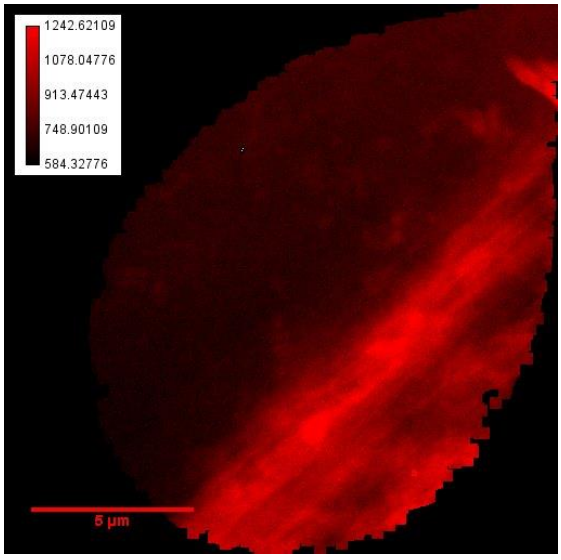

B

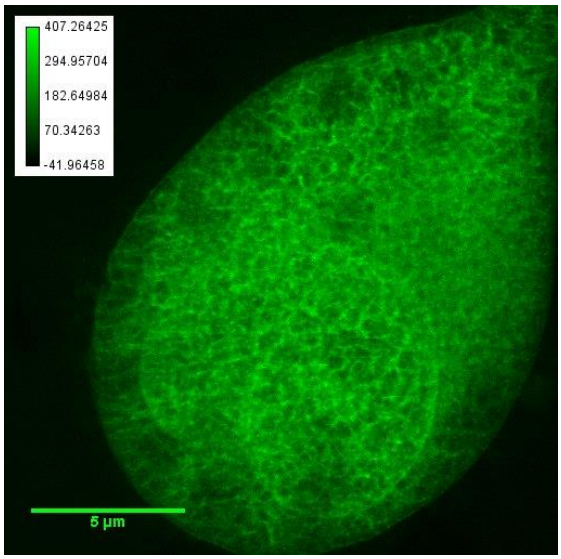

C

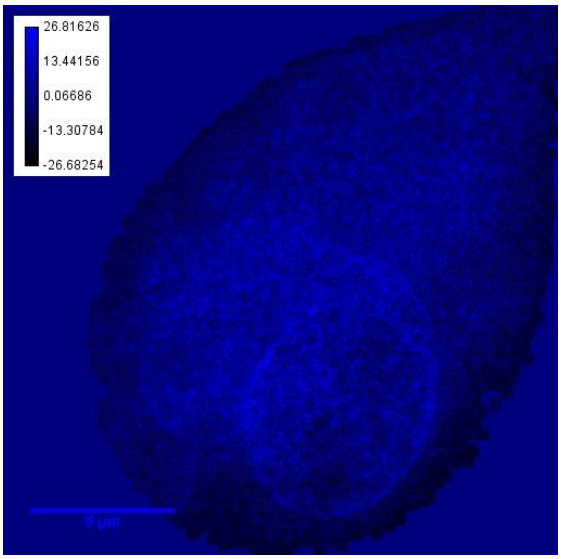

D

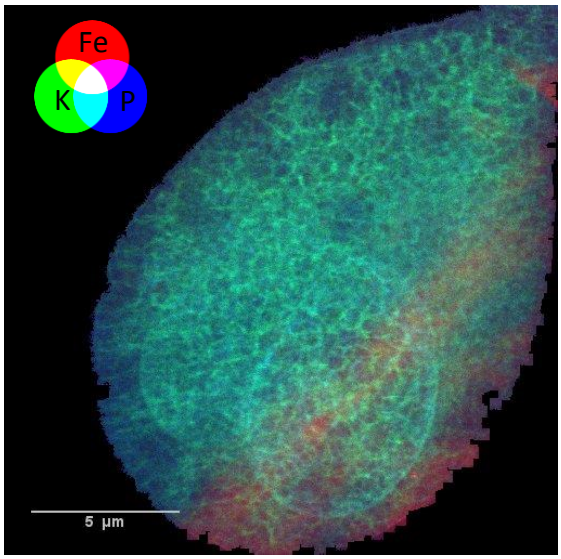

E

Figure 8.6*: Phase contrast Map [rad] [25 nm pixelsize],* **B** *Iron Fluorescence intensity Map [50 nm pixelsize],* **C** *Potassium Fluorescence intensity Map [50 nm pixelsize],* **D** *Phosphorus Fluorescence intensity Ma [50 nm pixelsize],* **E** *Fluorescence intensity Composite Map of Phosphorus, Potassium and Iron [50 nm pixelsize].*

SAMPLE 108 CELL 1 TREATED WITH LF

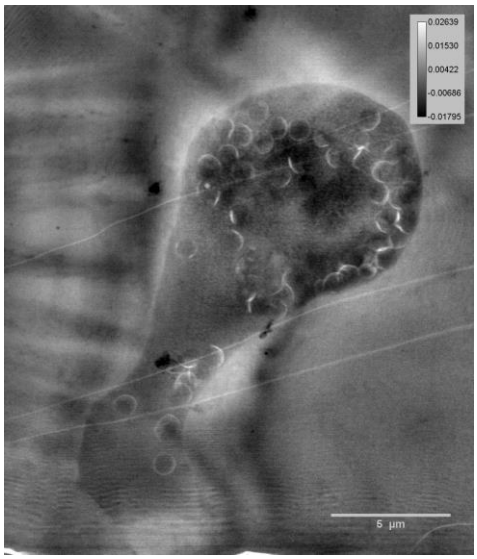

A

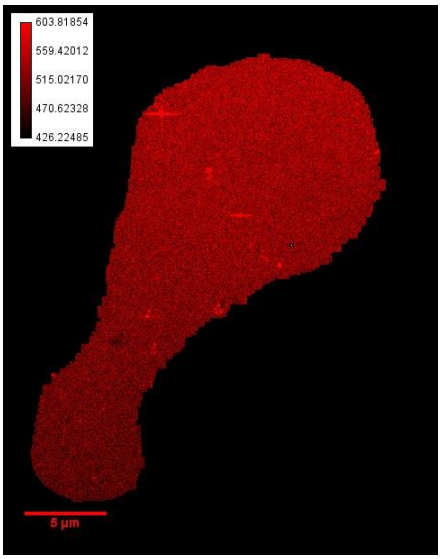

B

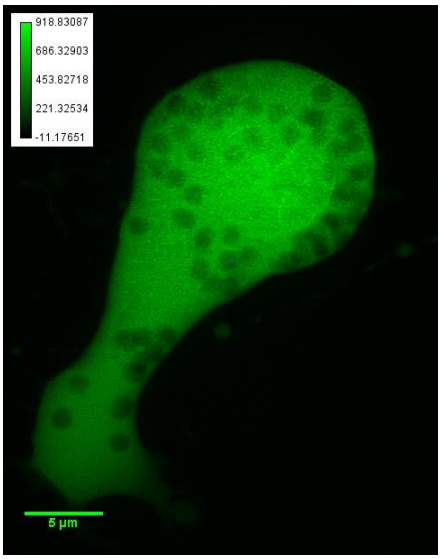

C

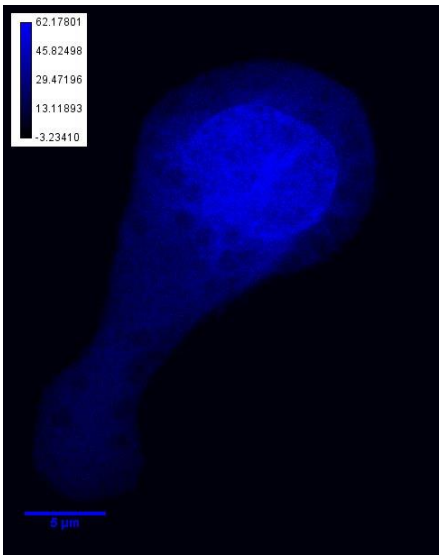

D

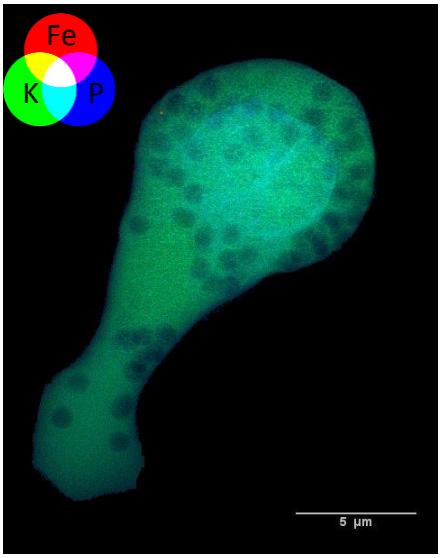

E

Figure 8.7: *Phase contrast Map [rad] [30 nm pixelsize],* **B** *Iron Fluorescence intensity Map [70 nm pixelsize],* **C** *Potassium Fluorescence intensity Map [70 nm pixelsize],* **D** *Phosphorus Fluorescence intensity Ma [70 nm pixelsize],* **E** *Fluorescence intensity Composite Map of Phosphorus, Potassium and Iron [70 nm pixelsize].*

SAMPLE 106 CELL 3 TREATED WITH LF AND LPS

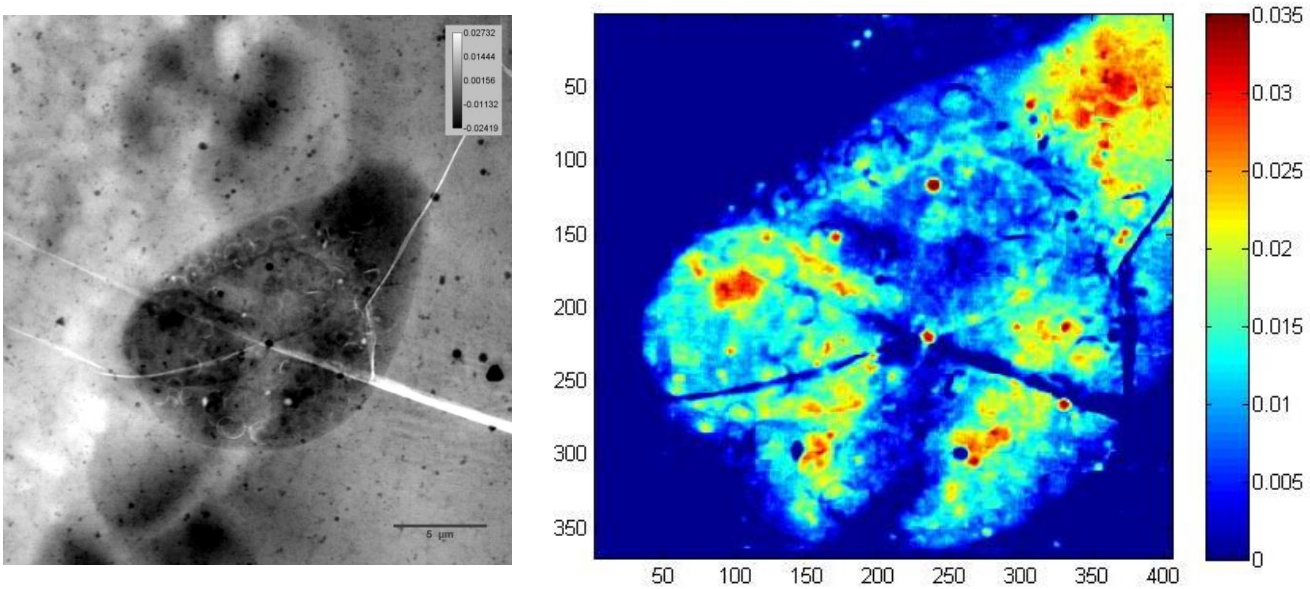

A

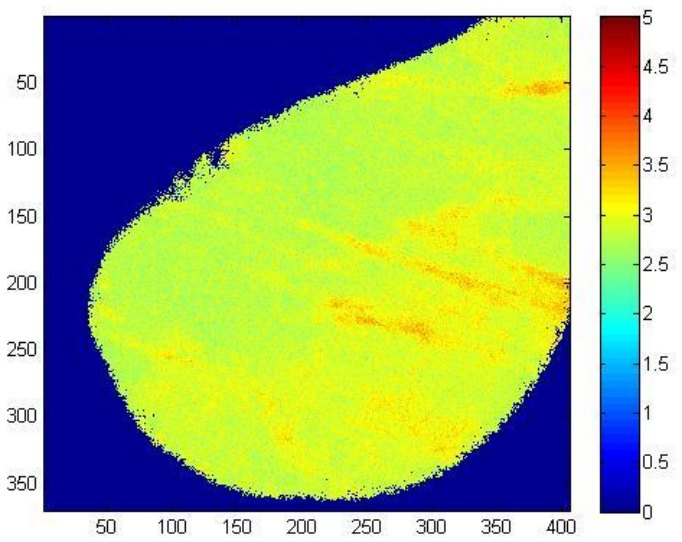
50
100
150
200
250
300
350
50 100 150 200 250 300 350 400
5
4.5
4
3.5
3
2.5
2
1.5
1
0.5
0

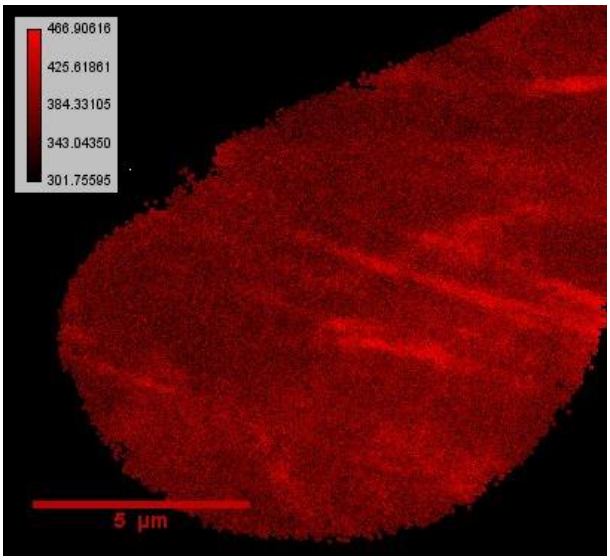
466.90616
425.61861
384.33105
343.04350
301.75595
5 µm

B

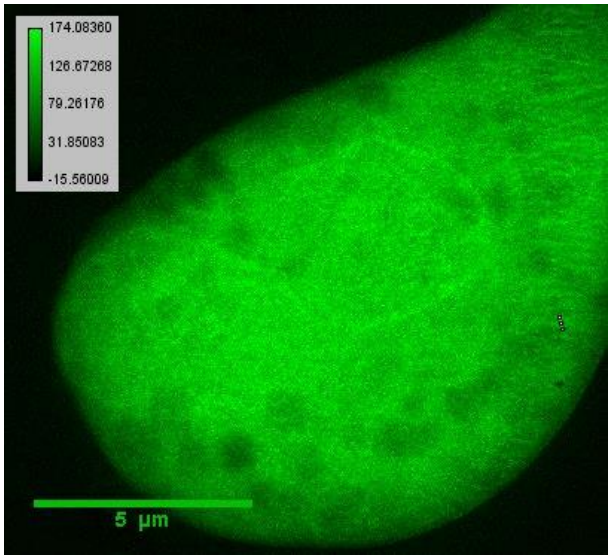
174.08360
126.67268
79.26176
31.85083
-15.56009
5 µm

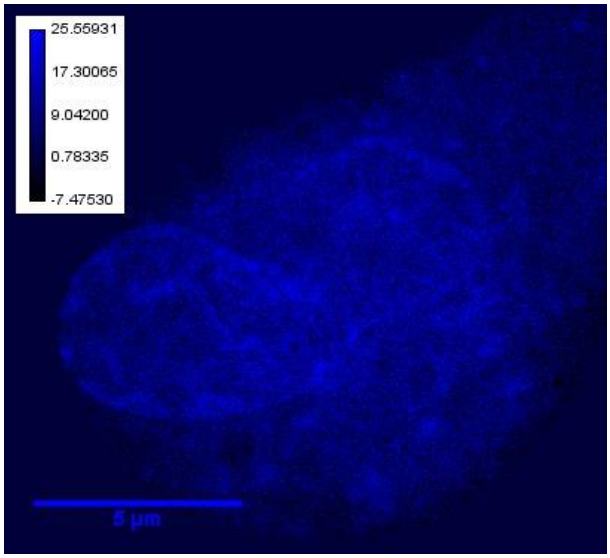
25.55931
17.30065
9.04200
0.78335
-7.47530
5 µm

C **D**

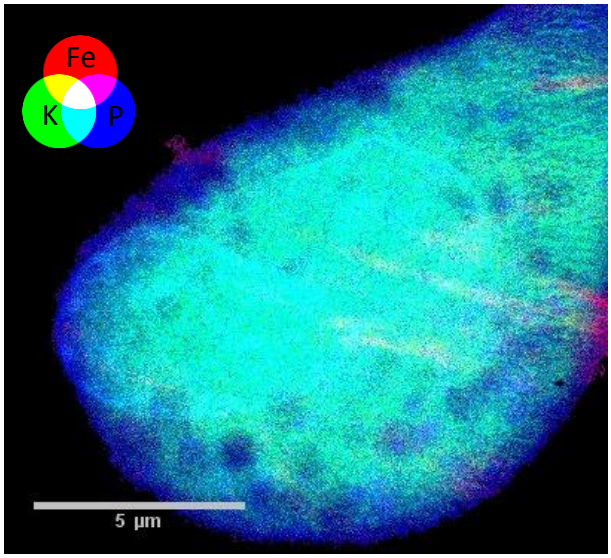

E

***Figure 8.8**: **A** Phase contrast Map [rad] [25nm pixelsize], **B** Iron Fluorescence intensity Map [50 nm pixelsize], **C** Potassium Fluorescence intensity Map [50 nm pixelsize], **D** Phosphorus Fluorescence intensity Map [50 nm pixelsize] **E** Fluorescence intensity Composite Map of Phosphorus, Potassium and Iron [50 nm pixelsize].*

SAMPLE LF CELL 1 TREATED WITH LF

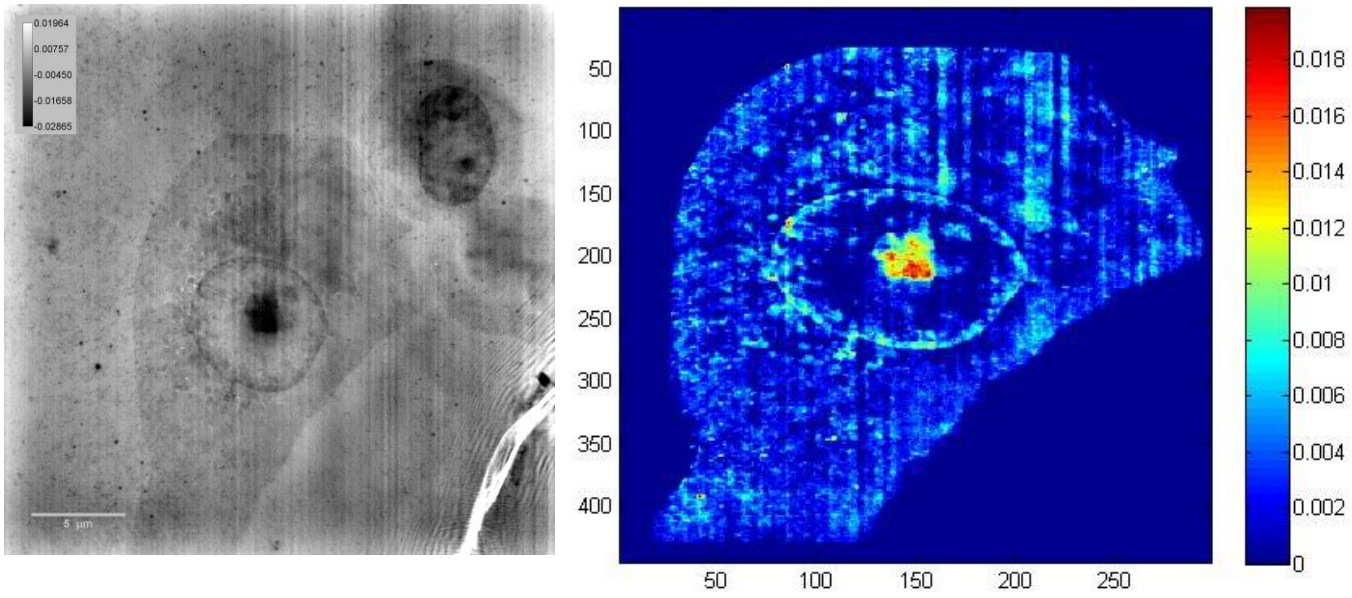

A

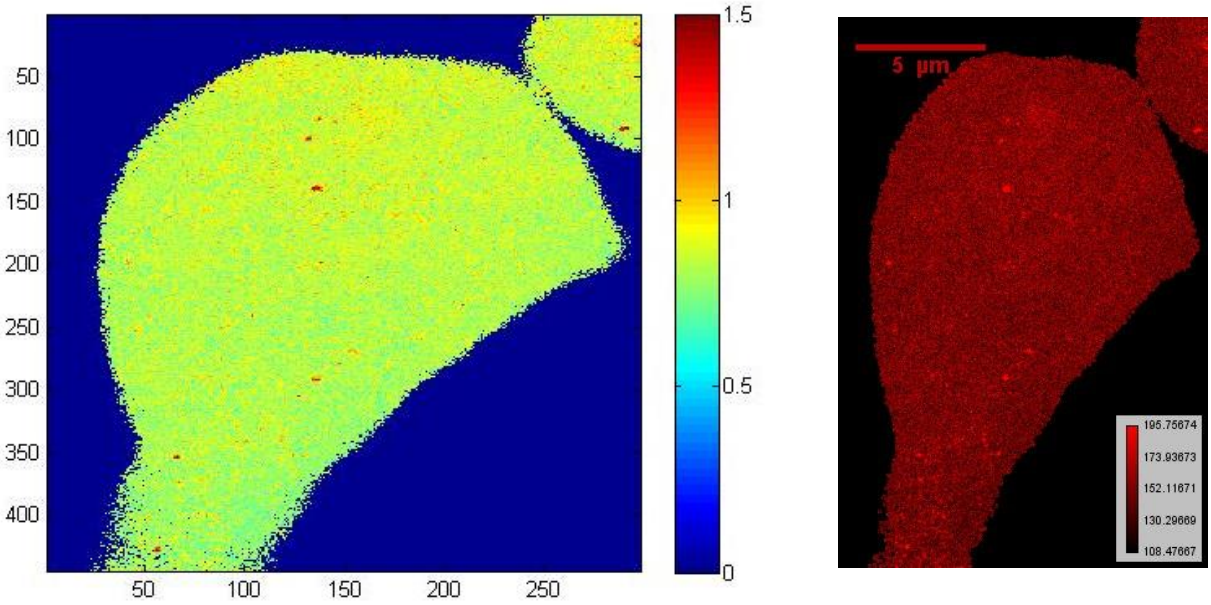

B

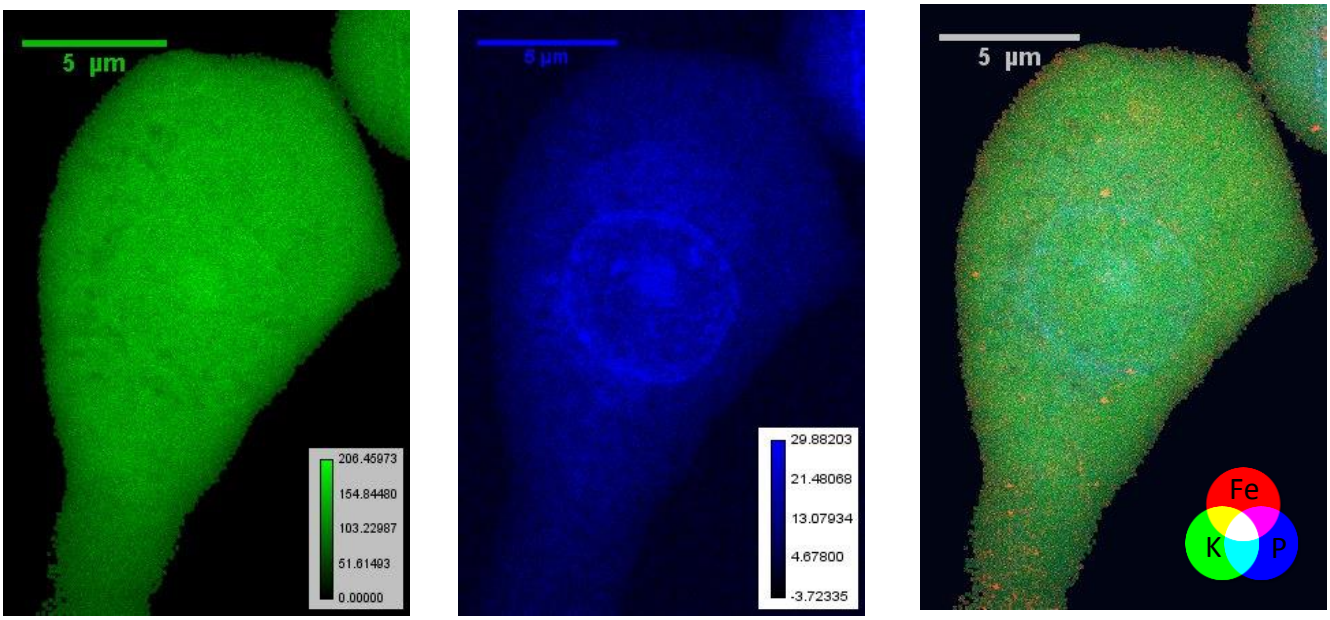

C **D** **E**

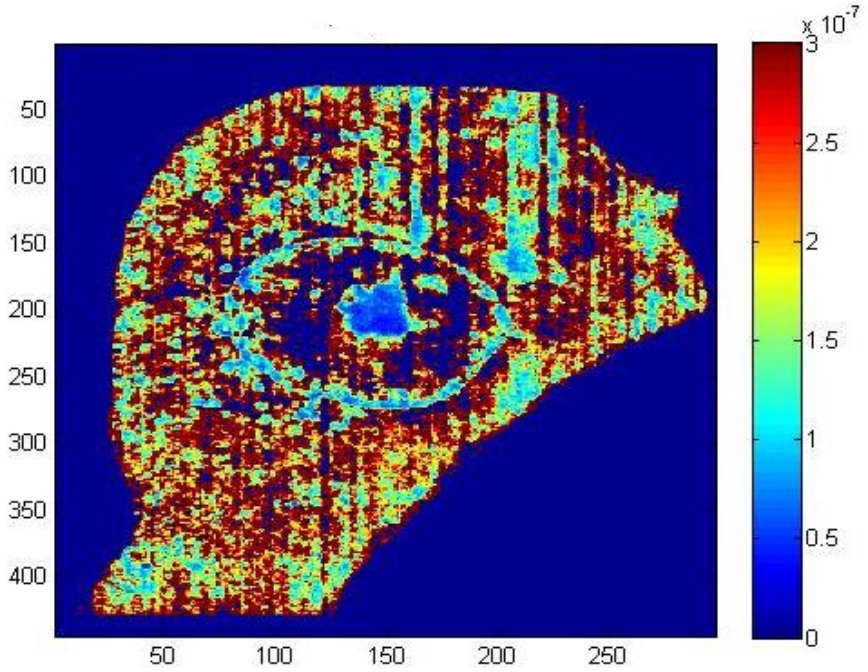

F

***Figure 8.9**: **A** Phase contrast Map [rad] [25 nm pixelsize], **B** Iron Fluorescence intensity Map [50 nm pixelsize], **C** Potassium Fluorescence intensity Map, **D** Phosphorus Fluorescence intensity Ma [50 nm pixelsize] **E** Fluorescence intensity Composite Map of Phosphorus, Potassium and Iron [50 nm pixelsize], **F** Iron Mass Fraction Map.*

SAMPLE LF CELL 2 TREATED WITH LF

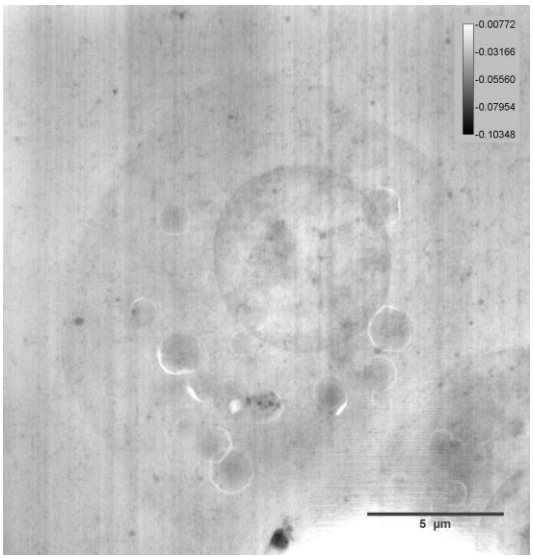

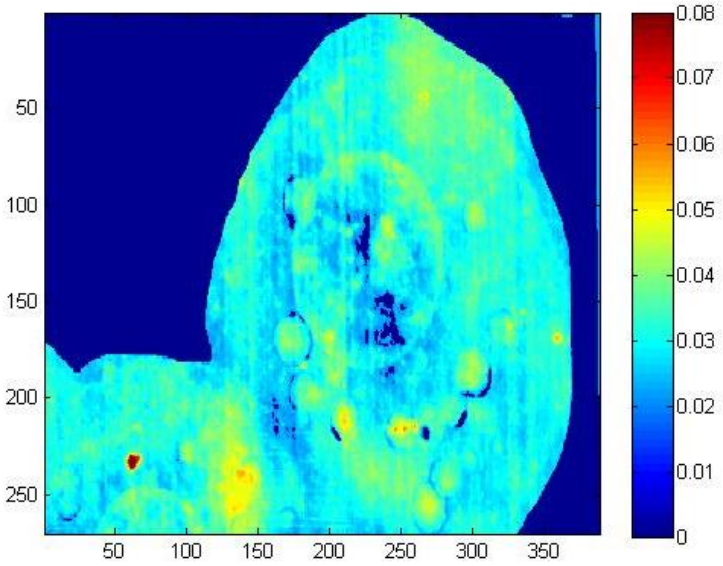

A

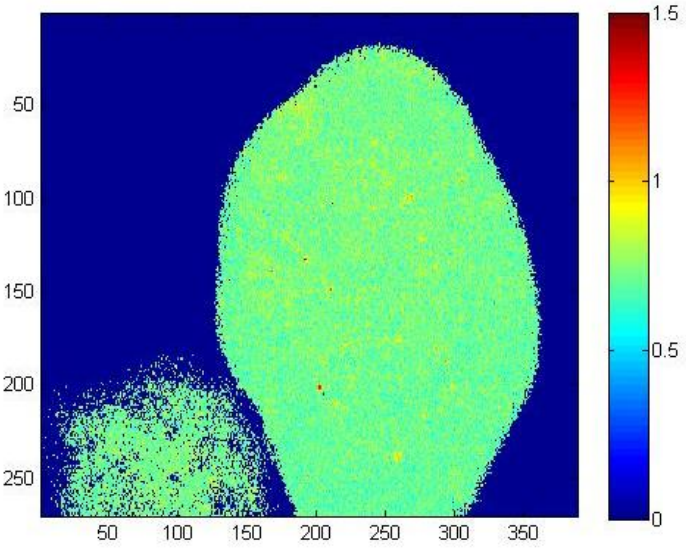

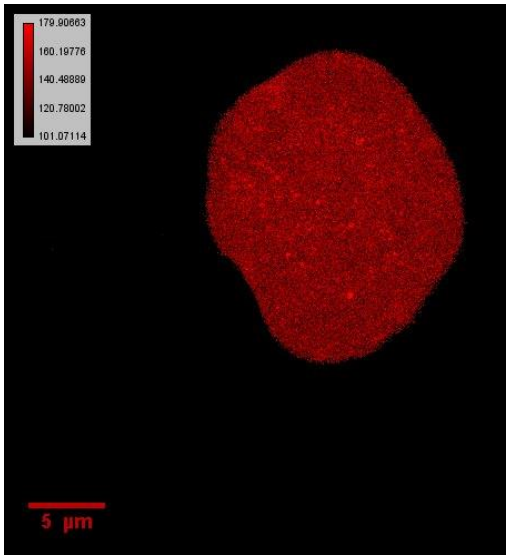

B

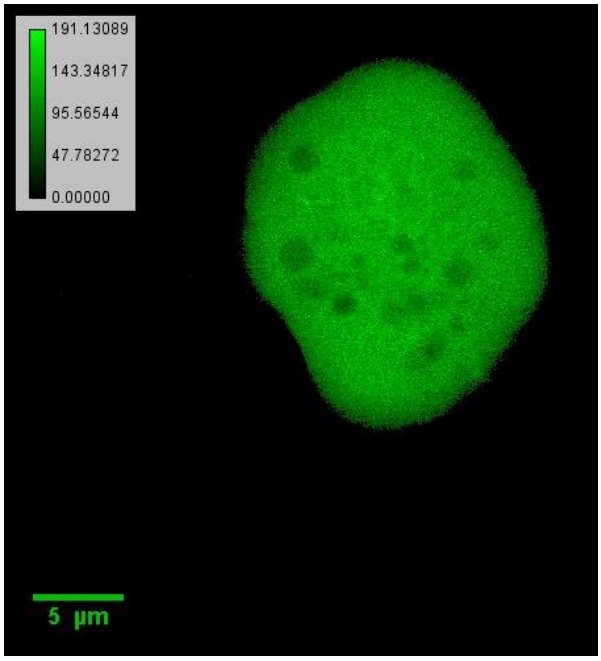

C

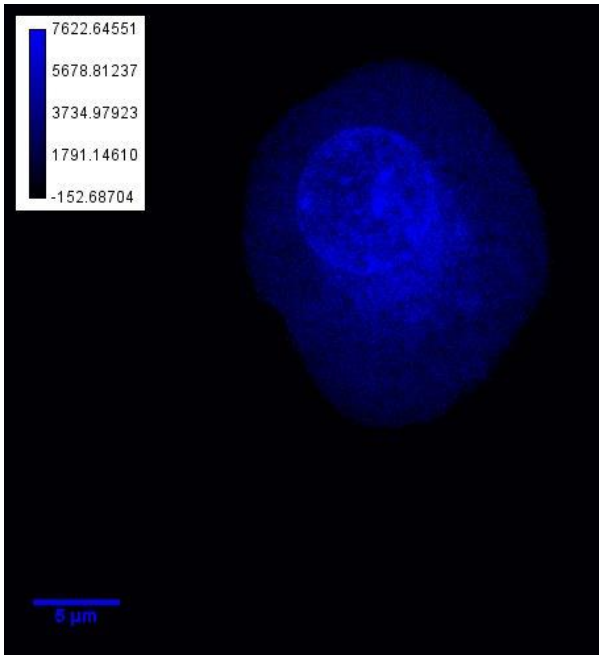

D

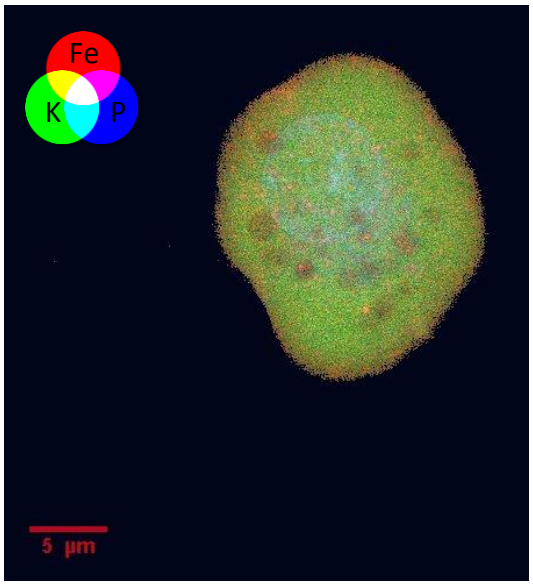

E

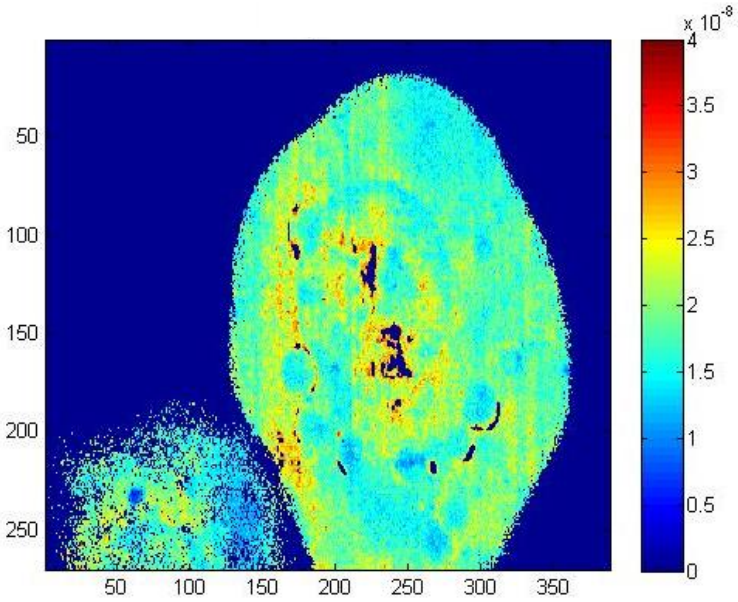

F

Figure 8.10: **A** *Phase contrast Map [rad] [25 nm pixelsize]*, **B** *Iron Fluorescence intensity Map [50 nm pixelsize]*, **C** *Potassium Fluorescence intensity Map [50 nm pixelsize]*, **D** *Phosphorus Fluorescence intensity Ma [50 nm pixelsize]* **E** *Fluorescence intensity Composite Map of Phosphorus, Potassium and Iron [50 nm pixelsize]*, **F** *Iron Mass Fraction Map.*

8.2 Discussion

The analysis and the interpretation of the results on frozen hydrated cells, is not yet complete. Both the iron fluorescence and the phase map suffer for the presence of ice surrounding the cells, which in some cases is cracked. This creates strong black-white fringes in the phase contrast image, and makes the registering procedure between the phase map and the fluorescence quite complex. For the cells that have strong black-white fringes in the phase contrast image, it was assumed a costant density value, in order to calculated the the Iron mass fraction Figures 8.11 **A,** 8.12 **A,** 8.13 **A,** 8.14 **A,** 8.15 **A,** 8.16 **A,** 8.17 **A,** 8.18 **A**. (see eq. 6.15 Chapter 6). Work is in progress to solve these problems. It must be considered that this kind of measurements were the first ones to be carried out at the ID16-A beamline. Nevertheless, we are confident that relevant information can be extracted from these measurements, once the correct procedures for the analysis would be set. On the basis of the Iron, Potassium and Phosphorus fluorescence map for each tipology of cell displayed in Figures 8.1 **B-C-D**, 8.2 **B-C-D**, 8.3 **B-C-D**, 8.4 **B-C-D**, 8.5 **B-C-D**, 8.6 **B-C-D**, 8.7 **B-C-D**, 8.8 **B-C-D**, 8.9 **B-C-D**, 8.10 **B-C-D** and on the basis of Iron, Potassium and Phosphorus mass fraction displayed in Figures 8.9 **F,** 8.10 **F,** 8.11 **A-B-C,** 8.12 **A-B-C,** 8.13 **A-B-C,** 8.14 **A-B-C,** 8.15 **A-B-C,** 8.16 **A-B-C,** 8.17 **A-B-C,** 8.18 **A-B-C** it was obtained the preliminary results showed in Annex2 where it was calculated for each tipology of the cells and for each experiment the weight fraction and the fluorescence count mean; differentiating between the nuocleus and the cytoplasm and the various elements. It was in preparation an article for Biometals special issue for the localization of Iron linked to the pathogenicity of frozen hydrated cells (see List of Publications).

CTRL 78 CELL 6 B

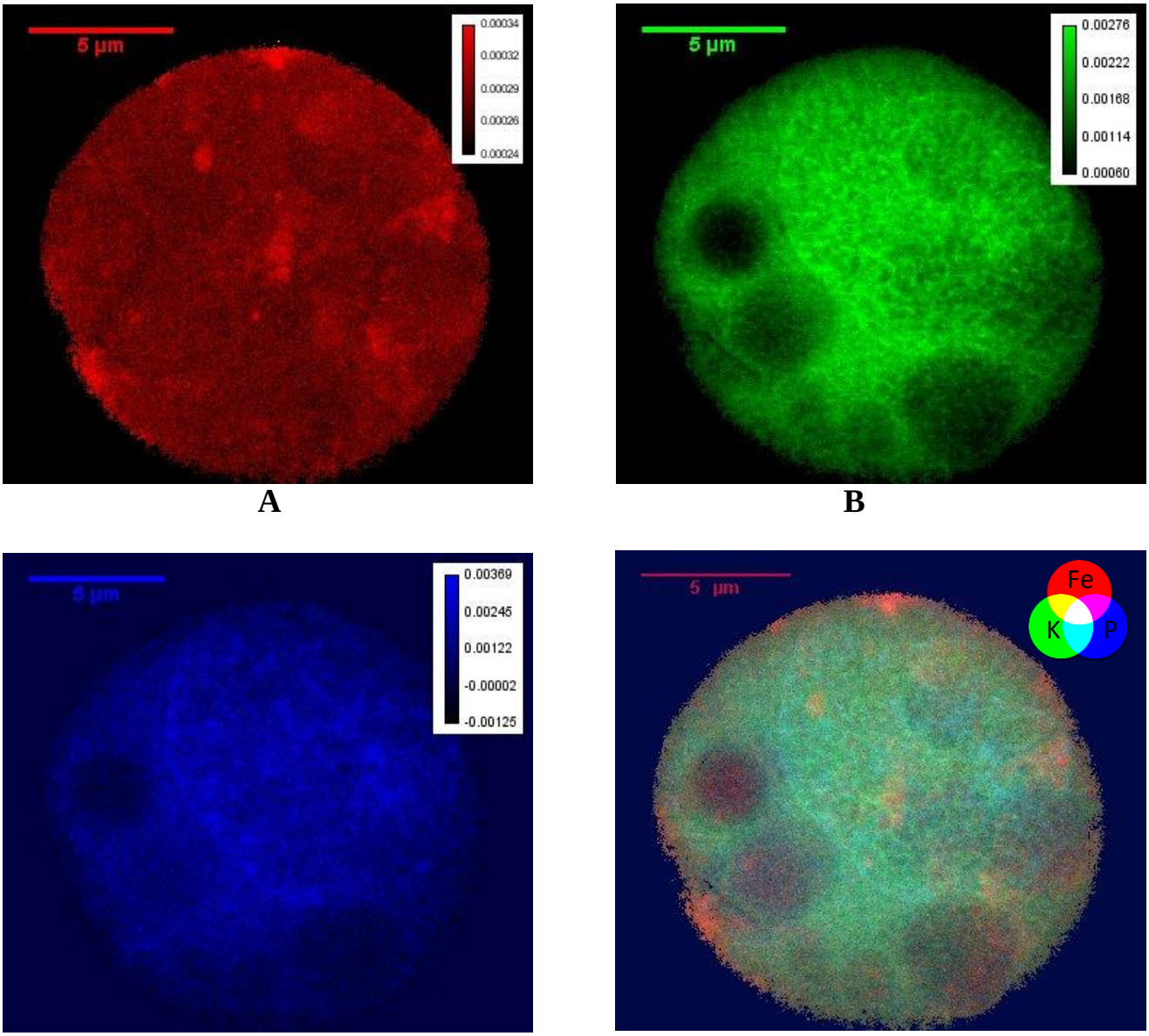

***Figure 8.11**: **A** Iron Mass Fraction Map, **B** Potassium Mass Fraction Map, **C** Phosphorus Mass Fraction Map, **D** Iron Mass Fraction Map Composite Map of Phosphorus, Potassium and Iron.*

CTRL 78 CELL 6 A

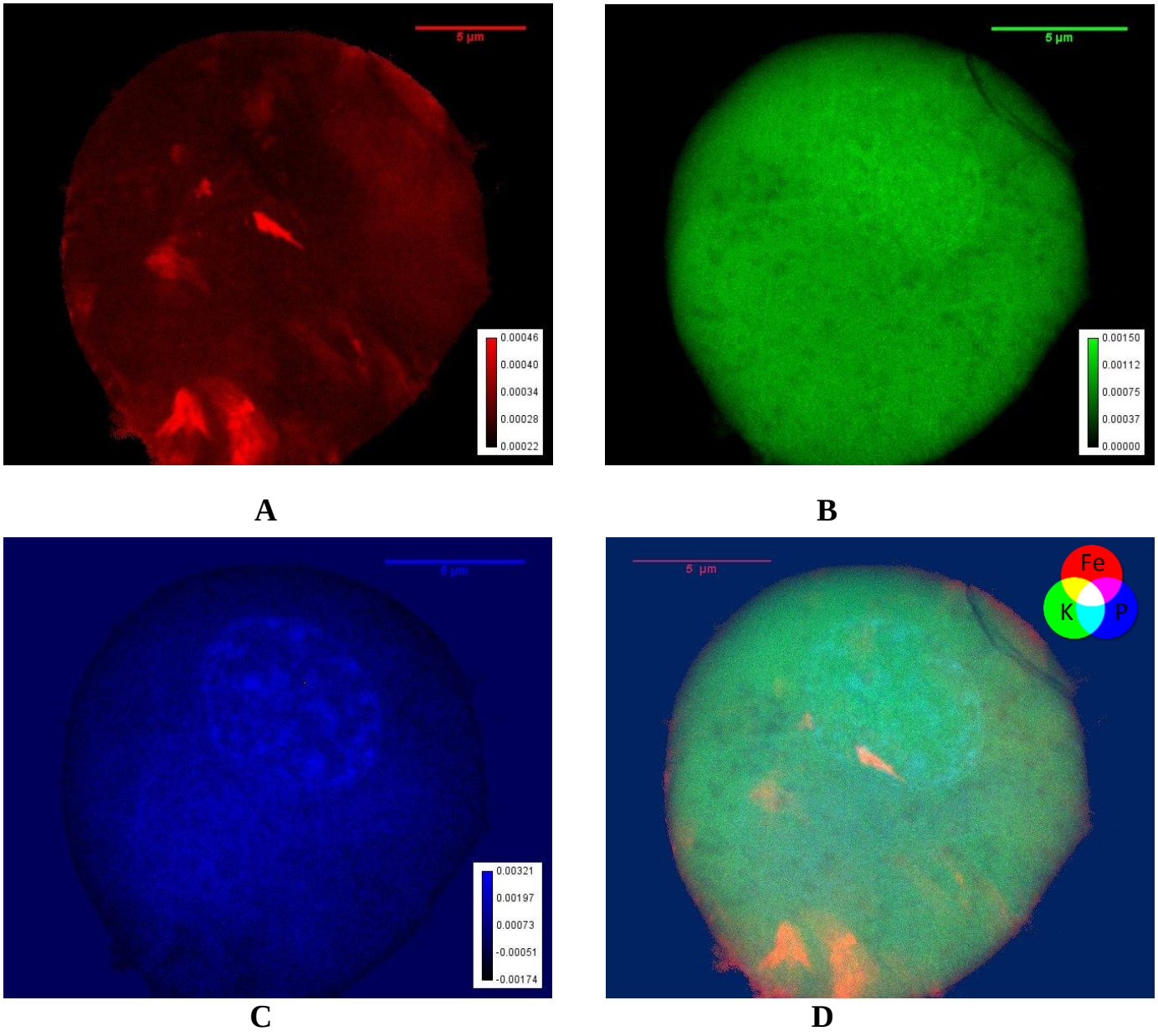

Figure 8.12: **A** *Iron Mass Fraction Map,* **B** *Potassium Mass Fraction Map,* **C** *Phosphorus Mass Fraction Map,* **D** *Iron Mass Fraction Map Composite Map of Phosphorus, Potassium and Iron.*

CTRL 202 CELL 1

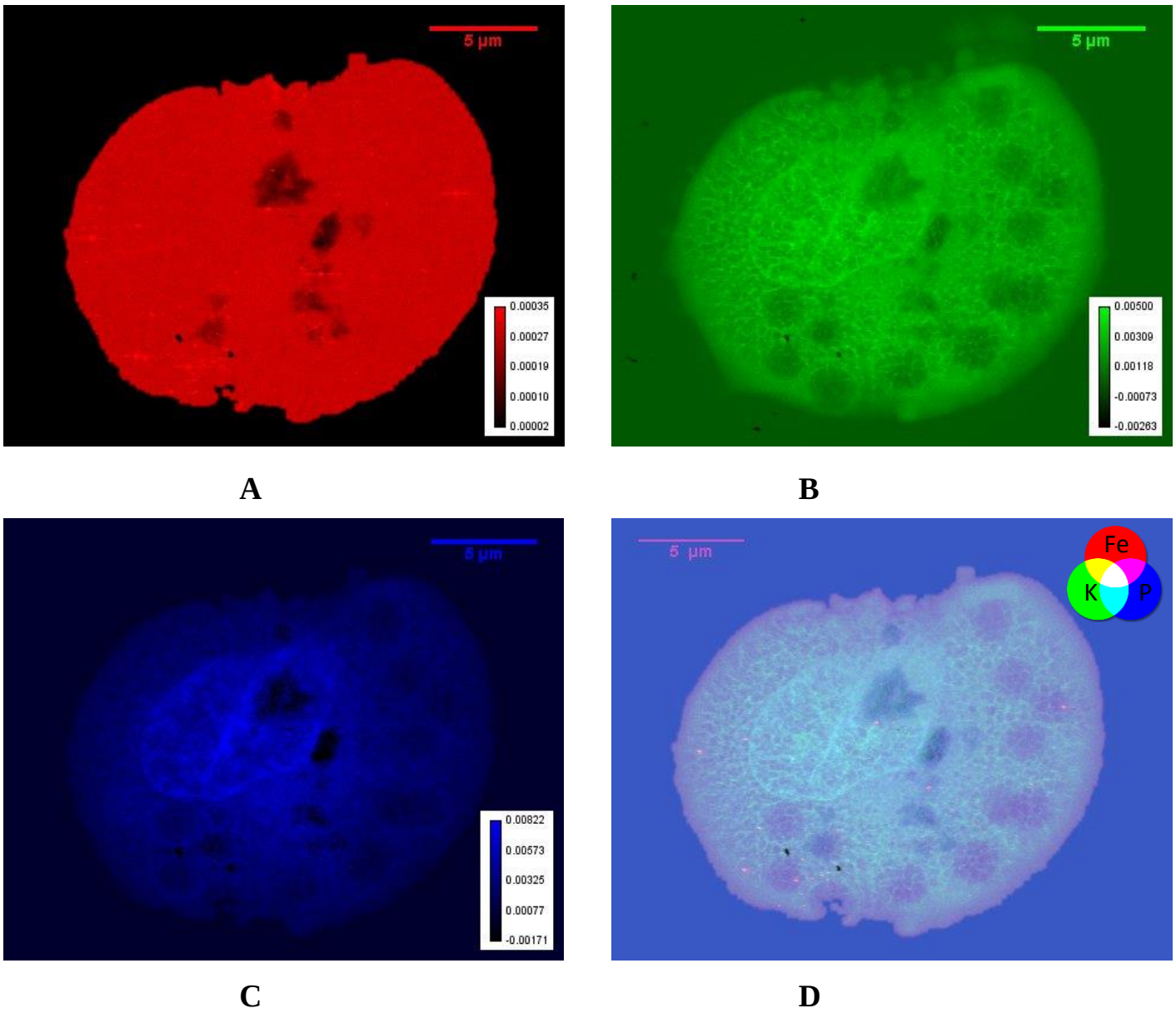

Figure 8.13: **A** *Iron Mass Fraction Map,* **B** *Potassium Mass Fraction Map,* **C** *Phosphorus Mass Fraction Map,* **D** *Iron Mass Fraction Map Composite Map of Phosphorus, Potassium and Iron.*

CTRL 202 CELL 2

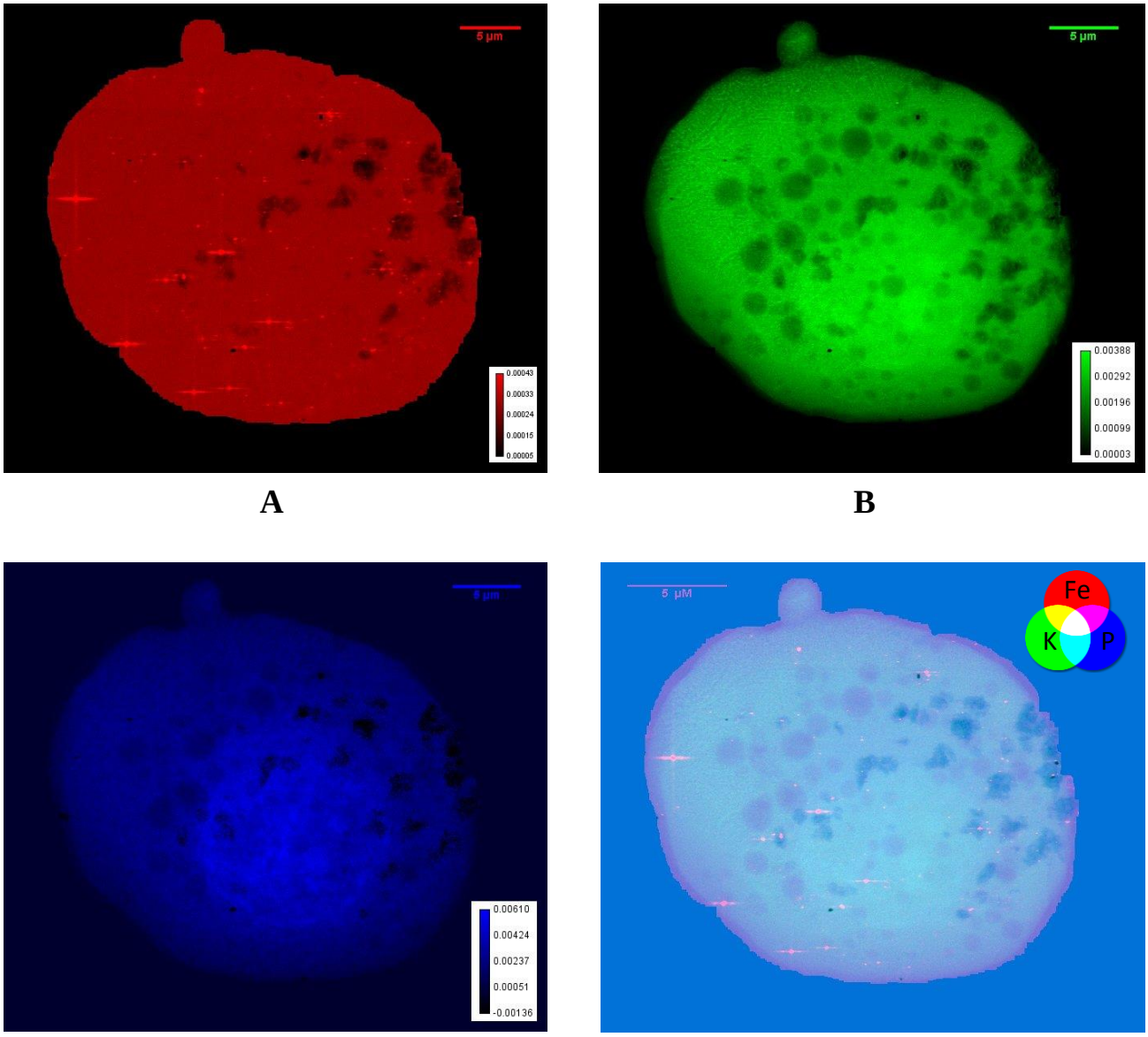

Figure 8.14: **A** *Iron Mass Fraction Map,* **B** *Potassium Mass Fraction Map,* **C** *Phosphorus Mass Fraction Map,* **D** *Iron Mass Fraction Map Composite Map of Phosphorus, Potassium and Iron.*

SAMPLE 106 CELL 1 TREATED WITH LF AND LPS

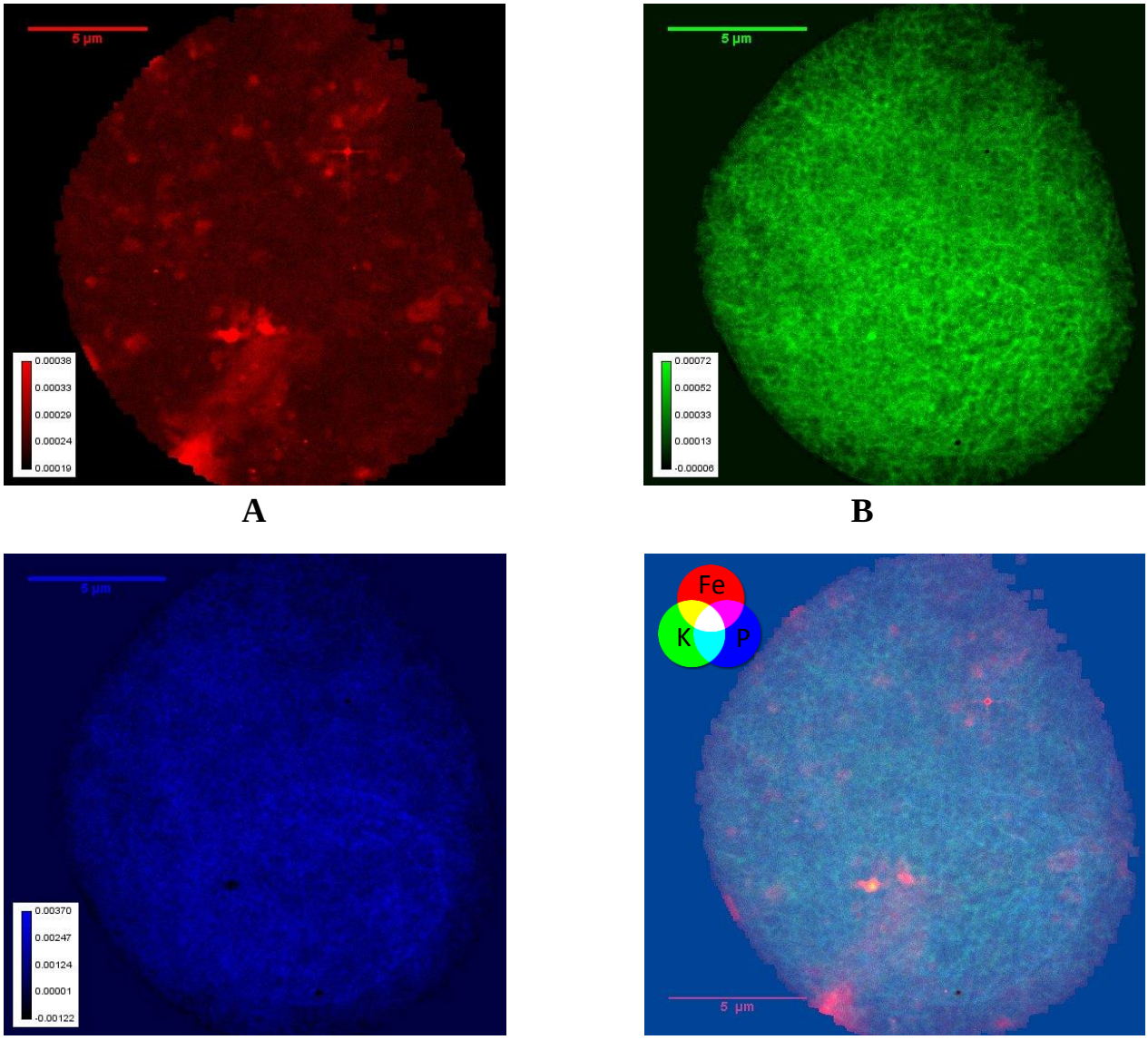

***Figure 8.15**: **A** Iron Mass Fraction Map, **B** Potassium Mass Fraction Map, **C** Phosphorus Mass Fraction Map, **D** Iron Mass Fraction Map Composite Map of Phosphorus, Potassium and Iron.*

SAMPLE 106 CELL 2 TREATED WITH LF AND LPS

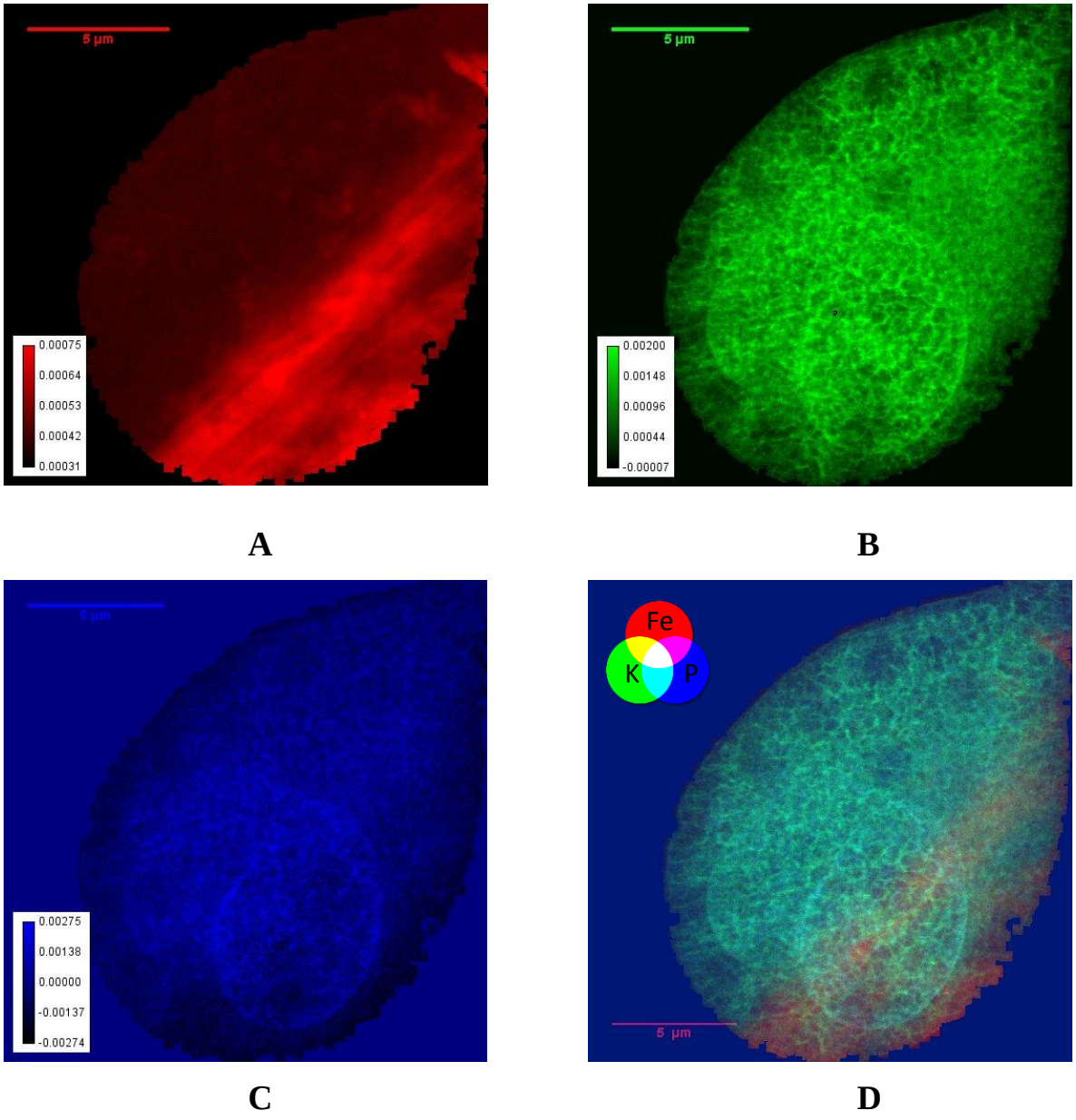

***Figure 8.16**: **A** Iron Mass Fraction Map, **B** Potassium Mass Fraction Map, **C** Phosphorus Mass Fraction Map, **D** Iron Mass Fraction Map Composite Map of Phosphorus, Potassium and Iron.*

SAMPLE 108 CELL 1 TREATED WITH LF

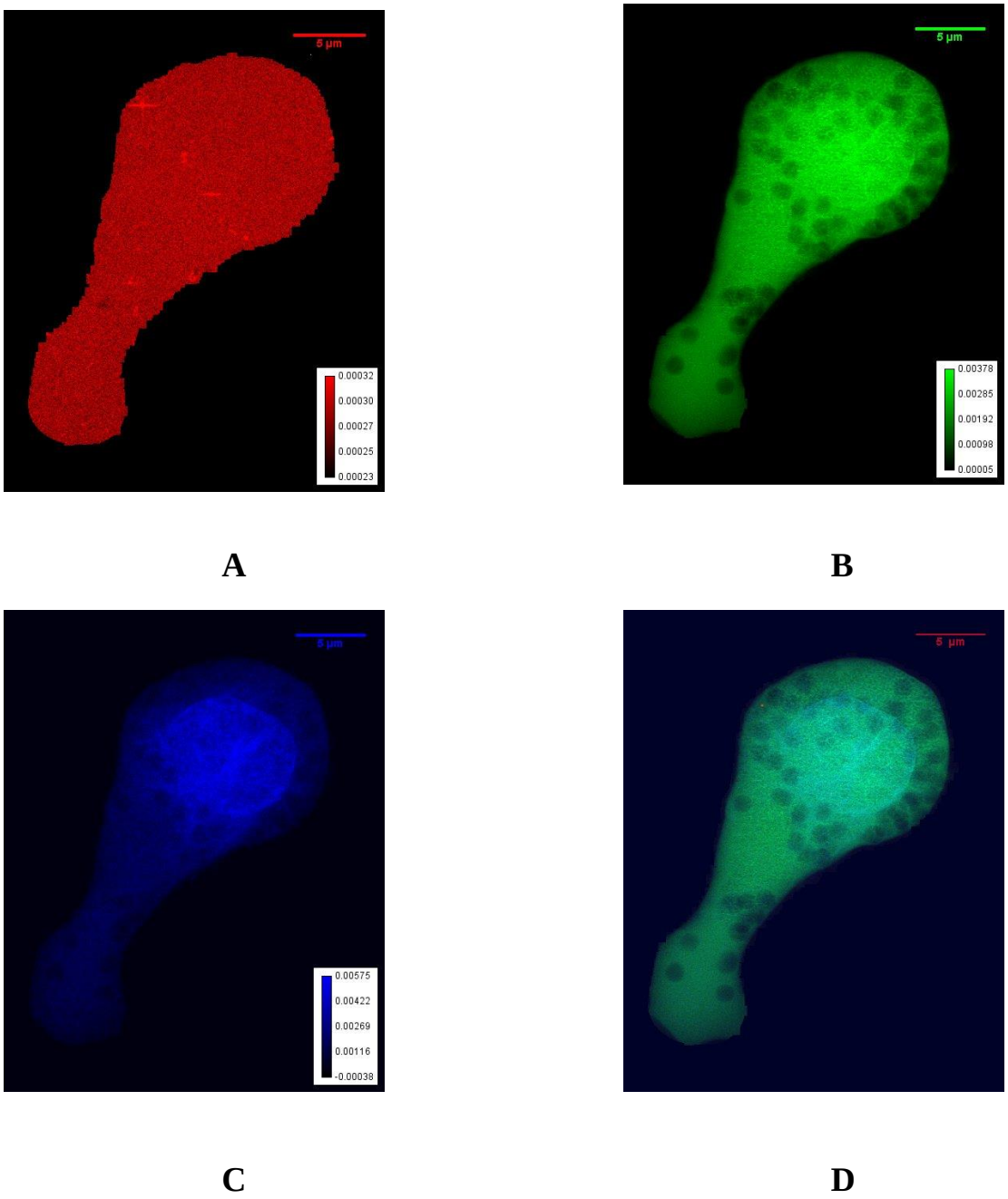

***Figure 8.17**:* **A** *Iron Mass Fraction Map,* **B** *Potassium Mass Fraction Map,* **C** *Phosphorus Mass Fraction Map,* **D** *Iron Mass Fraction Map Composite Map of Phosphorus, Potassium and Iron.*

SAMPLE 106 CELL 3 TREATED WITH LF AND LPS

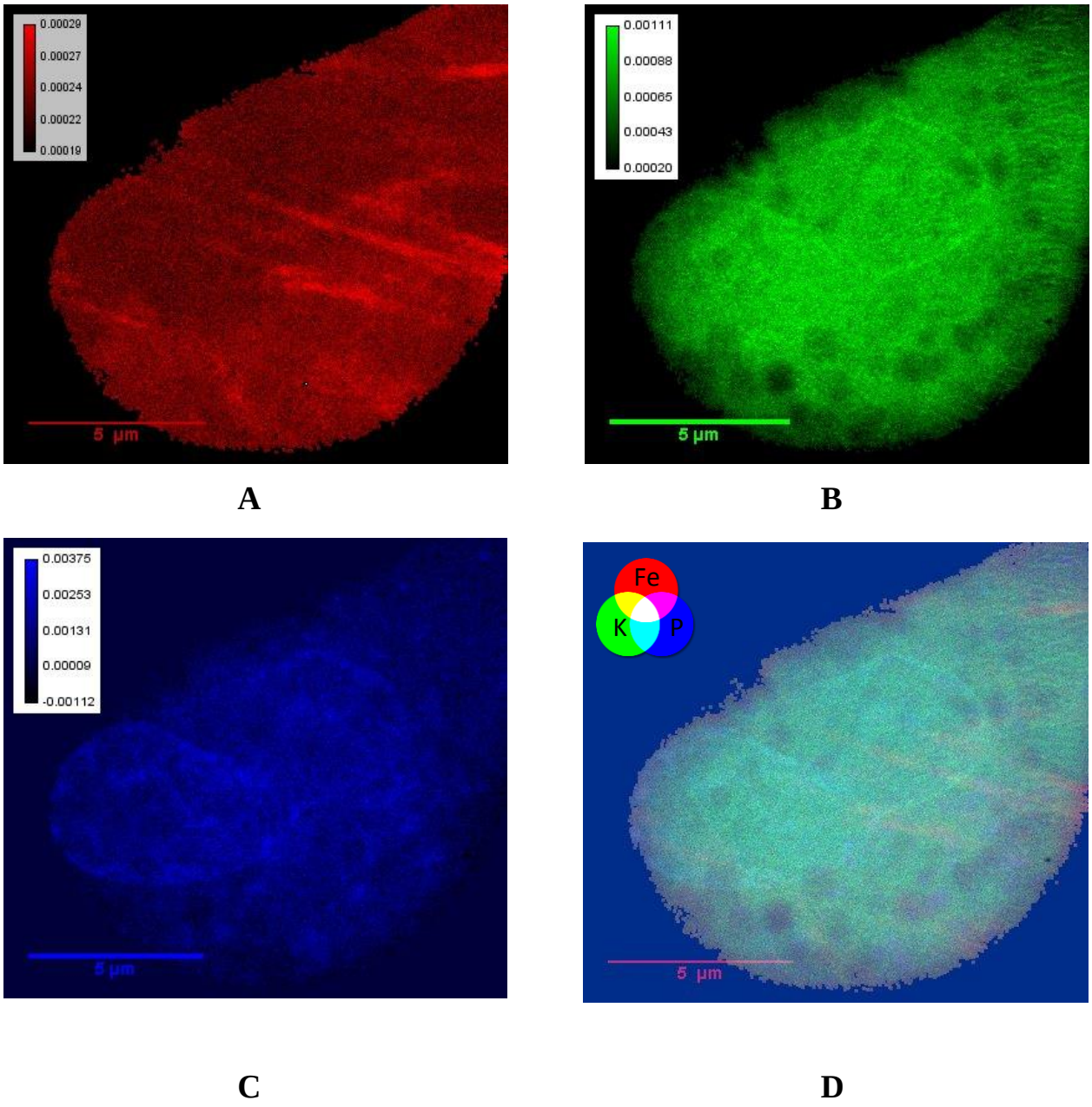

***Figure 8.18**: **A** Iron Mass Fraction Map, **B** Potassium Mass Fraction Map, **C** Phosphorus Mass Fraction Map, **D** Iron Mass Fraction Map Composite Map of Phosphorus, Potassium and Iron.*

Riassunto del Capitolo 8 in Italiano

In questo capitolo sono presentati i risultati dell'analisi fatta sulle cellule frozen hydrated. In particolare sono presentate le mappe di Phase contrast imaging 2D, e di fluorescenza da cui si sono poi ottenute le amppe di mass fraction.

Chapter 9

MAIN CONCLUSIONS AND FUTURE PERSPECTIVES

9.1 Conclusion

This work presents some recent developments in the field of X-ray Fluorescence Tomography and hard X-ray imaging applied to biomedical research. It has been shown that the ID16A beamline of the ESRF can serve as a proper experimental setup to investigate different aspects of cellular research. Three synchrotron-based techniques: X-ray Fuorescence Microscopy (XRFM), phase contrast imaging in 2D and holo-nanotomography were used in this research project together with a non-synchrotron technique, the Atomic Force Microscopy (AFM). With these techniques, we studied inflamed macrophage cells treated or not with Lactoferrin, an iron chelating glycoprotein of natural immunity, in order to quantitatively determine the intracellular iron concentration and its modifications for the different cell conditions. Both freeze-dried and frozen hydrated cells were examined.

This work was innovative, and therefore very challenging, for a number of reasons. We pointed for a very high spatial resolution (100 nm for fluorescence microscopy, 50 nm for 2D phase contrast imaging and holo-nanotomography), and we pointed for quantitative results. Often only very nice images of cells or fluorescence maps at high spatial resolution are presented, but without quantitative assessment of relevant physico-chemical quantities. In our case, instead, concentration and/or mass fraction determination requires accurate data analysis and registration of the fluorescence maps with imaging. In this thesis, we present also for the first time the attempt to normalize a fluorescence map with the quantitative analysis of a holo-nanotomography. As explained in chapter 6, we extracted from the tomography in phase contrast the cell thickness, obtaining in this way a concentration map without the help of Atomic Force Microscopy measurements. It must be noted that this result has been obtained on freeze-dried cells, which are very thin (thickness of the order of 1 μm), with a ratio between thickness and width of the order of 1:20. This obviously makes the tomography quantitative analysis quite complex.

Another novelty regards the application of phase contrast imaging and holo-nanotomography to frozen hydrated cells. Our experiment was the first one of this type carried out at the beamline ID16NI, with the new installation of a cryogenic system.

This work therefore represents a pioneering attempt, both in conception and in practical realization, for quantitative studies of composition and morphology of cells at nanoscale spatial resolution. It is clear that several aspects must be improved. First of all, in the experiment on frozen hydrated cells, some mechanical failure hindered us to perform tomography measurements. Therefore only 2D imaging could be performed. However, also the phase analysis of the 2D imaging revealed quite difficult, and as a consequence also the registration procedure with the fluorescence, probably because of some ice which inevitably surrounds the cell, and which in some cases is fractured, creating strong contrast in phase. Other experiments are scheduled soon, which hopefully will add relevant information to the ones already collected. If the value of this work is in part methodological, because we demonstrated for the first time the possibility to apply all these techniques to the same cells for quantitative determination of physico-chemical properties, it represents also a value from the biological point of view. First of all, the intracellular spatial distribution of iron at nanoscale spatial resolution has been determined for the first time. Quantitative concentration has been assessed in a single cell averaging the whole map. This gives indication that the average values are quite similar for the control and for the Lf, LPS, and LPS+Lf treated samples. It appears that Lf does not influence the iron concentration, but its distribution. In particular, Lf restores the iron distribution resembling to that of uninflammed cell. However, further experiments are needed to confirm these results. This study will contribute to deep the knowledge on the host-pathogen relationship and iron homeostasis as well as the Lf role in such relation.

In conclusion, we can affirm that this work has demonstrated the possibility to obtain quantitative information on cell composition and morphology, combining different synchrotron radiation-based techniques. However, work is still to be done to make the procedure robust and reliable. We also done the analysis of X-ray near-field ptychography data not showed in the thesis because the analysis is still in progress. As future perspective, we can think to the fluo-tomo, i.e. the registration of fluorescence map for different sample orientation, as the technique which can give “per se” the maximum of combined information.

RIASSUNTO IN ITALIANO

Questo lavoro presenta alcuni recenti sviluppi nel campo della fluorescenza a raggi X, della Tomografia e dell'imaging 2D, attraverso l'utilizzo dei raggi X duri, applicate alla ricerca biomedica. È stato dimostrato che la linea di luce ID16A di ESRF può servire come un adeguato apparato sperimentale per indagare diversi aspetti della ricerca cellulare. Sono state utilizzate in questo progetto di ricerca, insieme ad una tecnica di laboratorio la microscopia a forza atomica (AFM), tre tecniche di sincrotrone: Fuorescence Microscopy (XRFM), Imaging a contrasto di fase 2D e Holo-nanotomography. Con queste tecniche abbiamo studiato delle cellule macrofaghe infiammate trattate o meno con la proteina della lattoferrina, una glicoproteina chelante del ferro presente nel nostro sistema immunitario, con lo scopo di determinare quantitativamente la concentrazione di ferro intracellulare e le sue variazioni nelle diverse condizioni di studio delle cellule esaminate. Sono state analizzate sia cellule idratate e congelate (frozen hydrated) che cellule liofilizzate (freeze-dried).

Questo lavoro è risultato innovativo e molto impegnativo, per una serie di ragioni. Abbiamo voluto ottenere dei risultati quantitativi con una risoluzione spaziale molto elevata (100 nm per la microscopia a fluorescenza, e 50 nm per l'imaging a contrasto di fase 2D e Holo-nanotomography). Spesso vengono presentate solamente delle belle immagini di cellule o mappe di fluorescenza ad alta risoluzione spaziale, ma senza la valutazione quantitativa delle grandezze chimico-fisiche rilevanti. Nel nostro caso, invece, la concentrazione e / o la determinazione della mass fraction ha richiesto un'accurata analisi dei dati e la registrazione delle mappe di fluorescenza su quelle dell'imaging. In questa tesi, presentiamo anche per la prima volta il tentativo di normalizzare una mappa di fluorescenza con l'analisi quantitativa di un holo-nanotomography. Come spiegato nel capitolo 6, abbiamo estratto dalla tomografia a contrasto di fase lo spessore cellulare, ottenendo in questo modo una mappa di concentrazione senza l'aiuto di misurazioni di microscopia a forza atomica (AFM). Si noti che questo risultato è stato ottenuto su cellule liofilizzate, che sono molto sottili (spessore dell'ordine di 1 μm), con un rapporto tra lo spessore e la larghezza dell'ordine di 1:20. Questo ovviamente rende l'analisi quantitativa della tomografia abbastanza complessa.

Un'altra novità riguarda l'applicazione dell'imaging a contrasto di fase e dell'Holo-nanotomography alle cellule idratate e congelate. Il nostro esperimento è stato il primo di questo tipo effettuato nella linea di luce ID16A a ESRF, con la nuova installazione di un sistema criogenico.

Questo lavoro rappresenta quindi un tentativo pionieristico, sia nella concezione che nella realizzazione pratica, di studi quantitativi di composizione e di morfologia cellulare con una risoluzione spaziale su scala nanometrica. E' chiaro che alcuni aspetti devono essere migliorati. Prima di tutto, l'esperimento su cellule congelate idrate, ha avuto qualche guasto meccanico che ha ostacolato l'esecuzione delle misure di tomografia. Pertanto, è stato possibile eseguire solo immagini di imaging 2D. Tuttavia, anche l'analisi dell'imaging 2D si è rivelata molto difficile, e di conseguenza anche la procedura di registrazione con la fluorescenza, probabilmente a causa del ghiaccio che circondando inevitabilmente la cellula, e in alcuni casi si è fratturato, creando cosi' un forte contrasto di fase. Altri esperimenti sono in programma a breve, e si spera di aggiungere informazioni pertinenti a quelle già raccolte. Se il valore di questo lavoro è in buona parte metodologica, perché abbiamo dimostrato per la prima volta la possibilità di applicare tutte queste tecniche alle stesse cellule per la determinazione quantitativa delle proprietà fisico-chimiche, rappresenta anche un valore dal punto di vista biologico. Infatti la distribuzione spaziale intracellulare di ferro con risoluzione spaziale nanometrica è stato determinata qui per la prima volta. E' stata valutata per ogni cellula la concentrazione media. Confrontando questi valori, per tutti i tipi di campioni trattati, si è visto che i valori medi sono abbastanza simili per il controllo e i campioni trattati con Lf, LPS e LPS + Lf. Sembra che Lf non influenza la concentrazione di ferro, ma la sua distribuzione. In particolare, Lf ripristina la distribuzione naturale del ferro come quella che si ha nelle cellule non infiammate. Tuttavia, sono necessari ulteriori esperimenti per confermare questi risultati. Questo studio contribuirà ad approfondire la conoscenza sull'omeostasi del ferro e sul ruolo che ha in questo la lattoferrina.

In conclusione, possiamo affermare che questo lavoro ha dimostrato la possibilità di ottenere informazioni quantitative sulla composizione e sulla morfologia cellulare, combinando differenti tecniche di radiazione di sincrotrone. Tuttavia, c'è ancora lavoro da fare per rendere la procedura robusta e affidabile. Abbiamo anche fatto un'analisi dei dati di X-ray near-field ptychography non mostrati nella tesi perché l'analisi è ancora in corso. Come prospettiva futura, possiamo pensare alla tecnica di fluo-tomo, vale a dire la registrazione di mappe di fluorescenza per diversi orientamenti del campione, come la tecnica che può dare "di per sé" il massimo di informazioni combinate.

La tesi di Dottorato è impostata nella seguente maniera:

Capitolo 1 descrizione delle caratteristiche della radiazione da sincrotrone, l'interazione dei raggi X con la materia e brevi accenni sull'ottica di focalizzazione dei raggi X.

Capitolo 2 descrizione delle tecniche di Imaging e di fluorescenza basate sulla radiazione da sincrotrone.

Capitolo 3 descrizione della teoria alla base della tecnica AFM.

Capitolo 4 si da una breve descrizione della beamline ID16-A ESRF a Grenoble, dove sono stati svolti gli esperimenti oggetto di studio.

Capitolo 5 in questo capitolo sono descritti i campioni biologici. Murrin cells linea J774A.1 (ATCC® TIB-67™), trattate con lipopolisaccaride (LPS) e con lattoferrina.

Capitolo 6 trattazione dei dati analizzati e della metodologia adotatta per ottenere delle informazioni quantitative attraverso l'utilizzo di tutte le tecniche descritte ne lprecedente capitolo 2.

Capitolo 7 descrizione dei risultati ottenuti sulle cellule macrofaghe freeze dried.

Capitolo 8 descrizione dei risultati ottenuti sulle cellule macrofaghe frozen hydrated.

Capitolo 9 riassunto della ricerca e prospettive.

Annex

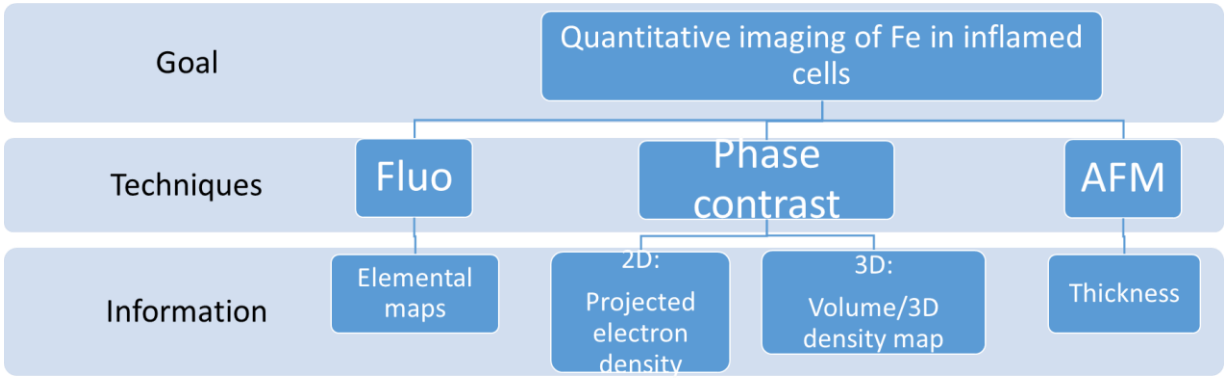
Goal
Quantitative imaging of Fe in inflamed cells
Techniques
Fluo
Phase contrast
AFM
Information
Elemental maps
2D:
Projected electron density
3D:
Volume/3D density map
Thickness

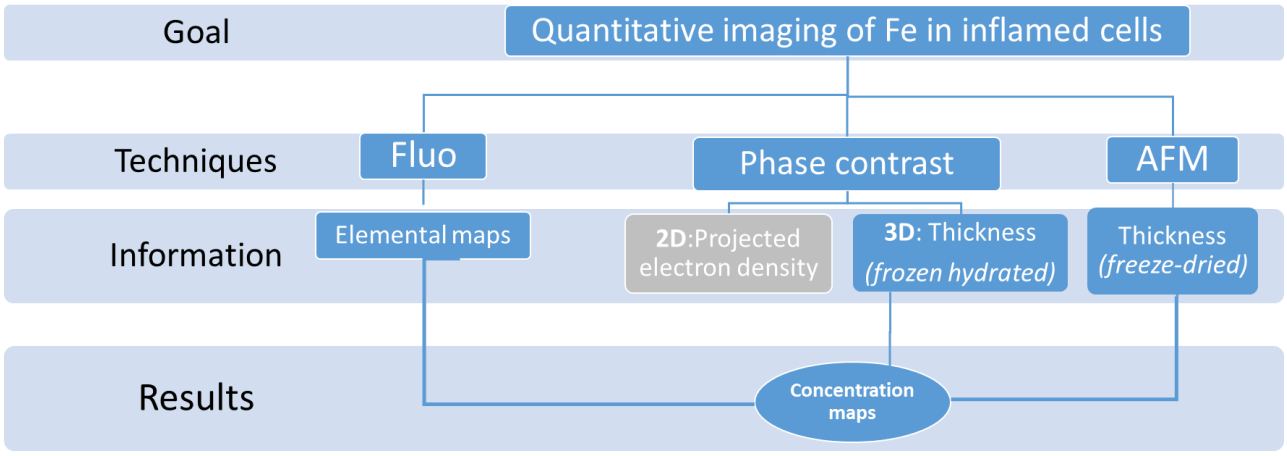
Goal
Quantitative imaging of Fe in inflamed cells
Techniques
Fluo
Phase contrast
AFM
Information
Elemental maps
2D:Projected electron density
3D: Thickness (frozen hydrated)
Thickness (freeze-dried)
Results
Concentration maps

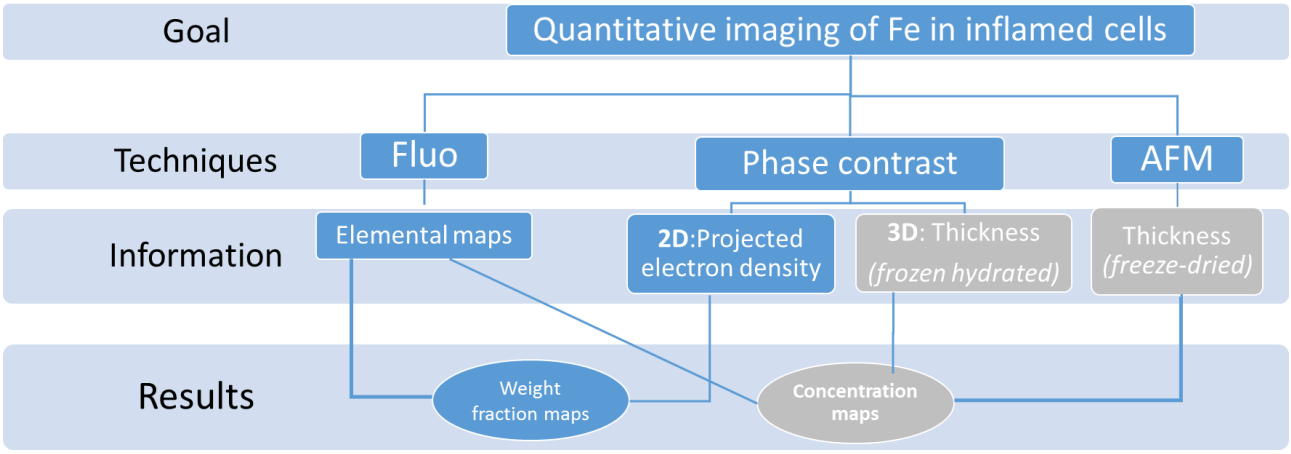
Goal
Quantitative imaging of Fe in inflamed cells
Techniques
Fluo
Phase contrast
AFM
Information
Elemental maps
2D:Projected electron density
3D: Thickness (frozen hydrated)
Thickness (freeze-dried)
Results
Weight fraction maps
Concentration maps

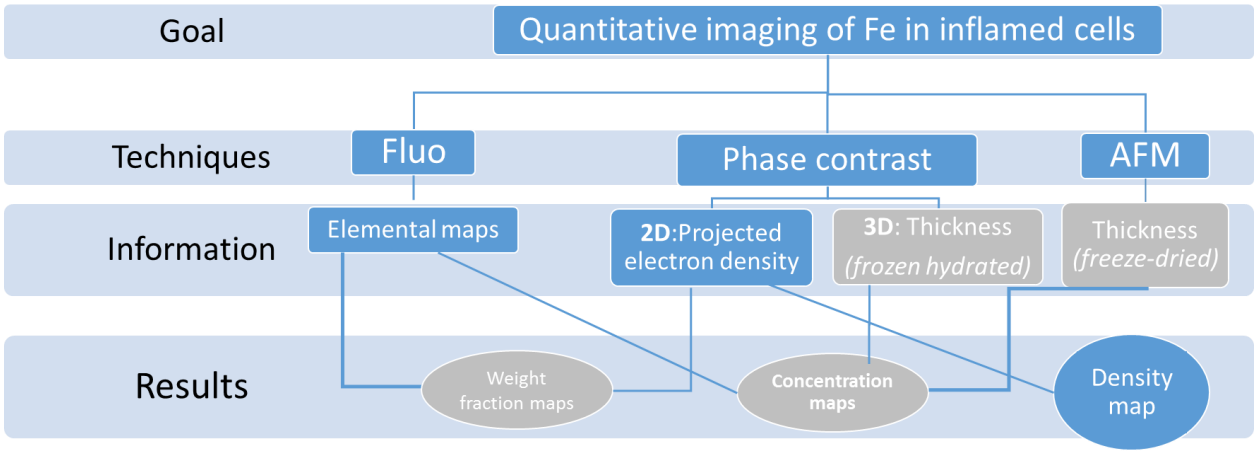
Goal
Quantitative imaging of Fe in inflamed cells
Techniques
Fluo
Phase contrast
AFM
Information
Elemental maps
2D:Projected electron density
3D: Thickness (frozen hydrated)
Thickness (freeze-dried)
Results
Weight fraction maps
Concentration maps
Density map

I have presented in the Annex2 the Iron Mass Fraction and Fluorescence count results obtained for each tipology of the cells differentiating between the nucleus and the cytoplasm for all the experiments carried out: ls2433-ls2551, which in principle have the same conditions.

The distinction between nucleus and cytoplasm in iron mass fraction and fluorescence map was made possible by the analysis of phosphorus and potassium maps where the nucleus is clearly distinguishable (see chapter VIII).

The data show a large variability between cells which are nominally in the same conditions, even larger than the variability between cells subjected to different treatments. Further analysis are needed to interpret these data.

SAMPLE			CTRL	CTRL	CTRL	LPS	LPS	LPS	LPLF	LPLF	LPLF	CTRL	CTRL	LF	LF	CTRL	LPS	LPLF	LF
			C6a	C6b	C14	C3	C4	C12	C1	C2	C4	C1	C2	C1	C3				
			LS2433									LS2551				LS2433-LS2551	LS2433	LS2433	LS2551
Weight Fraction Mean	Fe	NUCLEO	2.75E-04	2.83E-04	8.25E-05	2.00E-03	1.42E-04	1.61E-04	2.52E-04	5.36E-04	3.91E-04	2.69E-04	2.80E-04	2.90E-04	2.87E-04	2.38E-04	7.68E-04	3.93E-04	2.89E-04
		CITOPLASMA	1.58E-04	1.34E-04	2.44E-05	4.00E-05	7.17E-05	8.30E-05	1.48E-04	2.62E-04	2.86E-04	1.23E-04	1.25E-04	7.35E-05	9.47E-05	1.13E-04	6.49E-05	2.32E-04	8.41E-05

Table A2 .1: *Iron Mass Fraction: Average value given for each tipology of the cells differentiating between the nucleus and the cytoplasm for all experiment carried out.*

SAMPLE		LS2433					LS2551		LS2433-LS2551
		CTRL	CTRL	CTRL	LPS94	LPLF106	CTRL	LF	CTRL
Weight Fraction	Fe	9.6441E-05	5.657E-06	2.19203E-05	1.5724E-05	1.3E-04	9.2E-06	7.1E-07	8.6E-05
Count	Fe	163.716	18.385	16.263	34.064	224.960	12.728	33.941	143.179

Table A2 .2: *Iron Mass Fraction and Fluorescence count: Average value given for each tipology of the cells for all experiment carried out.*

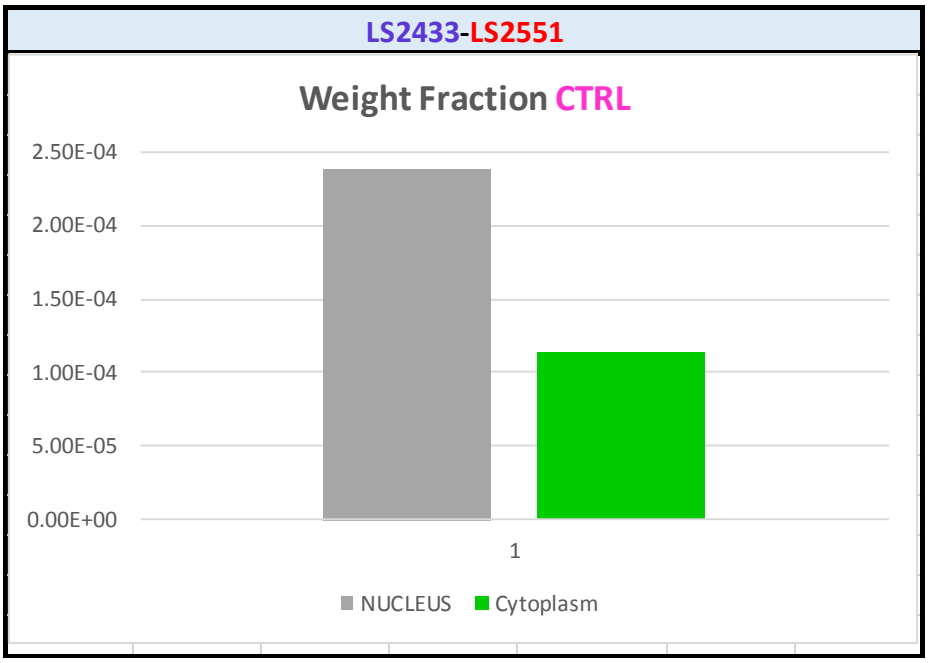

Figure A2 .1: *Iron, Phosphorus and Potassium Mass Fraction: Average value given for control cells differentiating between the nucleus and the cytoplasm for the experiment ls2433 and ls2551.*

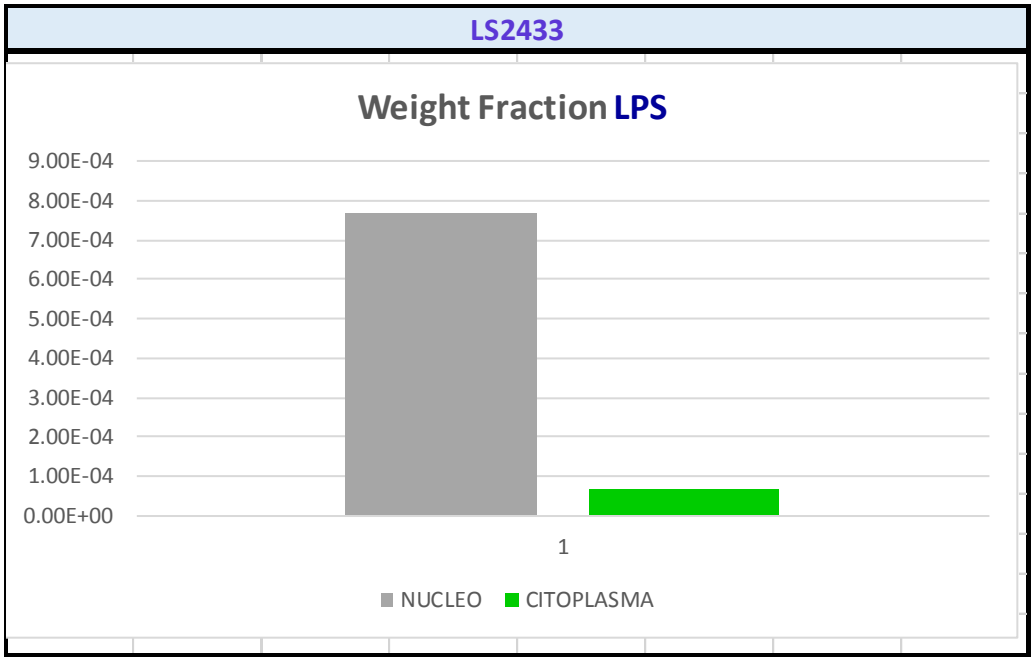

Figure A2 .2: *Iron, Phosphorus and Potassium Mass Fraction: Average value given for cells treated with LPS differentiating between the nucleus and the cytoplasm for the experiment ls2433.*

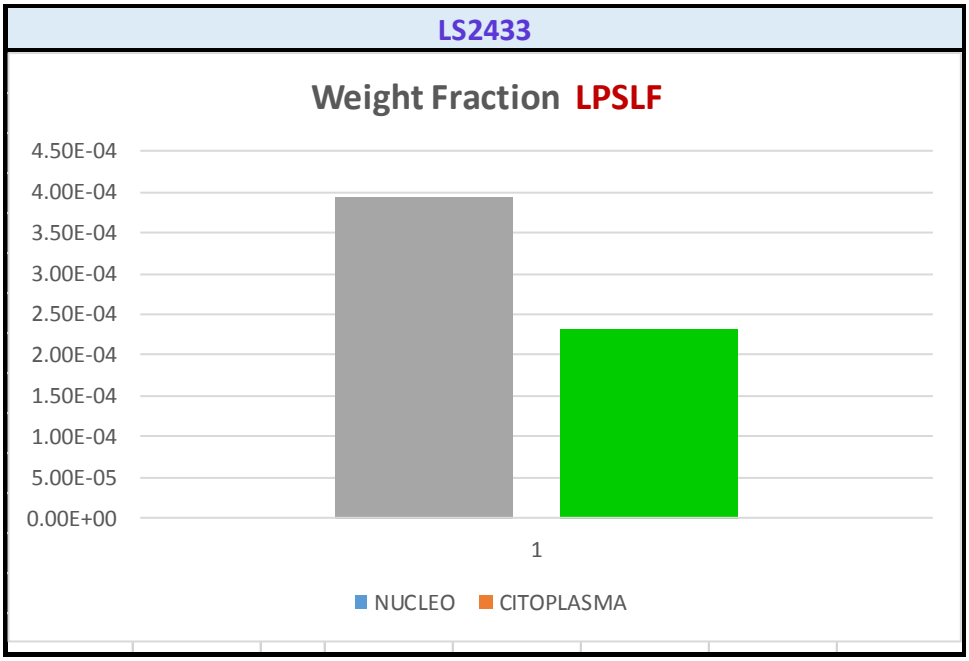

Figure A2 .3: *Iron, Phosphorus and Potassium Mass Fraction: Average and Standard Deviation value given for cells treated with LPS and LF differentiating between the nucleus and the cytoplasm for the experiment ls2433.*

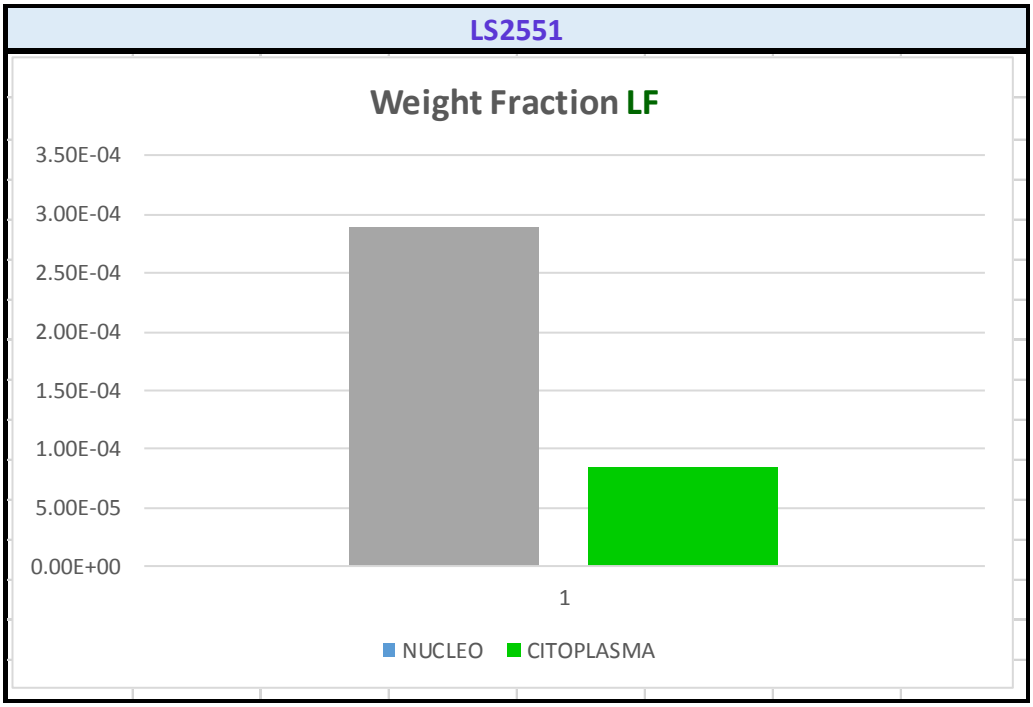

Figure A2 .4: *Iron, Phosphorus and Potassium Mass Fraction: Average value given for cells treated with LF differentiating between the nucleus and the cytoplasm for the experiment ls2551.*

Fe K P

Bibliography

[1] Kim, K.J. proc. VII National Conference on Synchrotron Radiation. 1986.

[2] J. M. Cowley, Diffraction Physics, North Holland, Amsterdam, 1975.

[3] M. Born and E. *Wolf*, Principles of Optics, 6th ed. Pergamon, Oxford, 1980.

[4] W.L. Bragg, Proc. Cambridge Phil. Soc. **17**, 43 (1913).

[5] G. Schmahl, and P. Cheng, X-Ray Microscopy, in *Handbook on Synchrotron Radiation,* Vol 4, edited by S. Ebashi, M. Koch, and E. Rubenstein, Elsevier Science Publishers B. V., 1991.

[6] O.E. Meyers, Amer. J.Phys 19, 359 (1951).

[7] Malucelli E., Iotti S., Gianoncelli A., Fratini M., Merolle L., Notargiacomo A., Marraccini C., Sargenti A., Cappadone C., Farruggia G., Bukreeva I., Lombardo M., Trombini C., Maier J.A., Lagomarsino S. Quantitative Chemical Imaging of the Intracellular Spatial Distribution of Fundamental Elements and Light Metals in Single Cells.2014, American Chemical Society.

[8] Bohic S., Simionovici A., Snigirev A., Ortega R., Devès G., et.al. 2001. Appl. Phys. Lett. 78 (22), 3544 - 3546.

[9] Ortega R., Bresson C., Fraysse A., Sandre C., Devès G., et.al. 2009. Toxicology Lett. 188, 26-32.

[10] Gori, Elementi di ottica, 1995.

[11] Sole V., Papillon E., Cotte M., Walter P., Susini J., 2007. Spectrochim. Acta Part B At. Spectrosc. 62, 63-68.

[12] De Jonge M., Hornberger B., Holzner C., Paterson D., Jacobsen C., et.al., 2008. Phys. Rev. Lett. 100, 163902.

[13] Di Fabrizio E., Cojoc D., Cabrini S., Kaulich B., Susini J., et.al., 2003. Opt. Express 11, 2278-2288.

[14] Tsuchiya S., Yamabe M., Yamaguchi Y., Kobayashi Y., Konno T., Tada K. Establishment and characterization of a human acute monocytic leukemia cell line (THP-1). 1980. International journal of cancer.

[15] Scorneaux B., Ouadrhiri .Y, Anzalone G., Tulkens PM. Effect of recombinant human gamma interferon on intracellular activities of antibiotics against Listeria monocytogenes in the human macrophage cell line THP-1. *Antimicrob Agents Chemother* (1996) **40**:1225-30.

[16] Cutone A., Frioni A., Berlutti F., Valenti P., Musci G. and Bonaccorsi di Patti MC. 2014 Lactoferrin prevents LPS-induced decrease of the iron exporter ferroportin in human monocytes/macrophages Biometals **27**: 807-13.

[17] Cutone A., Rosa L., Lepanto MS., Scotti MJ., Berlutti F., Bonaccorsi Di Patti MC., Musci G. and Valenti P. Lactoferrin Efficiently Counteracts the Inflammation-Induced Changes of the Iron Homeostasis System in Macrophages. 2017 (accepted). Frontiers in Immunology.

[18] Baker EN., and Baker HM. Molecular structure, binding properties and dynamics of lactoferrin. *Cell Mol Life Sci* (2005) **62**: 2531-9.

[19] Valenti P., and Antonini G. Lactoferrin: an important host defence against microbial and viral attack. *Cell Mol Life Sci* (2005) **62**:2576-87. doi: 10.1007/s00018-005-5372-0.

[20] Cutone A., Frioni A., Berlutti F., Valenti P., Musci G. and Bonaccorsi di Patti MC. 2014 Lactoferrin prevents LPS-induced decrease of the iron exporter ferroportin in human monocytes/macrophages Biometals **27**: 807-13.

[21] Malm J., Giannaras D., Riehle MO., Gadegaard N., Sjovall P. (2009) Fixation and drying protocols for the preparation of cell samples for time-of-flight secondary Ion mass spectrometry analysis. Anal Chem **81**:7197–7205.

[22] Passarelli MK., Winograd N. (2011) Characterizing in situ glycerophospholipids with SIMS and MALDI methodologies. Surf Interface Anal **43**: 269–271.

[23] Cloetens P, Ludwig W., Baruchel J., Dyck J V., Landuyt J V. and al. 1999 Holotomography: quantitative phase tomography with micrometer resolution using hard synchrotron radiation X-rays Appl. Phys. Lett. **75:** 2912–14.

[24] Langer M., Cloetens P., Guigay JP. and Peyrin F. 2008 Quantitative comparison of direct phase retrieval algorithms in in-line phase tomography Med. Phys. **35** (10) 4556–66.

[25] Lagomarsino S., Iotti S., Farruggia G., Cedola A., Trapani V., Fratini M. and al. 2011 Intracellular concentration map of magnesium in whole cells by combined use of X-ray fluorescence microscopy and atomic force microscopy Spectrochim Acta Part B At Spectrosc. **66** (11–12) 834–40.

[26] Gramaccioni C., Procopio A., Farruggia G., Malucelli E., Iotti S., Notargiacomo A., Fratini M., Yang Y., Pacureanu A., Cloetens P., Bohic S., Massimi L., Cutone A., Valenti P., Rosa L., Berlutti F. and Lagomarsino S. “Combined use of X-ray fluorescence microscopy, phase contrast imaging for high resolution quantitative iron mapping in inflamed cells.” Journal of Physics: Conference Series, Volume **849**, conference 1.

[27] Paesano R., Natalizi T., Berlutti F. and Valenti P. 2012 Body iron delocalization: the serious drawback in iron disorders in both developing and developed countries Pathog. Glob. Health **106** 200-16.

[28] Cairo G., Recalcati S., Mantovani A. and Locati M. 2011 Iron trafficking and metabolism in macrophages: contribution to the polarized phenotype Trends Immunol **32**: 241–47.

The research was granted by Sapienza University of Rome to PV and FB and by a **STSM** of the **Cost 1207**.

List of Publication

Gramaccioni C., Procopio A., Farruggia G., Malucelli E., Iotti S., Notargiacomo A., Fratini M., Yang Y., Pacureanu A., Cloetens P., Bohic S., Massimi L., Cutone A., Valenti P., Rosa L., Berlutti F. and Lagomarsino S. "Combined use of X-ray fluorescence microscopy, phase contrast imaging for high resolution quantitative iron mapping in inflamed cells." Journal of Physics: Conference Series, Volume 849, conference 1.

Gramaccioni C., Yang Y., Pacureanu A., Cloetens P., Bohic S., Malucelli E., Iotti S., Procopio A., Bukreeva I., Notargiacomo A., Fratini M., Valenti P., Rosa L., Berlutti F. and Lagomarsino S. **"Nanoscale quantitative determination of intracellular element concentration combining X-ray fluorescence microscopy with holotomography."**

Gramaccioni C., Malucelli E., Procopio A., Cloetens P., Bohic S., Iotti S., Valenti P., Rosa L., Berlutti F., Lagomarsino S. and Da Silva J.. "Comparison between X-ray near-field ptychography and phase contrast imaging". **In preparation for Small.**

Gramaccioni C., Rosa L., Malucelli E., Procopio A., Cloetens P., Notargiacomo A., Fratini M., Bohic S., Iotti S., Lagomarsino Berlutti F. and Valenti P.. "Localization of Fe linked to the pathogenicity of frozen hydrated cells". **To be published for Biometals special issue.**

Procopio A., Pacureanu A., Sargenti A.,.Gramaccioni C., Cappadone C., Farruggia G., Iotti S., Maier J., Cloetens P., Malucelli E. Ultrastructural study of biomineralization process in human bone marrow mesenchymal stem cells during the osteoblastic differentiation. **In preparation for Science.**